THE PREPARATION OF HIGH PERFORMANCE PEROVSKITE SOLAR CELLS

CAO JIUPENG

PhD
The Hong Kong Polytechnic University
2021

The Hong Kong Polytechnic University
Department of Applied Physics

The preparation of high performance perovskite solar cells

CAO Jiupeng

A thesis submitted in partial fulfillment of the requirements for the degree of Doctor of Philosophy

August 2020

CERTIFICATE OF ORIGINALITY

I hereby declare that this thesis is my own work and that, to the best of my knowledge and belief, it reproduces no material previously published or written, nor material that has been accepted for the award of any other degree or diploma, except where due acknowledgement has been made in the text.

_____(Signed)

Cao Jiupeng_____(Name of student)

Abstract

Compared to traditional silicon solar cells, the third generation solar cells have many advantages, like low cost, simple fabrication and mechanical flexibility. Organic inorganic perovskites have been one of the most promising light absorbing materials for the third generation solar cells because of their excellent optoelectronic properties, like broad spectral absorption, high carrier mobility and long carrier diffusion length. In a few years, the power conversion efficiency (PCE) of perovskite solar cells (PSC) has increased from 3.8% to more than 25%, which is close to the efficiency of high performance silicon solar cells.

In this thesis, 2-dimentional (2D) WS_2 flakes with defect-free surfaces are introduced as a template for van der Waals epitaxial growth of mixed perovskite films by solution process. The mixed perovskite films demonstrate a preferable growth along (001) direction on WS_2 surfaces. In addition, the WS_2/perovskite heterojunction forms a cascade energy alignment for efficient charge extraction and reduced interfacial recombination. This work demonstrates that high-mobility 2D materials can find important applications in PSCs as well as other perovskite-based optoelectronic devices.

Then, ammonium hypophosphite is introduced into the $FASnI_3$ perovskite precursor to suppress the oxidation of Sn^{2+} and assist the growth of perovskite grains, leading to improved perovskite film quality and reduced defect density, and consequently, the device efficiency and open circuit voltage are substantially improved. More importantly, the solar cells exhibit pronounced enhancement of long-term stability. This work provides a facile approach for improving the performance of tin-based perovskite solar cells by introducing ammonium hypophosphite as an antioxidant agent in the precursor solution.

Besides, Mixed Sn-Pb perovskites with bandgaps of 1.2－1.3 eV are ideal candidates for single-junction solar cells according to the Shockley-Queisser limit. However, the efficiency and stability of mixed Sn-Pb perovskite solar cells still lag behind that of its pure Pb counterpart due to the easy oxidation of Sn^{2+}. Here, multiple

functional additive 4-hydrazinobenzoic acid (HBA) is introduced to suppress the oxidation of Sn^{2+}. Meantime, incorporation of HBA can regulate the crystallization process of perovskite, leading to improved crystallinity and enlarged grain size. In addition, the HBA-SnF_2 complex presented at grain boundaries could passivate trap states and reduce nonradiative recombination. Consequently, the performance of perovskite solar cells increased from 17.16% to 20.14% along with enhanced stability.

List of publications

1. **Cao J**, Tai Q, You P, Tang G, Wang T, Wang N, Yan F. Enhanced performance of tin-based perovskite solar cells induced by an ammonium hypophosphite additive. *Journal of Materials Chemistry A*. 2019;7(46):26580-5.

2. Tai Q*, **Cao J***, Wang T, Yan F. Recent advances toward efficient and stable tin-based perovskite solar cells. *EcoMat*. 2019 Dec;1(1):e12004. (* equal contribution)

3. **Cao J**, Tang G, You P, Wang T, Zheng F, Zhao J, Yan F, Enhanced Performance of Planar Perovskite Solar Cells Induced by Van Der Waals Epitaxial Growth of Mixed Perovskite Films on WS_2 Flakes. *Advanced Functional Materials*. 2020, 2002358.

4. Loi HL, **Cao J**, Guo X, Liu CK, Wang N, Song J, Tang G, Zhu Y, Yan F. Gradient 2D/3D Perovskite Films Prepared by Hot-Casting for Sensitive Photodetectors. *Advanced Science*. 2020 May 29:2000776.

5. You P, Li G, Tang G, **Cao J**, Yan F. Ultrafast laser-annealing of perovskite films for efficient perovskite solar cells. *Energy & Environmental Science*. 2020;13(4):1187-96.

Acknowledgements

There are so many people that I would like to express my profound gratitude for their support and company during my study in The Hong Kong Polytechnic University.

First of all, I would like to thank my supervisor, Prof. Feng Yan. He gives me a lot valuable suggestions on both my study and life. It is his guidance, encouragement and supervision that inspire me to finish my PhD study on time. His high degree of enthusiasm for scientific research and unselfish assistance help me overcome the obstacles during my doctorial study. I will always be grateful for the advice and knowledge he shared during my study here.

Further, I would like to express my sincere thanks to my group member, Dr. Peng You, Dr. Naixiang Wang, Dr. Anneng Yang, Dr. JianZhong Zheng, Dr. Haifeng Ling, Dr. Shenghua Liu, Dr. Xuming Zou, Dr. Runsheng Wu, Dr. Ji Yu, Dr. Ying Fu, Dr. Wei Tang, Dr. Guanqi Tang, Mr. Jiajun Song, Mr. Xueliang Lei, Mr. Junqi Liao, Mr. Fangjie Li, Ms. Tianyue Wang, Ms. Hong Liu, Ms. Guannan Yin, Ms. Sihua Li. Thanks so much for their company and support during my study in PolyU.

Besides, my sincere gratitude is given to the technicians in PolyU who support my experiments here. I appreciate Dr. Vincent, Dr. Hardy, Mr. Chan Lam and Ms. Henrietta for their guidance in the experimental operation.

Finally, I would like to express my deep love to my family. It is their unconditional support and encouragement that motivate me to climb the peak of scientific research.

Table of Contents

List of Figures

Chapter 1 Introduction

1.1 Background

After the third industrial revolution, the repaid development of society has resulted in vast demand for energy. Up to now, the energy supply mainly comes from fossil fuel, which causes serious environmental problems, like global warming. Worse still, the severe environmental problem may lead to human health issues, like respiratory illness or even serious infectious diseases. With the increasing need of clean and renewable energy, photovoltaic technology, which converts solar energy into electricity directly, is attracting more and more attention.

Nowadays, silicon-based photovoltaic technology is dominating the world market because of its high efficiency and long term operation stability. However, the silicon-based solar cells are high cost and have complicated technological process, which make them less competitive against other energy sources. As one of the third generation photovoltaic technologies, organic-inorganic halide perovskites solar cells (PSCs) have been considered to be one of the most promising technology to replace silicon due to their rapid development of power conversion efficiency (PCE) from 3.8% to 25% in the past few years[1, 2]. Compared with silicon solar cells, perovskite solar cells have many advantages, like simple solution process, low cost and flexibility. However, there are still some issues about perovskite solar cells needed to be resolved before their commercial readiness.

1.2 Objectives of Research

The performance of perovskite solar cells is closely related to the quality of perovskite films, especially the crystal orientation, which cannot be easily controlled by solution processes. We introduced 2-dimentional (2D) WS_2 flakes with defect-free surfaces as a template for van der Waals epitaxial growth of mixed perovskite films by solution process. The mixed perovskite films demonstrate a preferable growth along (001) direction on WS_2 surfaces. In addition, the WS_2/perovskite heterojunction forms a cascade energy alignment for efficient charge extraction and reduced interfacial

recombination. The inverted PSCs with WS_2 interlayers show much higher efficiency and enhanced stability compared with the control one.

Among the high performance perovskite devices, Pb^{2+} is still necessary to achieve excellent photovoltaic properties. However, the degradation products of lead-based perovskites are toxic and will cause serious environmental problems, which hinders the wide application of this technology. Tin has been considered as less toxic alternative to lead. However, tin-based perovskites face serious oxidation issue. Ammonium hypophosphite was introduced into tin-based perovskite precursor to suppress the oxidation of Sn^{2+} and assist the growth of perovskite grains, leading to improved perovskite film quality. Consequently, the device efficiency and long term stability are substantially improved.

Mixed Sn-Pb perovskites with bandgaps of 1.2—1.3 eV are ideal candidates for single-junction solar cells according to the Shockley-Queisser limit. However, the efficiency and stability of mixed Sn-Pb perovskite solar cells still lag behind that of its pure Pb counterpart due to the easy oxidation of Sn^{2+}. Multiple functional additive HBA was introduced to inhibit the oxidation of Sn^{2+}. Meantime, the introduction of HBA can regulate the crystallization process of perovskite, leading to enhanced crystallinity. Hence, the performance and long term stability of perovskite solar cells are greatly enhanced.

1.3 Outline of Thesis

Chapter 1: In this chapter, the backgrounds of perovskite photovoltaic devices are introduced.

Chapter 2: The development of perovskite for photovoltaic applications is briefly reviewed. Then, the application of transition metal dichalcogenides (TMDs) to enhance the performance of perovskite solar cells is discussed. For tin-based perovskite solar cells, the introduction of reducing agents to suppress the oxidation of Sn^{2+} and usage of additives to control the perovskite film morphology are presented. Subsequently, the efforts to enhance the performance of mixed Sn-Pb perovskite solar cells are briefly discussed.

Chapter 3: 2-dimentional (2D) WS_2 flakes with defect-free surfaces are introduced as a template for van der Waals epitaxial growth of mixed perovskite films by solution process. The mixed perovskite films demonstrate a preferable growth along (001) direction on WS_2 surfaces. In addition, the WS_2/perovskite heterojunction forms a cascade energy alignment for efficient charge extraction and reduced interfacial recombination.

Chapter 4: Ammonium hypophosphite is introduced into the $FASnI_3$ perovskite precursor to suppress the oxidation of Sn^{2+} and assist the growth of perovskite grains, leading to improved perovskite film quality and reduced defect density, and consequently, the device efficiency is substantially improved. More importantly, the solar cells exhibit pronounced enhancement of long-term stability.

Chapter 5: Multiple functional additive 4-hydrazinobenzoic acid (HBA) was introduced in Mixed Sn-Pb perovskite to suppress the oxidation of Sn^{2+}. Meantime, incorporation of HBA can regulate the crystallization process of perovskite, leading to improved crystallinity and enlarged grain size. In addition, the HBA-SnF_2 complex presented at grain boundaries could passivate trap states and reduce nonradiative recombination.

Chapter 6: Conclusions and future outlook.

Chapter 2 Overview of Organic-inorganic Hybrid Perovskite Solar Cells

2.1 Introduction

Generally, hybrid halide perovskites have a formula of ABX_3, where A is organic ($CH_3NH_3^+$, MA or $HC(NH_2)_2^+$, FA) or alkali metal (Cs^+) cation, B is divalent metal (Pb, Sn or Ge) and X is halide anion[3]. Ideally, the B site cations are octahedrally coordinated by six X anions while the A cations reside at the eight corners of the cubic unit as shown in **Figure 2.1**a[4]. To stabilize the 3D perovskite structure, the empirical Goldschmidt's tolerance factor (t) must be satisfied, i.e., $t=(R_A+R_X)/[2^{1/2}(R_B+R_X)]$, where R_A, R_B and R_X are the ionic radii of A, B and X ions, respectively[5]. The tolerance factor can range from 0.813 to 1.107, otherwise the cubic crystal structure will be destroyed[6]. The tolerance factor of a series of common halide perovskites is shown in Figure 2.1b.

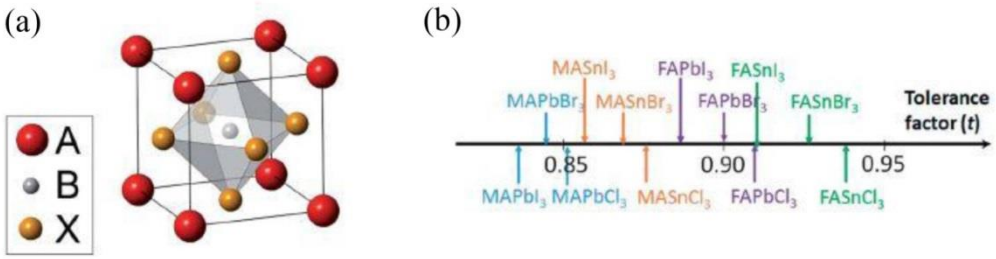

Figure 2.1 Cubic structure of 3D perovskite[7]. (b) Tolerance factor of a series of common perovskites[8].

Excellent photoelectric properties come from this 3D perovskite structure, like long carrier recombination lifetime, small effective mass for electron and hole, wide absorption of light and high charge mobility[9-13]. Specifically, adopting alkylammonium cations in the A position will result in a layered perovskite structure (Ruddlesden-Popper [RP] phase)[14]. The RP phase layered perovskite has a general formula of $L_2A_{n-1}B_nX_{3n+1}$, where L is a large cation (such as butyl ammonium

$C_4H_9NH^{3+}$ [BA^+]) and n is an integer[15]. Another low dimensional perovskites structure is Dion-Jacobson (DJ) type, which features divalent (2+) interlayer spacers[16, 17]. Analysis of this tolerance factor is helpful to understanding the structural transition in compositional engineering of perovskite materials.

2.2 Device Design of Perovskite Solar Cells

2.2.1 Device Structure

As shown in **Figure 2.2**, PSCs are usually prepared in two kinds of structures, normal structure and inverted structure, which primarily consist of transparent conductive oxide (TCO), electron transporting layer (ETM) and hole transporting layer (HTM)[18, 19]. The normal structure can be further divided into mesoporous and planar structures while the inverted structure is usually planar[20]. Generally, when perovskite is illuminated by sunlight, electron is excited from valence band (VB) to conduction band (VB) and hole is left in VB. Then, the generated electrons and holes are transported to each interface and injected to ETM and HTM, respectively. Here, the CB and VB of perovskite should form good energy level alignment with charge transporting layer and high carrier mobility of charge transporting layer is required to ensure efficient charge transport. Finally, electrons and holes are collected by working and counter electrodes and transported to external circuit.

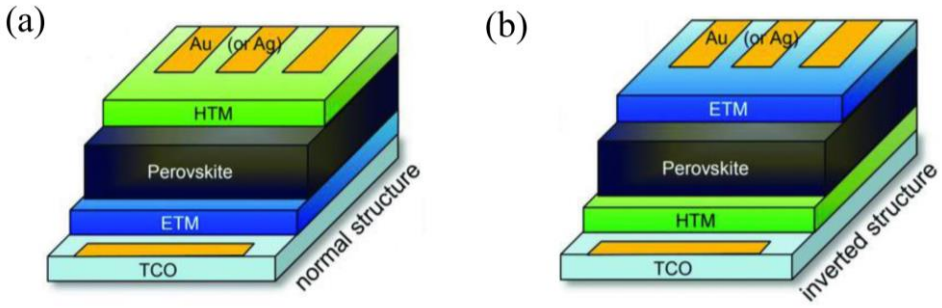

Figure 2.2 Schematically illustrated device structures of perovskite solar cells: (a) normal structure and (b) inverted structure[18].

2.2.2 Encapsulation Technology

Encapsulation of photovoltaic devices can prevent the permeation of moist and oxygen, which is one of the best ways to enhance the operation stability for

commercialization. The encapsulation materials should have good processability, high light transmission and good resistance to ultraviolet (UV) degradation and thermal oxidation[21]. Atomic layer deposition (ALD) has been used to encapsulate perovskite layers to enhance the humidity stability of PSCs[22]. However, the ALD process is expensive and increase the complexity of fabrication. Other common encapsulation methods include roll lamination (the devises are encapsulated by two adhesive sheets)[23], heat sealing (thermal energy is introduced to soften the sealants for encapsulation)[24] and glass substrate sealed by UV-curable epoxy[25]. Due to the easy oxidation of Sn^{2+} to Sn^{4+} (we will present detailed discussion later), timely encapsulation of tin-based PSCs is highly needed to avoid oxygen, thereby improving the long term device stability.

2.3 Transitional Metal Dichalcogenides (TMDs)

Transition metal dichalcogenides (TMDs), with the formula MX_2, where M is a transition metal atom (Mo or W) and X is a chalcogen atom (S or Se), have outstanding chemical, physical and electronic properties. Generally, the transition metal layer is sandwiched between two chalcogen layers, and the electronic and optical properties of TMDs significantly depend on the number of layers. For example, the in-direct bandgap of the bulk TMDs can change into direct bandgap when exfoliated to monolayer[26]. Moreover, TMDs have excellent charge carrier mobility, making them promising materials as charge transporting materials for perovskite solar cells.

2.3.1 TMDs for Hole Transporting

MoS_2 has high carrier mobility and an appropriate energy level and Capasso et al. used solution-processed MoS_2 flakes as hole transporting layer (HTL) for normal structure mesoporous PSCs[27]. MoS_2 flakes were exfoliated in 2-propanol (IPA) and deposited on perovskite layer by spray coating. The solar cells based on MoS_2 showed higher performance as well as much enhanced stability compared with that using doped spiro-OMeTAD. Kim and co-workers used chemical vapor deposition (CVD) method to prepare MoS_2 and WS_2 layers and used them as HTL for inverted planar PSCs[28]. Atomic force microscopy (AFM) data confirmed the roughness of these

TMDs layers was low enough to prepare the perovskite layer. The PCE of MoS_2 based devices was higher than that based on WS_2, which could be ascribed to the higher work function of MoS_2 and thus better energy level alignment with perovskite layer. To get large-area and uniform few layer MoS_2 sheets as HTL for planer inverted PSCs, Pal et al. used centrifugal-casting film formation method to form 2D MoS_2 nanosheets[29]. This centrifugal casting method was repeated several times to obtain a desired thickness of MoS_2 layers. Moreover, UV ozone (UVO) treatment of the MoS_2 layers was introduced to change the type-I band alignment to type-II band alignment at the MoS_2/perovskite heterojunction (**Figure 2.3**a). Photoluminescence (PL) spectroscopy confirmed the efficient hole transfer from perovskite to MoS_2 layer after UVO treatment (Figure 2.3b). This work highlights the importance of band alignment between the charge transporting layer and perovskite. Huang and co-workers used lithium intercalation reaction method to prepare water-soluble MoS_2, WS_2 and introduced them as HTLs for planar inverted PSCs[30]. Generally, MoS_2 and WS_2 have two commonly observed polymorphs, the natural semiconducting 2H phase and metallic 1T phase. Postheating of these TMD layers could cause great change of ratio of 1T phase in these samples. The content of 1T phase in the TMDs greatly influenced the device performance, which was caused by the different conductivities of these two different phases. The 1T phase possesses much higher conductivity, which contributes to better charge carrier extraction ability and thus reduced interfacial recombination. Moreover, the devices based on MoS_2 and WS_2 showed much enhanced stability compared to that based on PEDOT:PSS (Figure 2.3c). The hygroscopic nature of PEDOT:PSS cased poor stability of PEDOT:PSS-based PSCs. To improve the operating lifetime of PSCs, Kymakis and co-workers introduced MoS_2 flakes as hole transport interlayer for inverted planar solar cells[31]. These MoS_2 flakes have suitable energy level to facilitate hole extraction and serve as efficient electron blocking layer (Figure 2.3d). The introduction of MoS_2 interlayer could enhance the carrier extraction rate at the HTL/perovskite interface, contributing to improved device performance. Moreover, stability test of the encapsulated devices under continuous light soaking in ambient condition showed these MoS_2 interlayer could enhance the device stability. The MoS_2 modified device remained 80% of the original PCE after 568 h, while the control device reached 80% of the initial performance after only

about 170 h (Figure 2.3e). The much enhanced device stability could be ascribed to the blocking role of MoS_2 flakes at the interface, which prevents the migration of ions and then inhibits the degradation of perovskite at the interface. To improve the solubility of MoS_2, Dai et al. used a metal-organic compound (phenyl acetylene silver, PAS) to chemically modify MoS_2 through coordination bonds[32]. Fourier Transform Infrared Spectrometer (FTIR) spectra confirmed the coordination bond between MoS_2 and PAS (Figure 2.3f), and the MoS_2-PAS complex had good dispersibility in both dimethylformamide (DMF) and water. The PAS-modified MoS_2 was blended with PEDOT:PSS then used as HTL for planar inverted solar cells. The PCE of the devices increased from 14.69% to 16.47% because of enhanced hole extraction ability and transfer efficiency. Moreover, the device stability also improved due to the hydrophobicity of PAS modified MoS_2.

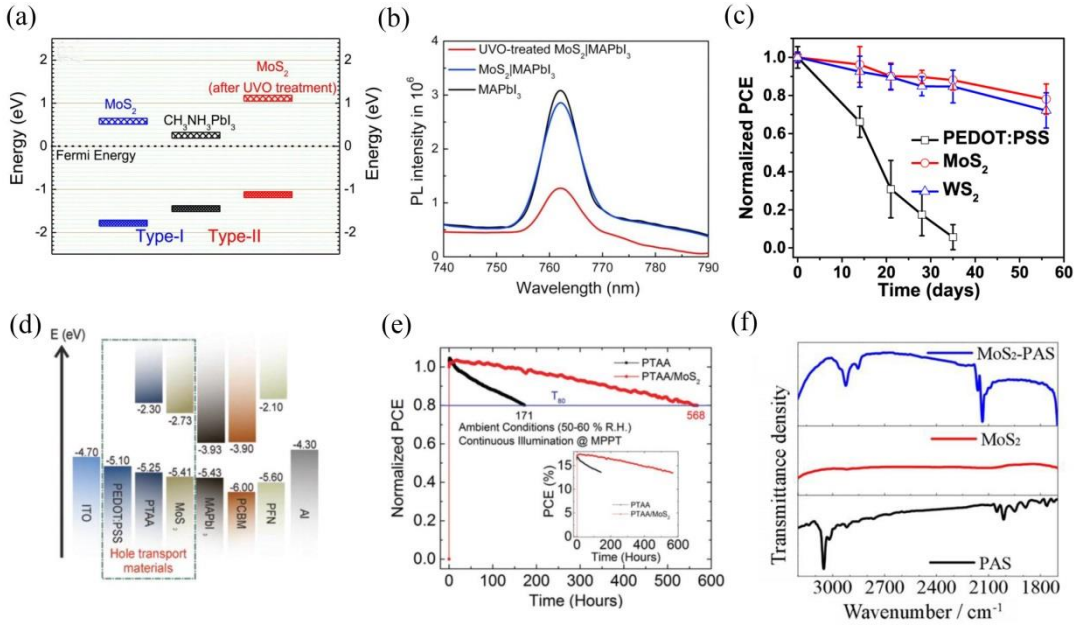

Figure 2.3 (a) Energy diagram of MoS_2/perovskite heterojunction. (b) PL spectra of perovskite layer on different substrates[29]. (c) Stability test of PSCs based on different HTLs[30]. (d) Energy diagram of the planar PSC. (e) Stability test of encapsulated PSCs under continuous illumination in ambient condition. Inset: actual MPP values of both devices[31]. (f) FTIR spectra of MoS_2, PAS and MoS_2-PAS[32].

To improve the stability of normal structure mesoporous PSCs, Bonaccorso et al. introduced liquid exfoliated few layer MoS_2 flakes as buffer layer between perovskite and Spiro-OMeTAD[33]. The few layer MoS_2 buffer layer had dual function, it could not only act as barrier to block metal electrode migration but also serve as additional

energy matching layer to facilitate hole collection. The solar cells with MoS_2 buffer layer demonstrated much enhanced stability, remaining 93% of its original PCE under illumination for 550 h, while the control device retained only about 66% of the initial PCE (**Figure 2.4**a). The enhanced device stability comes from the surface passivation of the MoS_2 buffer, which blocks the iodine migration of perovskite and the diffusion of Au metal electrode[34].

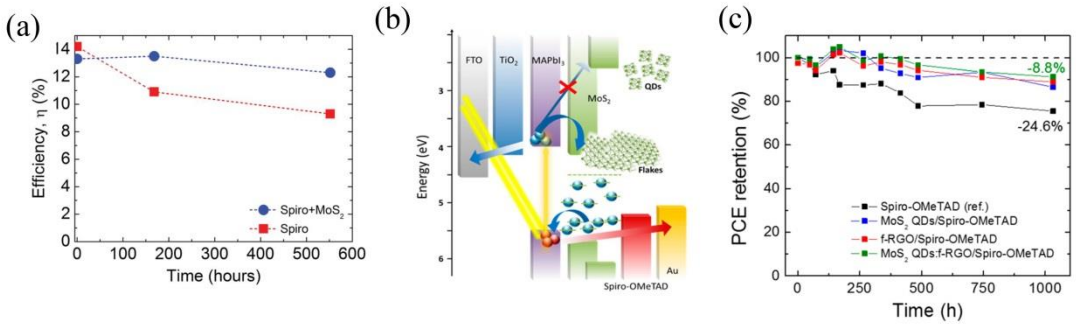

Figure 2.4 (a) Stability test of PSCs with and without MoS_2 buffer layer[33]. (b) Energy band positions of the materials in the $MAPbI_3$ based PSC. (c) Normalized PCE of the devices under 1 sun illumination[35].

Later, the same group used MoS_2 quantum dots (QD)/functionalized reduced graphene oxide (f-RGO) hybrids as buffer layer to improve the performance and stability of mesoscopic $MAPbI_3$-based PSCs[35]. Because of quantum confinement effects, the minimum energy of the conduction band (CB) of MoS_2 raised from -4.3 eV to -2.2 eV, which is above the lowest unoccupied molecular orbital (LUMO) of $MAPbI_3$ to block electron injection in HTL (Figure 2.4b). To achieve full coverage on the perovskite layer, the MoS_2 QDs were hybridized with f-RGO flakes. Thus, these MoS_2 QDs have dual function of hole-extraction and electron-blocking, which synergistically suppress the interfacial charge recombination. With these MoS_2 QDs/f-RGO interlayer, a maximum PCE over 20% was achieved with improved stability (Figure 2.4c). In other work, Choi and co-workers incorporated WSe_2 into PEDOT:PSS solution to serve as HTL in planar inverted PSCs[36]. The introduction of WSe_2 in PEDOT:PSS could improve the crystallinity of the perovskite films and facilitate effective carrier transport as well as reduce interfacial charge recombination. With the WSe_2-mediated PEDOT:PSS as HTL, the PCE increased from 13.8% to 16.3%.

2.3.2 TMDs for Electron Transporting

The electron transporting layer (ETL) is quite important for high performance PSCs, which should have suitable energy alignment with the perovskite layer as well as high carrier mobility. Zhao and co-workers used in situ hydrothermal method to fabricate 2D SnS_2 nanosheets as ETL for normal structure PSCs[37]. Benefiting from proper energy alignment of the device and high electron mobility of 2D SnS_2 nanosheets, a best PCE of 13.63% was achieved. In another work, Zhao et al. used self-assembly stacking deposition method to prepare few-layer SnS_2 as ETL for PSCs[38]. Compared with the common hydrothermal method, the self-assembly Langmuir-Blodgett (LB) deposition method facilitates the formation of compact and smooth SnS_2 surface, contributing to higher open-circuit voltage and fill factor of the device. Because of efficient electron extraction ability of SnS_2 layer, the champion device got an efficiency of 20.12% while the control device based on conventional SnO_2 ETL showed a PCE of 17.72% (**Figure 2.5**a). Moreover, X-ray photoelectron spectroscopy (XPS) spectroscopy showed the binding energies (BEs) of SnS_2/perovskite had an obvious shift compared with that of the bare perovskite and SnO_2/perovskite, indicating the Pb ··S interaction within the SnS_2/perovskite complex (Figure 2.5b). It is proposed that this Pb ··S interaction could facilitate the formation of microcosmic mosaic structure at the perovskite/SnS_2 interface, which contributes to efficient electron extraction and suppressed interfacial charge recombination. Moreover, this interaction helps to enhance the device stability. The solar cells based on SnS_2 retained 90% of its original efficiency after over 600 h, while the control device based on SnO_2 degraded to about 60% of its initial PCE under the same condition. Yin and co-workers used solution exfoliation method to prepare 2D TiS_2 nanosheets as ETL for planar PSCs[39]. Solar cells with TiS_2 as ETL achieved a PCE of 17.37%, which could be ascribed to the suitable energy level of the device and high electron mobility of TiS_2. Moreover, the low photocatalytic activity of TiS_2 could slow down the decomposition of perovskite under UV light illumination and thus improve the UV stability of the devices. The solar cells based on TiS_2 remained 90% of its original efficiency after illumination under UV light for 50 h, while the device with TiO_2 decayed by 44% under the same condition (Figure 2.5c). In addition, the

low-temperature processability of this TiS_2 ETL makes it promising for flexible PSC application. The flexible PSCs using TiS_2 ETL got a PCE of 12.75% with excellent mechanical stability (Figure 2.5d).

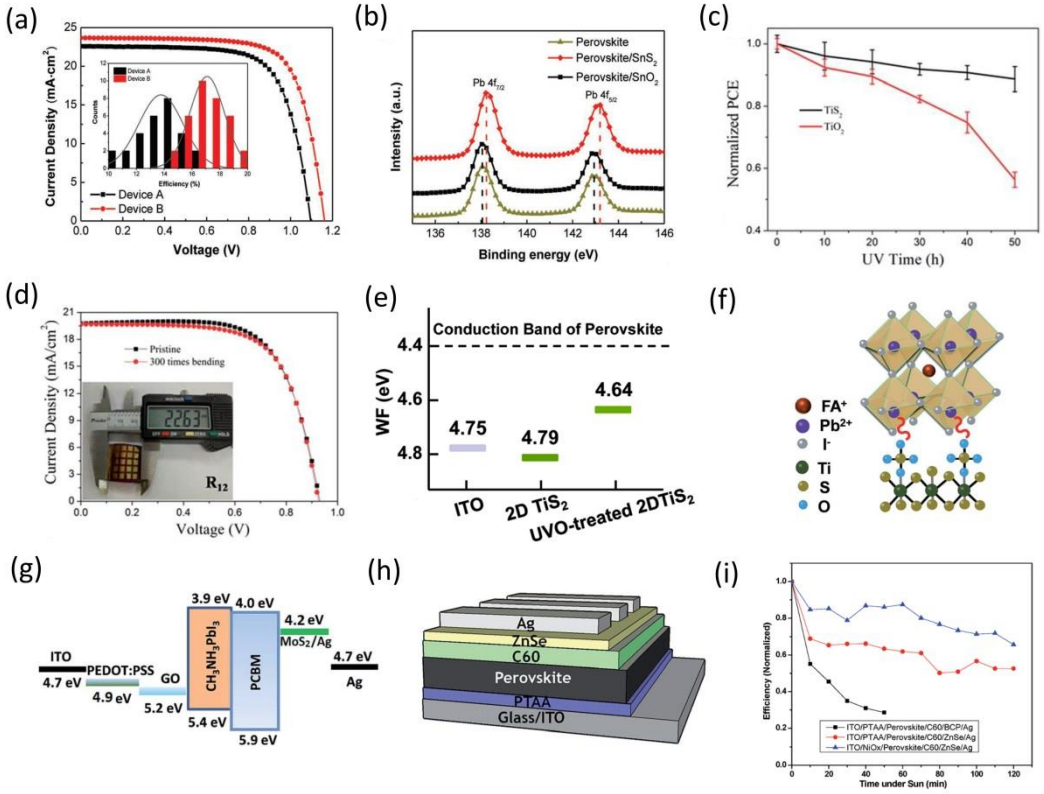

Figure 2.5 (a) J-V curves of the devices based on SnO_2 (devices A) and SnS_2 (devices B). (b) Pb 4f core level of XPS for perovskite, perovskite/SnS_2 and perovskite/SnO_2 films[38]. (c) UV light stability of the PSCs based on TiO_2 and TiS_2. (d) J-V curves of the flexible devices before and after 300 bending cycles with the curvature radius of 12 mm[39]. (e) Work function of ITO with the modification of TiS_2 and UVO-treated TiS_2 layer[40]. (f) A proposed bonding between 2D TiS_2 and perovskite[41]. (g) Schematic diagram of energy levels of the device[42]. (h) Device structure of the solar cells. (i) Stability test of the device with different transporting layers under continuous 1 sun illumination[43].

Similarly, Huang et al. used solution-processed 2D TiS_2 as ETL for planar normal structure PSCs[40]. UV-ozone (UVO) treatment of the 2D TiS_2 layers was introduced to tune the work function of this TiS_2 ETL to get smooth electron transfer from perovskite to ETL (Figure 2.5e). Based on the UVO-treated 2D TiS_2 ETL, a best PCE of 18.97% was achieved with good device stability. Recently, Huang and co-workers introduced 2D TiS_2 on top of SnO_2 and used this double layered structure as ETL for planar PSCs[41]. The highest PCE of 21.73% was achieved, which could be attributed

to the passivation of defects of SnO_2 by this TiS_2 layer and better energy level alignment between perovskite and the ETL. Moreover, it is proposed that a possible bonding between S and Pb could be favorable for the reduction of trap densities at the perovskite/ETL interface, which contributes to suppressed hysteresis (Figure 2.5f).

Wang and co-workers used graphene oxide (GO) and MoS_2 as interfacial layer for planar inverted PSCs to improve the device performance and enhance the device stability[42]. GO has a higher work function than that of PEDOT:PSS to form a better energy alignment with the highest occupied molecular orbital (HOMO) of $MAPbI_3$. Meantime, MoS_2 could reduce the work function of Ag cathode to match the LUMO of PCBM (Figure 2.5g). Benefiting from the ingenious energy match of the device and outstanding optoelectronic properties of the 2D materials, the PCE of the solar cells increased from 14.15% to 19.14%. Moreover, the MoS_2 layer could block the migration of I^- ions to suppress the reaction between $MAPbI_3$ and Ag. The suppressed interfacial reaction could improve the device stability. Bathocuproine (BCP) is commonly used as interfacial material for planar inverted PSCs to improve the device performance. However, BCP is not stable against UV light and cannot protect the perovskite layer. Imran and co-workers used 2D zinc selenide (ZnSe) as interfacial layer to improve the stability of PSCs[43]. ZnSe has a wide bandgap of 2.8-2.9 eV with high electron mobility, making it suitable material to replace BCP and the device structure is shown in Figure 2.5h. The PSCs with ZnSe showed comparable PCE with that based on BCP, but they demonstrated much improved light soaking stability. Furthermore, the devices with NiO_x and ZnSe showed even better stability, which comes from the stable nature of inorganic materials (Figure 2.5i). Later, the same group used 2D SnS as electron collection interlayer to replace BCP and achieved improved device stability[44]. Their work shows that interlayer engineering with suitable 2D materials could be a promising way to improve the performance and stability of PSCs.

2.4 Tin-based Perovskites

Among a large variety of perovskites and their low dimensional derivatives, Pb^{2+} is still necessary to achieve high device performance. However, the degradation

products of lead-based perovskites can be toxic for the environment, human and other species, which hinders the widespread application of this technology[45]. Therefore, less toxic lead-free perovskite light absorbers should be paid more attention. Tin has been considered as less toxic alternative to lead, which comes from the same group 14 of the periodic table as lead. Moreover, tin-based perovskites have optical bandgaps ranging from 1.2-1.4 eV[46], which is very close to the Shockley-Queisser limit (1.34 eV)[47].

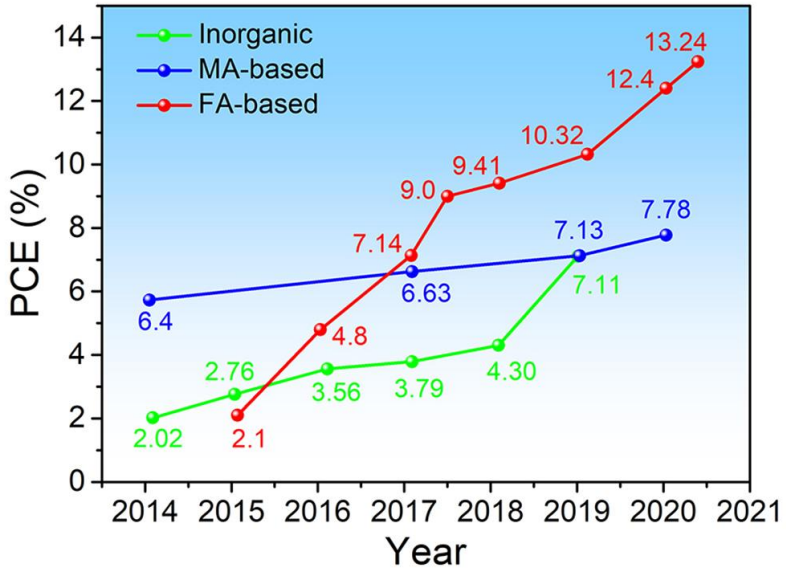

Figure 2.6 Efficiency progress of tin-based perovskite solar cells.

Tin-based halide perovskites were first introduced as conducting channels for thin-film filed effect transistors[48, 49]. In 2012, tin-based perovskite was used as light absorber for Schottky solar cells and a champion PCE of 0.9% was achieved[50]. In 2014, Noel et al. and Hao et al. reported tin-based PSCs almost at the same time, and promising PCE of around 6% was obtained[51, 52]. Researchers are encouraged by these initial results and tin-based PSCs have undergone rapid progress in the last few years. For example, low dimensional tin-based perovskites solar cells have reached PCE over 9%[53]. The efficiency progress of tin-based PSCs is shown in **Figure 2.6**. Currently, tin-based perovskite solar cells have achieved PCE of more than 13 %.

2.5 The Stability of Tin-based Perovskites

2.5.1 Properties of Tin-based Halide Perovskites

Locating in the same IVA group as Pb, Sn is one of the most promising metals to replace Pb. Tin-based perovskites $ASnX_3$ (A=MA, FA or Cs, X=halide) have attracted the attention of researchers from all over the world because of their excellent photoelectric properties.

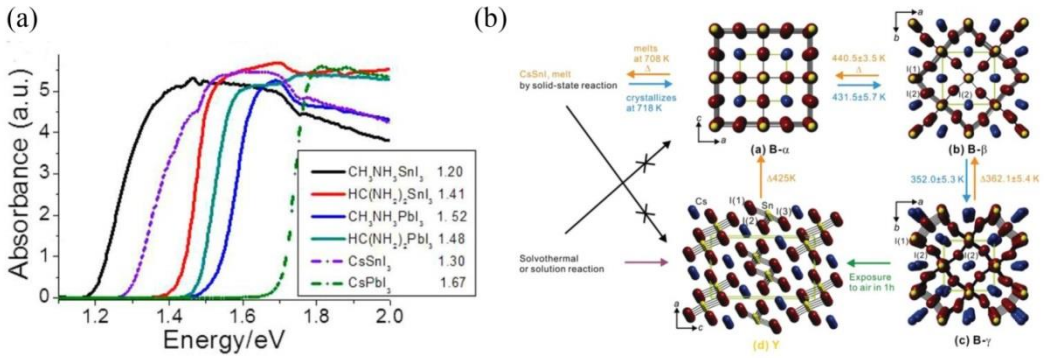

Figure 2.7 (a) Electronic absorption spectra of various perovskite compounds[46]. (b) Crystal structure of four $CsSnI_3$ polymorphs and their phase transformation process[54].

$MASnI_3$ has an optical bandgap of 1.2−1.4 eV[46, 51], which enables it much broader absorption spectrum compared with its $MAPbI_3$ counterpart (**Figure 2.7**a). Through fluorescence quenching measurements, Lin ma et al. estimated the carrier diffusion lengths in the $MASnI_3$ film, which can be as long as 500 nm[55]. Snith et al. first reported the entire lead-free $MASnI_3$ based perovskite solar cells[56]. They used traditional normal structure with mesoporous TiO_2 as scaffold, achieving a PCE of 6.40%.

Similar to their lead analogue, FA^+ is another highly investigated organic cation for tin-based perovskites. Different from $FAPbI_3$, which has yellow δ phase and dark α phase, $FASnI_3$ has only one stable phase up to 200 ℃[46, 57, 58]. Besides, due to the larger cation size of FA, $FASnI_3$ has a larger bandgap than that of $MASnI_3$ (Figure 2.7a)[59]. In 2015, Koh et al. used $FASnI_3$ as light absorbing layer for photovoltaic application, taking advantage of light harvesting from the infrared region, high current density of 24.45 mA cm^{-2} was achieved[60].

Because of its high thermal stability, all-inorganic lead-free $CsSnI_3$ also attracted intensive investigation[61, 62]. Typically, $CsSnI_3$ has two polymorphs at room temperature[63], one is yellow phase (Y) with a 1-D double-chain structure, and the other is black (B-γ) with a 3D perovskite structure. The Y phase can transform to black cubic phase (B-α) when the former is heated above 425 K under inert environment[54, 64]. With the temperature going down, the black cubic perovskite phase (B-α) gradually transforms to black tetragonal phase (B-β) at 426 K and black orthorhombic phase (B-γ) at 351 K. The phase transformation of $CsSnI_3$ is illustrated in Figure 2.7b. Moreover, the B-γ $CsSnI_3$ phase will be oxidized to Cs_2SnI_6 after exposure to air[65]. The black B-γ phase $CsSnI_3$ has a direct bandgap of ~1.3 eV[66, 67] and high charge carrier mobility[62], making it promising material for solar cell application. The potential of $CsSnI_3$ as an absorber for PSCs was discovered by Mathews et al., and they got a PCE of 2.02%[68].

2.5.2 Defect Physics of Tin-based Perovskites

The outer ns^2 electron structure of metal ions has great influence on the optoelectronic properties of perovskite materials[45, 69]. Unlike Pb^{2+}, the much active $5s^2$ electrons of Sn^{2+} can be easily oxidized to Sn^{4+} in the ambient air and form Sn vacancy (V_{Sn}) in the crystal lattice of perovskite, resulting in p-type doping of the material and limited photoexcited carrier diffusion length[56]. Based on calculation methods, Zhao et al. indicated the A-site cation and synthesis condition could greatly influence the defect states of tin-based perovskites[59]. For $MASnI_3$ system, it was found that V_{Sn} was the dominant defect under different synthesis conditions due to the low formation energy of V_{Sn} resulted from the strong Sn 5s-I 5p antibonding coupling. Because of the larger ionic size of FA^+ and longer Sn-I bond, the Sn 5s-I 5p antibonding coupling in $FASnI_3$ is weaker than that of $MASnI_3$, resulting in higher V_{Sn} formation energy in $FASnI_3$ (**Figure 2.8**a,c). Then, the conductivity of $FASnI_3$ can be tuned from p-type to intrinsic by adjusting the synthesis condition while $MASnI_3$ has high p-type conductivity regardless of the growth conditions.

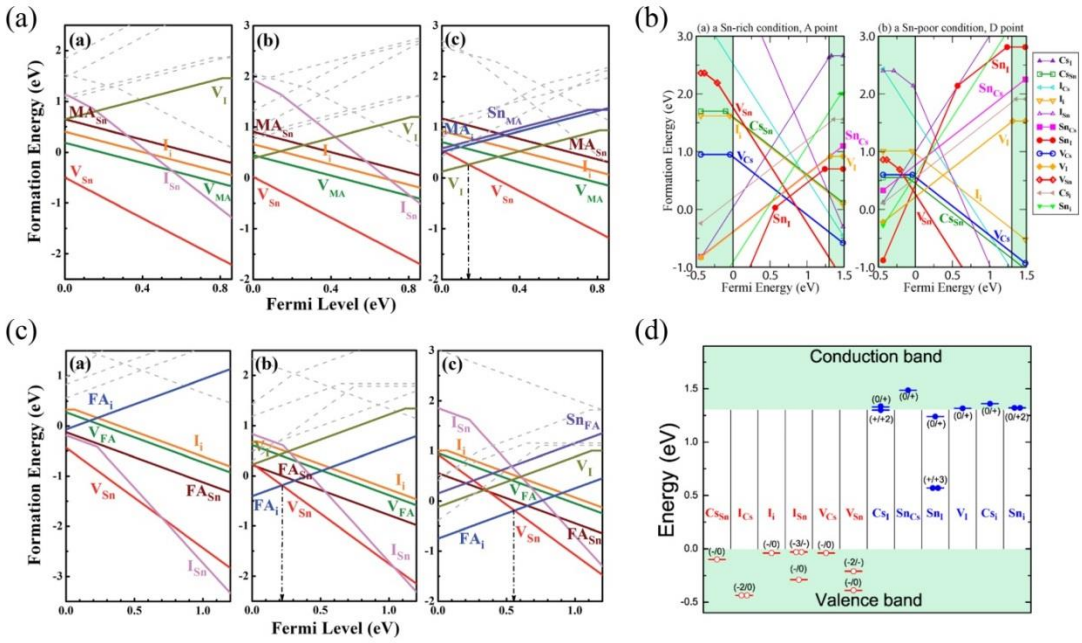

Figure 2.8 Formation energies of intrinsic point defects in (a) $MASnI_3$ and (c) $FASnI_3$ under a) I-rich/Sn-poor, b) moderate, c) I-poor/Sn-rich condition, respectively[59]. (b) Calculated formation energy of defects in $CsSnI_3$ under Sn-rich and Sn-poor condition, respectively. (d) Calculated transition energy levels of various intrinsic defects, acceptor and donor defects levels are denoted by red and blue lines, respectively[70].

Xie and co-workers used theoretical calculations to explore the degradation mechanism of $MASnI_3$ at the atomic level[71]. The Sn-I bond plays a crucial role in the stability of perovskite surface, and H_2O will form a H-I bond while O_2 will form a Sn-O bond with the perovskite surface, which will weaken the bond strength of Sn-I bond. Based on this investigation, more attention should be paid to avoid the formation of HI molecules and thus to enhance the stability of tin-based perovskites. For the inorganic $CsSnI_3$ system, Wei can co-workers depicted the strong Sn 5s-I 5p antibonding coupling caused low V_{Sn} formation energy, leading to high p-type conductivity under Sn-poor synthesis condition[70]. On the other hand, the density of V_{Sn} can be reduced under Sn-rich synthesis environment (Figure 2.8b,d). Thus, Sn(II) halide salt compensations like SnF_2, $SnCl_2$ and SnI_2 have been introduced to create tin-rich condition during growth of tin-based perovskites to reduce the doping density[72].

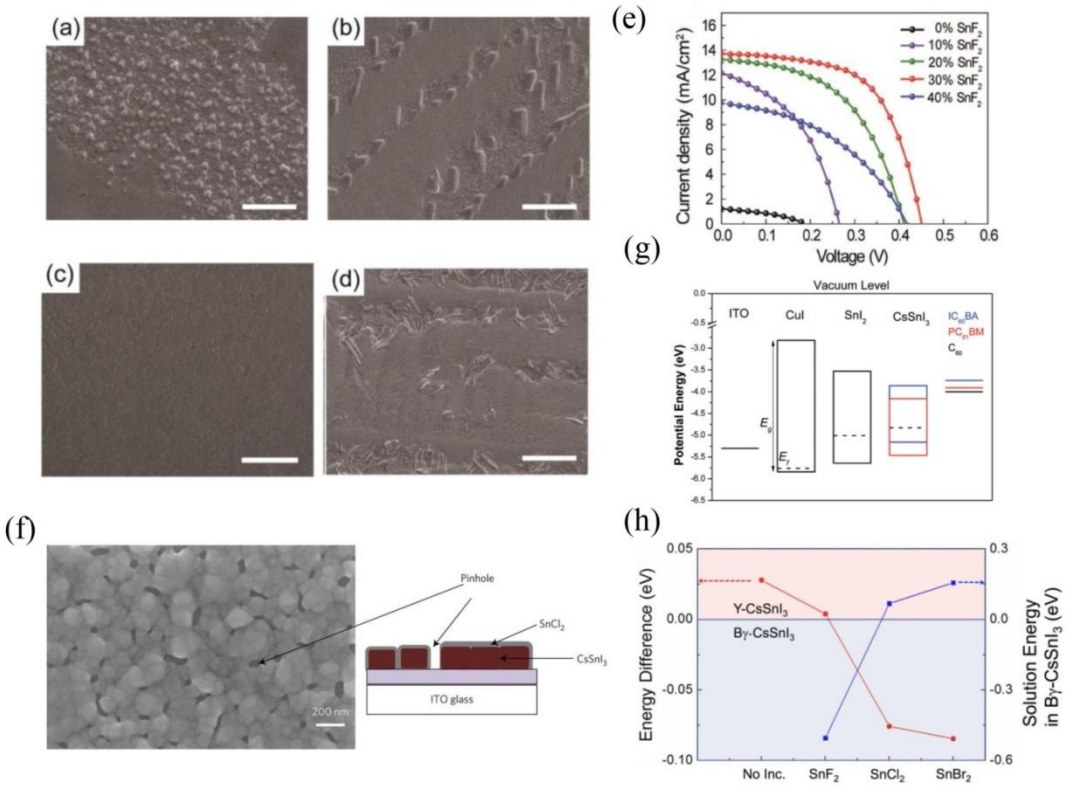

Figure 2.9 (a-d) SEM images of $MASnIBr_2$ perovskite films with various contents of SnF_2, a-0 mol%, b-20 mol%, c-30 mol%, d-40 mol%. The scale bar is 3 μm. (e) J-V curves of $MASnIBr_2$ based solar cells with different amounts of SnF_2[73]. (f) SEM image of $CsSnI_3$ film with 10 mol% $SnCl_2$ and the proposed film structure. (g) Schematic energy alignment diagram of the device[74]. (h) Total energy difference between two $CsSnI_3$ polymorphs and solution energies using different SnX_2. It should be noted that negative energy means better phase stability[75].

SnF_2 was first introduced by In Chung et al. to dope $CsSnI_3$, which was later used as HTM in dye sensitized solar cells[76]. Addition of SnF_2 into $CsSnI_3$ can reduce Sn vacancies was first demonstrated by Kumar et al. in 2014[68], which makes $CsSnI_3$ less conductive, and high current density of 22 mA cm^{-2} was achieved in PSCs. It is found that with 20 % excess SnF_2 doping, the carrier density dropped 2 orders of magnitude compared with pristine $CsSnI_3$, which makes $CsSnI_3$ functional as light absorber in solar cells. In 2015, the same group investigated the effects of doping SnF_2 in $FASnI_3$[60]. With 20% SnF_2 doping, the X-ray photoelectron spectroscopy (XPS) data showed the mere presence of Sn^{2+} but no Sn^{4+}, indicating that all tin perovskite samples were in the unoxidized state. The addition of 20 mol% SnF_2 leads to the increase of current density from 2.14 mA cm^{-2} to 12.4 mA cm^{-2}, yielding an overall PCE of 1.41 % based on a normal mesoporous structure. Because of the short carrier

diffusion length in tin-based perovskites, they further optimized the thickness of mesoporous TiO_2 layer and a best PCE of 2.10% was obtained. In addition, Min and co-workers showed that SnF_2 can be beneficial for the crystal growth of tin-based perovskite[73]. Because of its limited solubility, SnF_2 will be the first precipitate during the spin-coating process. These SnF_2 particles will create more nucleation sites and thus enable more uniform and compact perovskite film, as shown in **Figure 2.9**a-d. With improved perovskite film quality and reduced carrier recombination, the 30 mol% SnF_2 added $MASnIBr_2$ based solar cells achieved a best PCE of 3.7% (Figure 2.9e). Hartmann et al. studied the impact of SnF_2 on the electronic structure of $CsSnBr_3$, and they found the addition of 20 mol% SnF_2 could suppress the oxidation of Sn^{2+} to Sn^{4+} [77]. Currently, SnF_2 is incorporated into most tin-based PSCs to get good photoelectric performance[78-80].

$SnCl_2$ is a common used reducing agent[81], and Marshall et al. added it to $CsSnI_3$ to improve device performance[82]. Using high-resolution XPS analysis, they found that $SnCl_2$ was present at the perovskite surface, and this $SnCl_2$ layer would function as desiccant to improve the stability of $CsSnI_3$ (Figure 2.9f). They also analyzed the effect of different tin halide additives ($SnCl_2$, $SnBr_2$, SnI_2 and SnF_2), and a simplified device architecture (ITO/$CsSnI_3$/$PC_{61}BM$/BCP/Al) was used to investigate the influence of various additives doping on the device performance. Devices with $SnCl_2$ as additive got the best PCE of 3.56%. Surprisingly, the device performance improved greatly after storage under nitrogen. Improved crystallization of the fullerene electron transport layer (PCBM) by intense light illumination when the devices were subject to test[83] and n-type doping of the fullerene layer by $SnCl_2$ contributed to the increase of the device performance.

SnI_2 was also used as excess tin source to compensate the missing Sn^{2+}. Hatton et al. prepared $CsSnI_3$ perovskite films with extra SnI_2 in the precursor solution[74]. Their devices have an inverted planar structure with CuI as the hole transport layer and fullerene as the electron transport layer. The devices with excess SnI_2 exhibited a champion open voltage (V_{OC}) of ~0.55 eV, which was twice compared with that for a previous $CsSnI_3$ based PSC[68]. They also pointed out that the energetics at the $CsSnI_3$/fullerene interface had great effect on the open voltage, and the corresponding

energy level of the device is given in Figure 2.9g. Increase in the LUMO of the fullerene ETM contributes to the increase of the device V_{OC}, which is in accordance with a reduction in the energy lost when electron moving from $CsSnI_3$ to the ETM as previously proved in organic solar cells[84].

Heo and co-workers studied different SnX_2 (X=F, Cl, Br) additives on the photovoltaic performance and device stability of $CsSnI_3$ based PSCs, and found $SnBr_2$ was the best additive for $CsSnI_3$[75]. X-ray diffraction (XRD) and UV-visible absorption spectra corroborated that $SnBr_2$ was the most effective additive in stabilizing the B-γ $CsSnI_3$ phase, and the device with $SnBr_2$ showed the highest PCE of 4.30% with enhanced stability. Density functional theory (DFT) calculations suggest that SnX_2 additive tend to occupy interstitial sites to stabilize the B-γ $CsSnI_3$ phase and $SnBr_2$ is the most effective (Figure 2.9h). On the other hand, SnX_2 shows the function of surface passivation by forming adsorption layer on $CsSnI_3$ slab, and the adsorption energy of $SnBr_2$ is the largest. Thus, $SnBr_2$ is the most suitable additive for $CsSnI_3$ to improve both device performance and stability.

2.5.3 Reducing Agents

To restrain the notorious oxidation of Sn^{2+} to Sn^{4+}, it is necessary to add some reducing agents during the preparation of tin-based perovskites. Hypophosphorous acid (HPA) is a common reducing agent and it has been used in lead-based perovskite to improve the film quality by reducing the oxidized I_2 back to I^- and facilitating an improved stoichiometry in the perovskite crystal[85].

When it comes to tin-based perovskite, Li et al. used all inorganic $CsSnIBr_2$ to study the effect of HPA[61]. Interestingly, the color of the perovskite precursor changed from bright yellow to dark brown upon the addition of HPA solution (**Figure 2.10**a), indicating the formation of new compounds. Time-resolved photoluminescence (TRPL) decay measurement showed dramatic increase in charge carrier lifetime with the addition of HPA, indicating that HPA can reduce tin vacancies in the perovskite film. Using a normal mesoporous device structure, an average PCE of 3.0% was achieved. Moreover, the encapsulated all inorganic PSCs showed great long term stability, retaining 103% of its initial performance after 77 days in ambient

environment (Figure 2.10b).

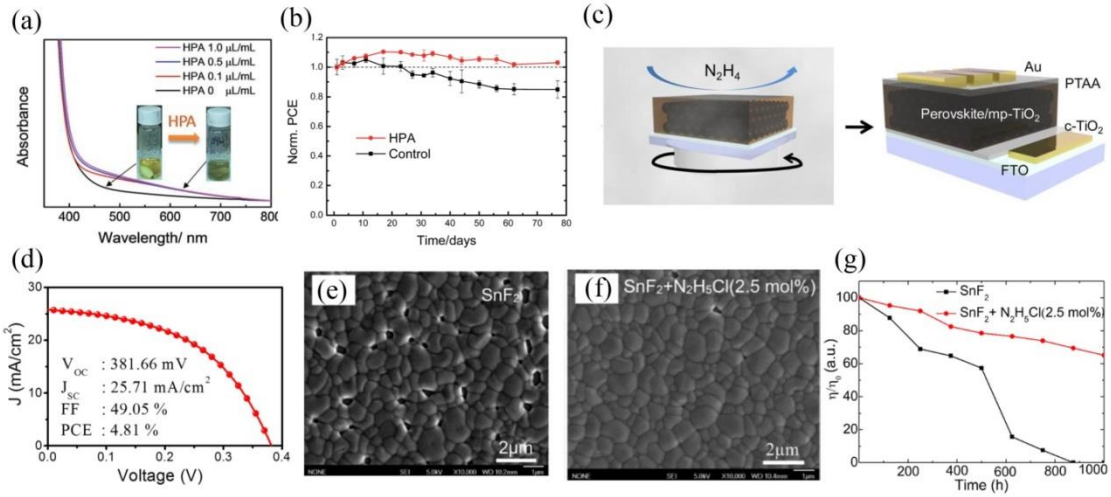

Figure 2.10 (a) UV-vis absorption spectra of $CsSnIBr_2$ solution with various amounts of HPA additives. (b) Stability test of the encapsulated $CsSnIBr_2$ solar cells[61]. (c) Illustration of reducing atmosphere during the device fabrication process and the device structure[86]. (d) J-V curves of the $CsSnI_3$ based solar cells with best performance[87]. SEM images of $FASnI_3$ film (e) no N_2H_5Cl additive, (f) 2.5 mol% N_2H_5Cl additive. (g) Stability test of the device with/without N_2H_5Cl[88].

Hydrazine is another well recognized reducing agent and it has been used during preparation of copper indium gallium selenide (CIGS) solar cells[89]. Song et al. introduced N_2H_4 vapors (Figure 2.10c) during the crystallization of tin-based perovskites in the presence of SnF_2 to suppress the oxidation of Sn^{2+}[86]. XPS measurements indicated that the ratio of Sn^{4+}/Sn^{2+} reduced significantly when the perovskite films were prepared under hydrazine vapor along with the presence of SnF_2. With a normal structure using mesoporous TiO_2 layer as substrate, $CsSnI_3$ based device showed current density as high as 30 mA cm^{-2}, resulting in an overall PCE of 1.83%. Later on, the same group used excess SnI_2 as tin compensator in combination with a reducing hydrazine vapor atmosphere to prepare $CsSnI_3$ based solar cells, achieving PCE up to 4.81% (Figure 2.10d)[87]. Moreover, they also studied the relation between the device performance and the AI/SnI_2 ratio (A=Cs, FA and MA), and only $FASnI_3$ can function normally close to the stoichiometric ratio. This may reflect the different formation energy of Sn^{2+} vacancies in different tin-based perovskites, and the formation energy is the highest in $FASnI_3$[59]. Recently, Kayesh and co-workers introduced hydrazinium chloride (N_2H_5Cl) in precursor solvent to prepare $FASnI_3$ perovskite film[88]. Hydrazine compounds are common reducing agents[90] which can

release electrons to suppress the oxidation of Sn^{2+}. XPS measurement confirmed that the integration of N_2H_5Cl reduced the Sn^{4+} content by 20%, which contributed to suppressed carrier recombination. Moreover, the chloride ions from N_2H_5Cl can lead to perovskite intermediate, which is beneficial for the growth of larger perovskite grains (Figure 2.10e-f)[91]. Based on an inverted planar structure, the device with 2.5 mol% N_2H_5Cl achieved a PCE of 5.4%, which was nearly twice higher compared with the control one. In terms of stability, the PSCs with N_2H_5Cl remained 65% of the original performance after storing in glovebox for 1000 h, while the plain device degraded to fail after 850 h (Figure 2.10g).

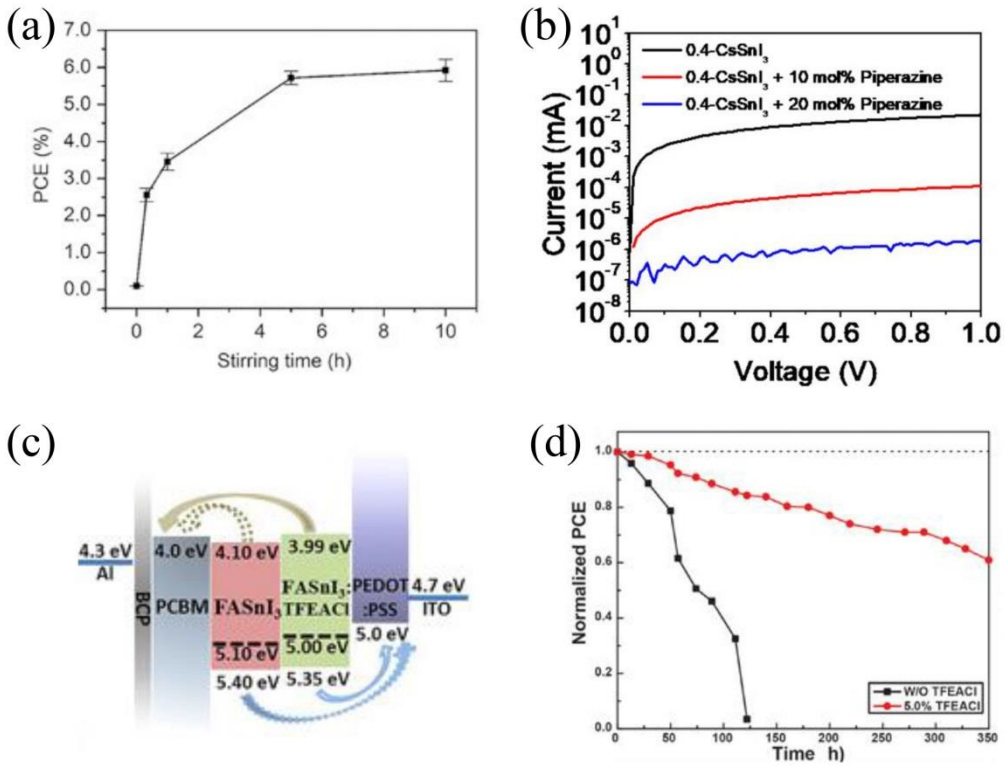

Figure 2.11 (a) Device performance prepared from different Sn powder stirring time[92]. (b) I-V curves of $CsSnI_3$ film prepared from different condition[93]. (c) Energy level diagram of the PSCs based on different perovskite films. (d) Light soaking tests of the solar cells under a continuous simulated solar irradiation[94].

The purity of SnI_2 has great impact on the photovoltaic performance of tin-based PSCs, and it is reported that PSCs based on 99% SnI_2 cannot work and 99.99% SnI_2 is the optimal[68]. Gu et.al used Sn powder to purify low purity SnI_2 (99%) to reduce the Sn^{4+} content[92]. Sn powder was added to the perovskite precursor solution and stirred for about 5 hours to ensure the completion of redox reaction (**Figure 2.11**a), i.e. Sn^{4+}

+ $Sn=2Sn^{2+}$. Inverted device structure was prepared to evaluate the Sn powder reduction on the photovoltaic performance, and a best PCE of 6.75% with V_{OC} of 0.58 V, J_{SC} of 17.5 mA cm^{-2} and FF of 66.3% was achieved. Meantime, the unencapsulated device showed good shelf stability, remaining 90% of its original PCE after storing in glovebox for 860 h. This work provides a low cost way to purify SnI_2 source of inferior purity to get good device performance.

Similar with the character of hydrazine, piperazine was introduced to $CsSnI_3$ to suppress the self-doping effect and improve the device performance[93]. Tze-Bin and co-workers added piperazine to $CsSnI_3$ perovskite with SnI_2 as excess tin source[87], and they found that diamine group of piperazine can form strong interaction with SnI_2 to improve the perovskite film coverage. Meantime, 20% piperazine modified $CsSnI_3$ film showed 4 orders of magnitude resistance than that of the reference film (Figure 2.11b), demonstrating its effectiveness in suppressing self-doping. After optimizing the thickness of mesoporous TiO_2 layer, a best PCE of 3.83% was achieved. In another work, Hoshi et al. added 5-ammonium valeric acid (5-AVAI) to enhance the oxidation stability of $MASnI_3$[95]. 5-AVAI has been used in lead-based perovskite to improve charge-carrier lifetime and device stability by forming $(5\text{-AVAI})_xMA_{1-x}PbI_3$[96]. However, the cubic perovskite structure of $MASnI_3$ is retained regardless of the addition of 5-AVAI, which is different from the situation of $MAPbI_3$. The improved oxidation stability may come from the formation of 5-AVAI layer on the surface of the $MASnI_3$, which stems from the hydrogen bonds formed between NH^{3+} from 5-AVAI and I^- ions from the SnI_6^{4-} octahedra[97]. Similarly, Islam and co-workers used 5-AVAI to enhance the oxidation stability of $FASnI_3$ perovskite film[98]. Proton nuclear magnetic resonance (^1H NMR) spectra confirmed the hydrogen bond interaction between 5-AVAI and iodide from SnI_6^{4-} octahedral. XPS measurements found the existence of 5-AVAI on the perovskite film surface, which would be beneficial for the enhanced air stability of perovskite film. Benefiting from improved perovskite film crystallinity and reduced charge recombination, the device performance increased from 3.4% to 7.0% with 3 mol% 5-AVAI. Recently, Yu and co-workers used 2,2,2-trifluoroethylamine hydrochloride (TFEACl) together with SnF_2 to improve the efficiency and stability of $FASnI_3$ solar cells[94]. FTIR and XPS confirmed the presence of TFEACl in the perovskite film. XRD patterns of the

perovskite films show obvious shift, which indicates the reduction of the lattice constant and the incorporation of Cl into the crystal lattice. Moreover, the incorporation of Cl can tune the work function of these perovskite films to result in better energy alignment between perovskites and charge transport layer (Figure 2.11c), which can contribute to improved charge collection and better device performance. With 5mol% TFECl, the device performance increased from 3.63% to 5.3% with enhanced light soaking stability (Figure 2.11d).

In a recent work, Jiang et al. introduced reducing additive trihydrazine dihydriodide (THDH) to the perovskite precursor solution to reduce the background carrier density[99]. ^{1}H-NMR spectrum implied that one N_2H_4 molecular in THDH would be evaporated during the preparation of perovskite film and only N_2H_5I remained in the final perovskite film. Because of the reducing nature of hydrazine, the oxidation of Sn^{2+} in the perovskite was significantly suppressed. Moreover, the remaining N_2H_5I can interact with perovskite to improve the morphology of the $FASnI_3$ film[88]. Using 99% purity SnI_2 as tin source, the device with 5% THDH got an efficiency of 8.48%. Very recently, He et al. introduced 4-fluorobenzohydrazide (FBH) as additive to form an antioxidant capping layer on the $FASnI_3$ perovskite film[100]. FTIR spectroscopy confirmed the coordination effect between the C=O group from FBH and Sn^{2+}, which favored the formation of large oriented perovskite grain. Meantime, ^{1}H NMR spectrum verified the reduction of Sn^{4+} by the hydrazide group in FBH. DFT calculation indicated increased energy barrier for oxygen absorption after FBH modification, which could retard the oxidization process of perovskite. At normal oxygen condition, the device performance increased from 8.34% to 9.47% with FBH capping layer. Interestingly, at high oxygen condition of 100 parts per million (ppm), the FBH-based device achieved a PCE of 9.03% while the control device only got a PCE of 4.14% due to serious oxidation. In another work, Zhang and co-workers introduced cobaltocene ($CoCp_2$) as electron donor to suppress the oxidation of $CsSnI_3$ perovskite[101]. XPS scans indicated the oxidation state of cobalt ions changed from Co^{2+} to Co^{3+}, suggesting electron transfer from $CoCp_2$ to $CsSnI_3$ to build a reduction environment, which was favorable for the reduction of Sn^{4+} oxidation. Based on mesoporous $TiO_2/Al_2O_3/NiO_x$/carbon structure, the device got a maximum PCE of 3.0%. This work suggests that introducing donor elements could be a promising way

to suppress Sn^{2+} oxidation.

2.5.4 Additives to Control the Morphology of Tin-based Perovskites

Uniform and pinhole free perovskite film is quite important for good photovoltaic performance by avoiding the undesirable charge recombination. However, Sn^{2+} has higher Lewis acidity than Pb^{2+}, which causes uncontrollable crystallization during the spin-coating process and leaves pinholes on the perovskite film[51, 102]. The unsatisfactory film quality usually results in poor device performance or even short circuit due to the direct contact between the two electrodes through pinholes. Therefore, it is of great importance to develop novel methods to get good quality tin-based perovskite films for better device performance and long term device stability.

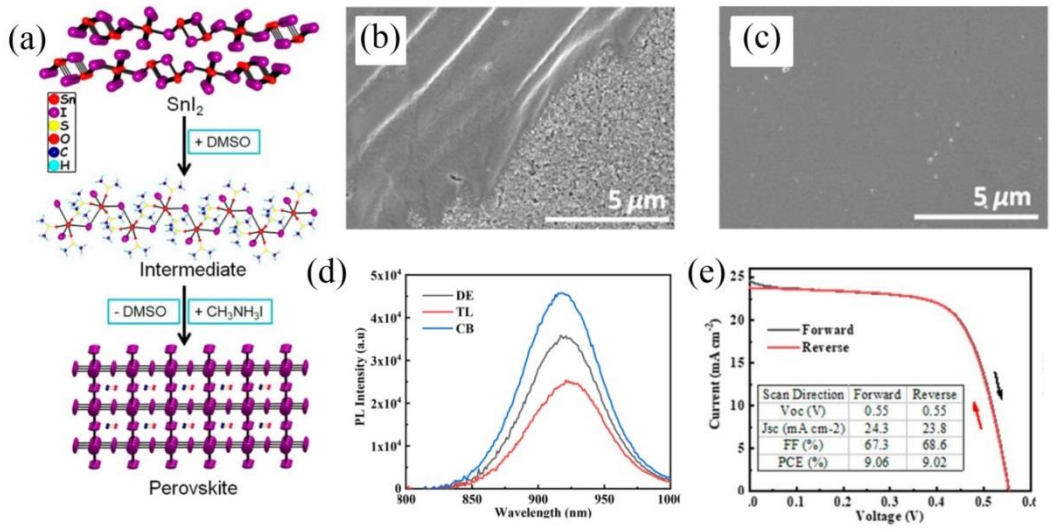

Figure 2.12 (a) Schematic of perovskite film formation from SnI_2·3DMSO intermediate. SEM images of $MASnI_3$ perovskite film using different solvent, (b) DMF, (c) DMSO. Uncovered TiO_2 surface was observed when DMF was used as solvent[103]. (d) PL spectra of $FA_{0.75}MA_{0.25}SnI_3$ film treated with different antisolvent. (e) J-V curve of the champion device[104].

Solvent engineering has been one of the most effective methods to prepare high quality lead-based perovskite films[105, 106]. Briefly, high quality perovskite films are prepared based on the Lewis acid-base adduct approach. The solvents like DMF, dimethyl sulfoxide (DMSO), n-methyl pyrrolidone (NMP) etc.) to dissolve MAI and PbI_2 are polar aprotic solvents, which can act as Lewis bases. On the other hand, PbI_2 is known to be a Lewis acid. Thus, intermediate phase of MAI·PbI_2·DMSO will form

through the weak chemical interaction[107], and the intermediate phase greatly influences the crystal growth and morphology of perovskite film[108].

In the case of tin-based perovskite, Hao et al. was the first to study the solvent effects on the crystallization of the $MASnI_3$ perovskite films[103]. A 3DMSO·SnI_2 intermediate phase enables homogeneous nucleation and an adjustable perovskite growth rate (**Figure 2.12**a), helping to obtain uniform and pinhole-free perovskite films (Figure 2.12b,c). The heterojunction depleted solar cells without hole transporting layer based on these high quality $MASnI_3$ films were prepared, achieving photocurrent density up to 21 mA cm^{-2} and an overall PCE of 3.15%. It should be mentioned the devices using DMF as solvent often suffered short circuits. This work highlights the importance of solvent engineering in achieving improved perovskite film morphology.

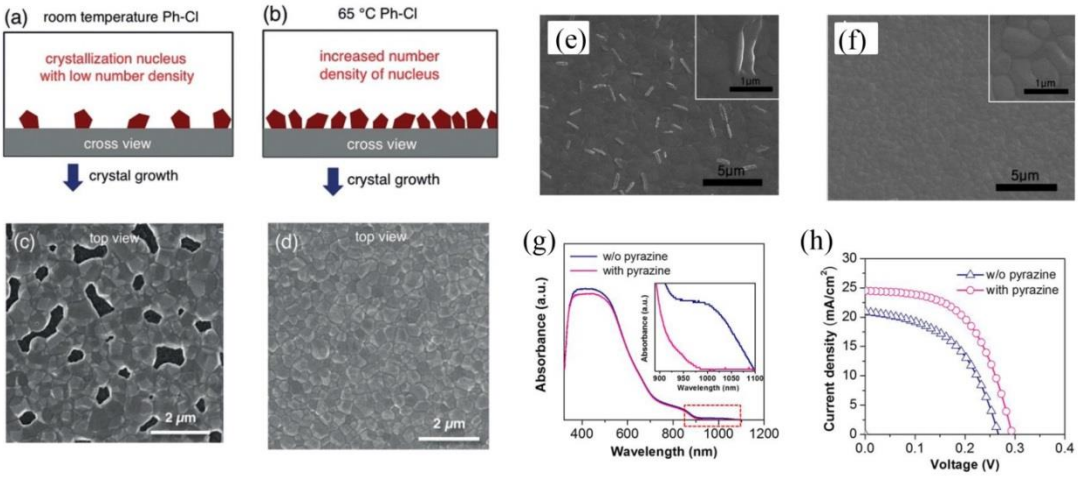

Figure 2.13 Crystal nucleation of perovskite film treated with (a) room temperature antisolvent and (b) antisolvent at 65 ℃. SEM images of $FA_{0.75}MA_{0.25}SnI_3$ perovskite film prepared with (c) room temperature chlorobenzene and (d) 65 ℃ chlorobenzene[109]. SEM images of $FASnI_3$ perovskite film prepared (e) without pyrazine and (f) with pyrazine. (g) Absorption spectra of $FASnI_3$ films with and without pyrazine. The absorption band from 900 to 1100 nm reflects the reduced defect center. (h) J-V curves of $FASnI_3$ based solar cells with and without pyrazine[110].

Liu et al. compared different antisolvent treatment on the film quality and electrical properties of $FA_{0.75}MA_{0.25}SnI_3$ perovskite film[104]. Among diethyl ether (DE), toluene (TL) and chlorobenzene (CB), CB treatment can get dense and uniform perovskite film with reduced charge carrier recombination (Figure 2.12d). Chlorobenzene has

suitable boiling point and miscibility, which is important to get a balance between nucleation and crystal growth of perovskite film[111]. With improved film morphology and reduced recombination, the device achieved a champion PCE of 9.06% (Figure 2.12e).

Since temperature can affect the miscibility of two solvents, then the temperature of antisolvent (chlorobenzene, Ph-Cl) can influence the process of antisolvent treatment[112]. Liu and co-workers systematically studied the effect of antisolvent temperature on the formation of tin-based perovskite film to improve the film coverage[109]. It is proposed that hot antisolvent treatment (HAT) can increase the density of nucleation sites, contributing to high quality perovskite films without pinholes (**Figure 2.13**a-d). Furthermore, they used solvent vapor annealing (SVA) to increase the crystallite size, which was achieved by annealing the perovskite films under DMSO vapor atmosphere. By carefully controlling the vapor density of DMSO during SVA treatment, the average grain size increased from 237 nm to 440 nm, which would reduce trap sites and contribute to better photovoltaic performance. Combining hot antisolvent treatment and solvent vapor annealing, the best PCE reached 7.2%. Later, He and co-workers introduced redissolved $FASnI_3$ crystals as precursor solution to prepare high quality perovskite film[113]. They used a temperature-lowering method to grow bulk $FASnI_3$ crystals and redissolve the $FASnI_3$ crystal to obtain the precursor solution. Meantime, antisolvent free high-vacuum quick-annealing technique was used to fabricate $FASnI_3$ solar cells. Compared with precursor solution consisting monomer (FAI, SnI_2), the redissolved crystal solution may have more $[SnI_6]^{4-}$ cages, which will contribute to uniform perovskite films with large grains and low density of deep defects. The champion device achieved an overall PCE of 8.9% and a steady-state efficiency of 8.55%. This work provides new method for the preparation of high quality tin-based perovskite film.

While SnF_2 is a common additive to inhibit the oxidation of Sn^{2+} and reduce the conductivity of tin-based perovskite, excess SnF_2 can induce phase separation on the surface of the perovskite film, which will be bad for the device performance[78]. In this regard, Lee et al. selected pyrazine as a mediator to form SnF_2-pyrazine complex, which resulted in homogeneous dispersion of SnF_2 into perovskite film[110]. As a result,

smooth and dense $FASnI_3$ film without phase separation was obtained (Figure 2.13e,f). Moreover, the combination of pyrazine and SnF_2 can reduce trap states, which contributed to the improved photovoltaic performance (Figure 2.13g)[114]. With a normal mesoporous structure, a PCE of 4.8% was obtained with good reproducibility (Figure 2.13h).

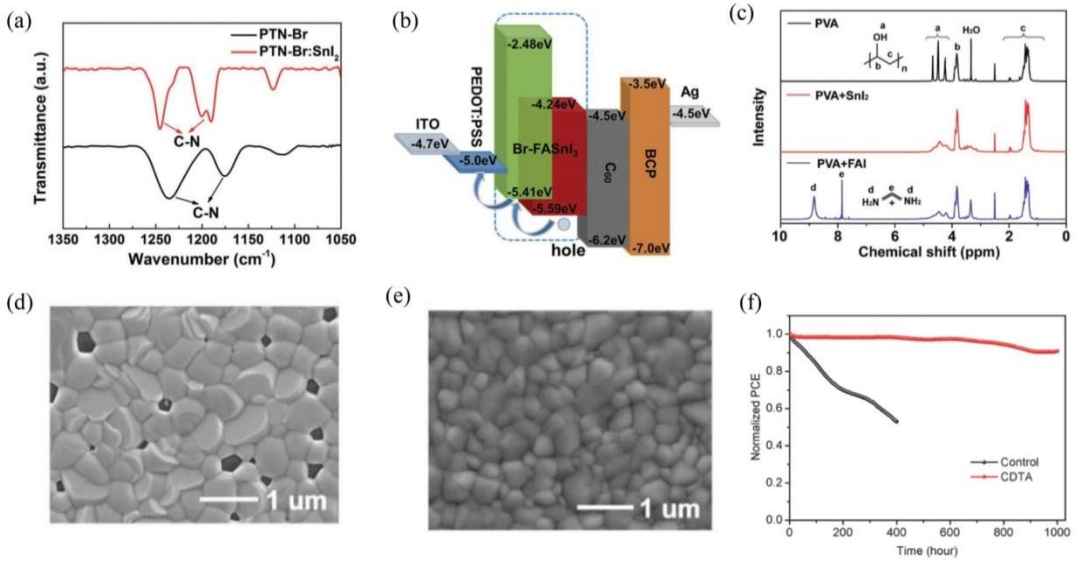

Figure 2.14 (a) FTIR spectroscopy of PTN-Br and PTN-Br-SnI_2 complex. (b) Energy level alignment of PTN-Br modified PSCs[115]. (c) ^1H NMR spectra of PVA, PVA-SnI_2 and PVA-FAI. SEM images of (d) $FASnI_3$ perovskite film and (e) PVA modified $FASnI_3$ perovskite film[116]. (f) Stability test of PSCs under light soaking (AM 1.5 G, 100 mW cm^{-2}) [117].

Based on similar principle, Duyen et al. used trienthyphosphine (TEP) as Lewis base to form intermediate complexes with Sn^{2+} species[118]. With a small amount of TEP in the perovskite precursor solution, the perovskite crystallization process was slowed down and the film morphology was improved. Specifically, solar cells based on the high quality 2D $(BA)_2(MA)_{n-1}Sn_nI_{3n+1}$ perovskite films showed improved stability, retaining more than 90% of its initial performance after 1 month. Trimethylamine (TMA) is a soft Lewis base, which can form SnF_2-TMA complex through Lewis acid-base interaction. Based on this principle, Zhu et al. employed TMA to facilitate homogeneous film formation of $FASnI_3$ perovskite[119]. Using two-step deposition method, PCE of 7.09% was obtained in planar inverted PSCs. Recently, Hu and co-workers used poly(methyl methacrylate) (PMMA) as additive to improve the film quality and electrical properties of $FASnI_3$ perovskite films[120]. The

C=O bond of PMMA can act as electron donor to interact with ammonium group, which can help to optimize the morphology of perovskite film[121]. Moreover, the PMMA modification can reduce trap density of perovskite film, which is beneficial for the improvement of fill factor and open voltage. With the addition of PMMA, the photovoltaic performance increased from 2.78% to 3.62% and the device showed much improved stability.

To improve hole transportation between tin-based perovskite and hole transport layer, Chen et. al introduced poly[tetraphenylethene3,3′-(((2,2-diphenylethene-1,1-diyl)bis(4,1-phenylene))bis(oxy))bis(*N*,*N*-dimethylpropan-1-amine) tetraphenylethene] (PTN-Br) into $FASnI_3$ perovskite precursor to form a bulk heterojunction film[115]. FTIR spectroscopy confirmed the interaction between SnI_2 and PTN-Br to form Lewis adducts to passivate the trap states of perovskite films (**Figure 2.14**a). Moreover, the PTN-Br has suitable energy level to form a gradient band alignment between perovskite and HTM to enhance hole transportation and collection (Figure 2.14b). With the introduction of PTN-Br, the device performance increased from 5.12% to 7.94% with much enhanced stability. Later, Chen and co-workers introduced poly(ethylene-co-vinyl acetate) (EVA) to regulate the crystallization of $FASnI_3$ perovskite[122]. The C=O group of EVA could form Lewis acid-base complexation with uncoordinated tin atoms, which can slow down the crystalline rate of $FASnI_3$ and favor orientated growth of perovskite grains. The champion device got a PCE of 7.72% with prolonger environmental stability. In a recent work, Meng and co-workers used poly(vinyl alcohol) (PVA) to slow down the crystalline rate of $FASnI_3$ perovskite[116]. ^1H NMR measurements confirmed the formation of hydrogen bonding between PVA molecule and iodide ions, and these hydrogen bonding interactions could introduce nucleation sites to slow down the crystal growth of $FASnI_3$ film (Figure 2.14c). As a result, homogeneous and pinhole-free perovskite films were obtained (Figure 2.14d,e). Moreover, the hydrogen bonding interactions at the grain boundary can suppress the migration of iodide ions, which will contribute to the enhanced long term stability of the devices. In addition, the hydroxyl groups in PVA have antioxidant property[123], which can be oxidized to aldehydes or carboxylic acids to retard the oxidation of Sn^{2+}. Based on planar inverted structure, the champion device with PVA got an efficiency of

8.92%. Interestingly, the encapsulated $FASnI_3$-PVA based devices showed enhanced operational stability, almost no decay in PCE was observed after 400 h under one sun illumination in the ambient air. The much improved operational stability could be ascribed to the suppressed iodide ions diffusion and the antioxidant property of PVA.

Islam and co-workers used post deposition vapor annealing (PDVA) process with MACl to prepare large area tin-based PSCs[124]. Compared with normal annealing method, this MACl vapor method can help to fabricate uniform and pinhole-free $FASnI_3$ films with increased crystallinity and decreased defects with an aperture area over 1.02 cm^2. With PDVA process, the efficiency of 1.02 cm^2 solar cells increased from 4.18% to 6.33%. In another work, Hayase et al. used Lewis base ethane-1, 2-diamine (edamine, DAE) post treatment to suppress the charge carrier recombination of tin-based perovskite[125]. FTIR spectroscopy confirmed the presence of edamine on the perovskite surface. Amine group of edamine molecules could stabilize the undercoordinated Sn to reduce charge recombination. XPS measurements indicated that iodide deficiency rather than tin oxidation is the main reason for the large V_{OC} loss. With 0.05 mM edamine post treatment, the champion device achieved an efficiency of 10.18%, which used to be one of the highest reported efficiency for tin-based solar cells. More recently, Wu and co-workers used π-conjugated Lewis based molecules to control the crystallization rate of $FASnI_3$ perovskite[117]. They synthesized three π-conjugated Lewis based molecules and it was found that the electron-donating triphenylamine unit on 2-cyano-3-[5-[4-(diphenylamino)phenyl1]-2

-thienyl]-propenoic acid (CDTA) could result in more stable Lewis adduct during the nucleation process. The FTIR spectroscopy confirmed the coordinated reaction between such molecules and Sn^{2+} components. Meantime, this coordination could slow down the crystallization rate of $FASnI_3$ perovskite and lead to pinhole-free and homogeneous perovskite films. Moreover, the hydrophobicity of aromatic ring on the CDTA molecule could prevent the permeation of moisture into the perovskite lattice thus slow down the oxidation process of $FASnI_3$ films. Based on planar inverted structure, the CDTA treated PSCs got enhanced PCE of 10.17% and certified PCE of 9.39%. The encapsulated PSCs also demonstrated good light soaking stability, maintaining over 90% of its original PCE after 1000 h (Figure 2.14f).

2.6 Sn-Pb Mixed Perovskite Solar Cells

The bandgap of mixed Sn-Pb perovskites can be tuned from 1.2 eV to 1.6 eV, making them ideal light absorbers approaching the Schockley-Queisser limit and low-bandgap perovskite subcells for tandem devices[126-128]. Meantime, the incorporation of lead can simultaneously enhance the device performance and stability. The development of pure tin-based PSCs provides useful insights for preparing Sn-Pb mixed solar cells.

Similar with tin-based perovskite, binary Sn-Pb mixed perovskites also face the problem of easy oxidation of Sn^{2+}, which causes high trap densities and short carrier lifetime. In 2014, Zuo et al. prepared mixed $MAPb_{1-x}Sn_xI(Cl)$ perovskites from MAI, $PbCl_2$ and $SnCl_2$, and for the first time PCE above 10% was achieved[129]. Xu and co-workers introduced a common antioxidant ascorbic acid (AA) in perovskite precursor to enhance the performance of mixed Sn-Pb PSCs[123]. Besides from retarding the oxidation of Sn^{2+}, the counter anion of AA can function as Lewis base to interact with SnI_2/PbI_2 to form intermediate and influence the crystallization kinetics of perovskite. With AA as additive, $MA_{0.5}FA_{0.5}Pb_{0.5}Sn_{0.5}I_3$ based solar cells got an efficiency of 14.01% with improved stability.

Zhu et al. introduced DMSO as capping agent to control the crystallization of Sn-Pb perovskite[130]. It is found that high affinity of DMSO with metal iodides can slow down the reaction rate between MAI and SnI_2/PbI_2, leading to larger perovskite grains and enhanced crystallinity. Moreover, energy dispersive spectroscopy (EDS) analysis indicated that DMSO could ameliorate the inhomogeneous distribution of Sn in the alloyed perovskite, which can improve the film quality and thus device performance. Based on planer inverted structure, the best device got PCE of 15.2%. Zong and co-workers used Lewis-adduct SnF_2 3FACl as additive to realize the uniform and continuous distribution of SnF_2 along the grain boundaries of Sn-Pb perovskite, which enhanced the physical properties of these alloyed ideal bandgap halide perovskites (IBHPs)[131]. FTIR spectrum confirmed the Lewis base-acid interaction between SnF_2 and FACl. This coordination is not stable at high temperature, which will realize the uniform distribution of SnF_2 along the grain boundaries in the alloyed perovskite after annealing with the release of FACl

byproduct (**Figure 2.15**a). The tin-rich grain boundary can reduce Sn vacancy concentration and improve the chemical stability of the mixed Sn-Pb perovskite films. The device performance increased from 12.9% to 15.8% with enhanced environmental stability.

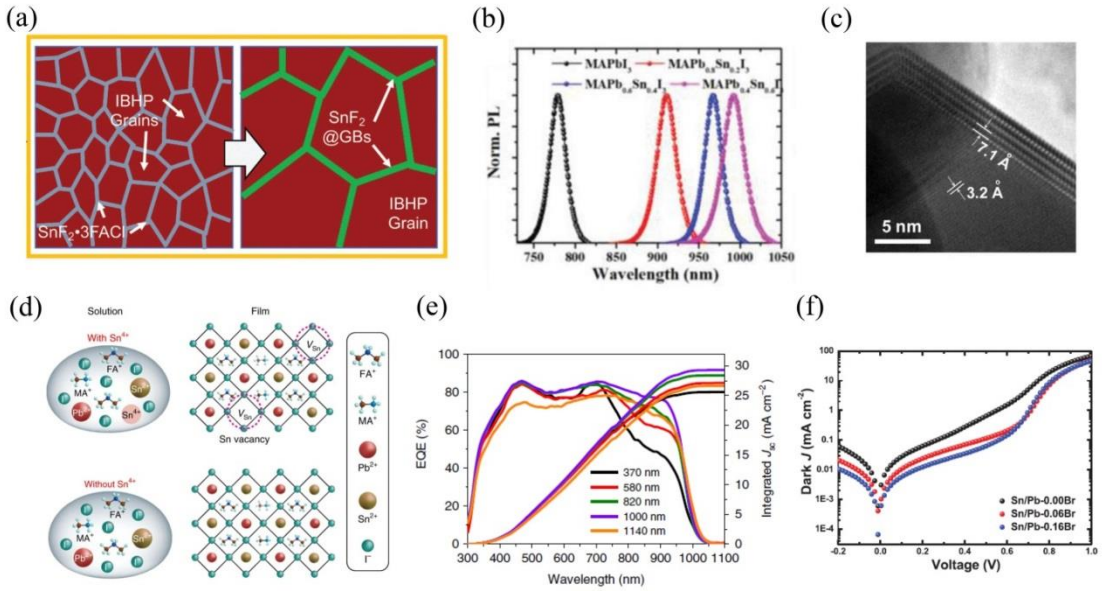

Figure 2.15 (a) Schematic illustration of microstructural evolution in IBHP films with the incorporation of the Lewis-adduct SnF_2·3FACl in the precursor[131]. (b) Steady-state PL spectra of the $MAPb_{1-x}Sn_xI_3$ films[132]. (c) HRTEM image of the grain boundary region of perovskite prepared with GuaSCN as additive[133]. (d) Illustration of the formation of Sn vacancies in perovskite and the suppression of Sn vacancy formation because of the absence of Sn^{4+}[134]. (e) External quantum efficiency (EQE) spectra of PSCs with 0.03mol% Cd^{2+} ions in different perovskite thickness[135]. (f) Dark J-V curves of Sn-Pb PSCs with different Br concentrations[136].

Recently, Zhu et al. used galvanic displacement reaction (GDR) to prepare Sn-Pb binary PSCs[132]. Briefly, they added Sn metal powders to pure Pb perovskite precursor to get Sn-Pb binary precursor solutions by the equation: $Sn(s) + Pb^{2+} \text{---} Sn^{2+} + Pb(s)$. XRD patterns and PL spectroscopy confirmed the formation of $MAPb_{1-x}Sn_xI_3$ precursor solutions (Figure 2.15b), and XPS analysis can be used to find the x value. Using inverted device structure, $MAPb_{0.4}Sn_{0.6}I_3$ based solar cells got an efficiency of 15.76%. Using the same method, $(FAPb_{0.6}Sn_{0.4}I_3)_{0.85}(MAPb_{0.6}Sn_{0.4}Br_3)_{0.15}$ based solar cells got PCE of 18.21%. This method can be used to prepare other mixed metal PSCs. Similarly, Lin and co-workers used metallic Sn powders to prepare narrow bandgap Sn-Pb perovskites[134]. Based on the comproportionation reaction $Sn+Sn^{4+} \text{---} 2Sn^{2+}$, the metallic Sn powder can suppress the oxidation of Sn^{2+} (Figure 2.15d). With the

introduction of Sn power, the device performance increased from 18.3% to 21.1%, which is one of the highest efficiency among Sn-Pb mixed PSCs. Using similar in-situ reduction method by excess Sn powder, Jiang and co-workers got PCE of 20.7% based on $(FASnI_3)_{0.6}(MAPbI_3)_{0.4}$ perovskite film[137].

Similar with previous work, Kapil et al. added Cs to the lattice of $(FASnI_3)_{0.5}(MAPbI_3)_{0.5}$ perovskite to reduce the lattice strain and improve the intrinsic stability of perovskites[138]. XRD patterns showed gradual shift to higher values, indicating the incorporation of Cs^+ into the lattice and shrink of the lattice. Derived from the Williamson-Hall plot, it was found the strain first relaxed with small amount addition of Cs^+ then increased with large amount of Cs^+ incorporation. As confirmed by thermally stimulated current (TSC) measurements, both shallow and deep level trap densities dropped with proper amount of Cs^+ addition. Moreover, FTO glasses were used instead of frequently used ITO because FTO has higher transmission in the infrared region, which can help to get higher current density at wavelengths longer than 800 nm. With the incorporation of 2.5% Cs^+, the best PCE of 20.4% was achieved with high current density of 33.14 mA cm^{-2}. Tong and co-workers used guanidinium thiocyanate (GuaSCN) to improve the optoelectronic properties of Sn-Pb mixed perovskites[133]. High resolution transmission electron microscope (HRTEM) image confirmed that a small amount of GuaSCN additive could form a 2D structure at grain boundaries (GBs) (Figure 2.15c), which would passivate GBs and suppress oxidation of Sn^{2+}. Moreover, the GuaSCN additive could enhance the carrier lifetime and thus carrier diffusion lengths, which would result in more light absorption in the infrared radiation (IR) region and collect more photocarriers. 7% GuaSCN modified Sn-Pb mixed PSCs got a PCE of 20.5% with much improved current density. It should be noted that the enhancement of device performance comes from the combination function of GuaSCN other than the single effect of Gua^+ or SCN^-. Recently, Yang and co-workers added cadmium (Cd^{2+}) ions into Sn-Pb perovskite precursor to improve the performance of narrow bandgap solar cells[135]. It is proposed that a very small amount of Cd^{2+} ions can fill the Sn vacancies to reduce the background carrier concentration, which results in enhanced minority carrier mobility and longer carrier diffusion length. The improved properties of Sn-Pb mixed perovskites enabled increased thickness of narrow bandgap perovskite to ensure light absorption in the

near infrared wavelength region (Figure 2.15e). With the introduction of 0.03 mol% Cd^{2+}, $FA_{0.5}MA_{0.45}Cs_{0.05}Pb_{0.5}Sn_{0.5}I_3$ based solar cells got an efficiency of 20.3% with negligible hysteresis. To prepare efficient low bandgap Sn-Pb mixed perovskite solar cells, Zhao et al. added Cl into the perovskite layer[139]. It was found that the incorporation of 2.5% Cl into the perovskite can enlarge the grain size, increase carrier mobility and suppress charge recombination. Based on planer inverted structure, the champion device got PCE of 18.4%. Later, this group used Br to passivate GB and improve the performance of mixed Sn-Pb solar cells[136]. Conductive atomic force microscopy (c-AFM) indicated that dark saturation current was mainly caused by leakage current from GBs and Br incorporation can passivate GBs to reduce carrier recombination (Figure 2.15f). With the incorporation of 6% Br, the champion device got PCE of 19.03% with good reproducibility. Their work suggests that halide mixing in iodide-based perovskites could be a useful way to improve the performance of mixed Sn-Pb PSCs.

Chapter 3 Enhanced performance of planar perovskite solar cells induced by Van der Waals epitaxial growth of mixed perovskite films on WS_2 flakes

3.1 Introduction

Organic-inorganic metal halide perovskites have received great attention for many advantages, including long carrier diffusion length, high charge mobility, high light absorption coefficient and solution processability[1, 140, 141]. Perovskite solar cells (PSCs) that can convert sunlight directly into electricity have achieved certified power conversion efficiency (PCE) of more than 25%, which is comparable with silicon-based photovoltaic technologies[2]. Compositional engineering with mixed cations and metal halides is an effective approach to optimizing the optoelectronic properties as well as the stability of perovskites. For example, PSCs based on mixed-cation formamidinium (FA)/methylammonium (MA) perovskites demonstrate not only higher efficiency but also improved long term stability in comparison with single cation counterparts[142-144]. Moreover, the film quality of perovskites such as the grain size and orientation can greatly influence their optoelectronic properties, like carrier lifetime and mobility, and hence the performance of resultant PSCs[145-147]. Some strategies have been developed to control the growth of perovskite films. For example, Cho et al. reported that $MAPbI_3$ perovskite films with preferred orientation could be obtained by using thermal-gradient-assisted directional crystallization method[148]. Xu et al. reported a preferable growth of mixed MA/FA perovskites along (001) direction by finely tuning the perovskite compositions[149]. However, it is still challenging to obtain high quality and oriented perovskite films by a solution process.

Epitaxial growth has been demonstrated to be an effective technique for preparing high-quality semiconductor films with preferred orientations[150, 151]. Epitaxial growth of perovskite films have been studied by several groups. For example, Wang et al.

used vapor-phase epitaxy to prepare $CsPbBr_3$ single-crystal thin films on zinc blende (ZnSe) crystals[152]. Benefiting from the good lattice match, orthorhombic $CsPbBr_3$ films with the (110) plane parallel to ZnSe (100) substrate were obtained. Shi et al. reported high-temperature vapor phase epitaxy growth of inorganic $CsPbBr_3$ and $CsSnBr_3$ perovskites on NaCl substrates under a controllable deposition rate[153]. The as-grown epitaxial perovskite films could have a lateral dimension up to centimeters along with superior carrier dynamics. However, for PSCs, the epitaxial growth of perovskite films should be realized on semiconductor interfacial layers.

2D materials like graphene and transition metal dichalcogenides (TMD) have exceptional optoelectronic properties, which have been used as interfacial layers in PSCs to enhance the device performance and stability[154]. For example, the modification of SnO_2 with naphthalene diimidegraphene can enhance charge extraction and transport, resulting in improved PCE[155]. In this chapter, we use liquid-phase-exfoliated WS_2 flakes as an interfacial layer in mixed PSCs. WS_2 has a high carrier mobility and a suitable band structure, making it an excellent charge transport material in PSCs[30, 156]. We find that the mixed perovskite $Cs_{0.05}MA_{0.05}FA_{0.9}PbI_{2.7}Br_{0.3}$ can have van der Waals (vdWs) epitaxial growth along (001) on the WS_2 flakes by spin coating[157, 158], which leads to perovskite films with high crystallinity and low defect density. Meanwhile, the WS_2 interlayer can enhance charge extraction at the interface and suppress interfacial charge recombination in PSCs. Inverted PSCs with a WS_2 interlayer in a planar device structure show PCEs up to 21.1% and excellent long-term stability.

3.2 Devices Fabrication and Characterization

Materials: Formdmidinium iodide (FAI) and methylammonium bromide (MABr) were purchased from Dyesol. Lead iodide (PbI_2) and lead bromide ($PbBr_2$) were purchased from Alpha Aesar. N-methyl-2-pyrrolidone (NMP), diethyl ether, poly[bis(4-phenyl)(2,4,6-trimethylpheny)amine] (PTAA) and bathocuproine (BCP) were purchased from Sigma-Aldrich. Phenyl-C71-butyric acid methyl ester (PCBM) was purchased from Nano-C.

Synthesis of WS_2 flakes: 50 mg of WS_2 powder in 10 mL isopropanol was sonicated

for 6 h. Then the dispersion was centrifuged for 10 min at 2000 rpm to separate the unexfoliated material and the upper solution was collected for further characterization.

Device fabrication: ITO glass substrates were ultrasonically cleaned by deionized water, acetone and isopropanol for 15 min sequentially. PTAA (2 mg mL^{-1} in toluene) was spin-coated on the ITO substrates at 4000 rpm for 30s then annealed at 100 ℃ for 10 min. For the WS_2 modification, the WS_2 flakes in isopropanol were spin-coated on the PTAA film for several times to achieve the desired coverage. 1.4 M $Cs_{0.05}MA_{0.05}FA_{0.9}PbI_{2.7}Br_{0.3}$ perovskite precursor solution with molar ratio of CsI:MABr:FAI=0.05:0.05:0.9 and the molar ratio of (FAI+MABr+CsI):($PbBr_2$+PbI_2)=1in mixed DMF/NMP (6:1) solution was spin-coated on the substrates at 4000 rpm for 30s and diethyl ether was dripped at 10^{th} s. The as-spun perovskite films were annealed at 75 ℃ for 1 min and 100 ℃ for 60 min. Afterwards, PCBM (20 mg mL^{-1} in chlorobenzene) was spin-coated at 3000 rpm for 30s to act as electron transport layer. BCP (0.5 mg mL^{-1} in methanol) was spin-coated on the PCBM at 5000 rpm for 30s. The devices were completed by thermal evaporation of Ag on the BCP layer.

Characterizations: Photocurrent density-voltage (J-V) curves were measured by a Keithley 2400 source meter with a solar simulator under AM 1.5 G one sun illumination (Newport 66902). The external quantum efficiency (EQE) of the PSCs was measured using an EQE system under DC mode. SEM images were obtained by a field-emission SEM (Hitachi S-4300). The TEM images were collected using JEOL JEM 2100F operated at 200 kV. XRD measurements were collected using Cu Kα radiation (Rigaku, Smartlab). XPS were measured on Thermo Fisher Scientific XPS system.

3.3 Results and Discussion

WS_2 flakes were prepared by liquid phase exfoliation of bulk WS_2 powders using ultrasound[159, 160]. Transmission electron microscopy (TEM) and atomic force microscopy (AFM) were used to analyze the microstructure and morphology of the WS_2 flakes. **Figure 3.1**a shows a typical TEM image of WS_2 flakes. The high-resolution TEM (HRTEM) image of a WS_2 flake is shown in Figure 3.1b. The

clear lattice fringes indicate the high quality of the WS_2 flake, and the inset of Figure 3.1b shows the selected-area electron diffraction (SAED) pattern of the WS_2 flake, corresponding to hexagonal crystal structure. From the AFM image of the WS_2 flakes and corresponding thickness statistics in Figure 3.1c, the thickness of the WS_2 flakes is in the 2-5 nm range, confirming the few layer WS_2 flakes. The WS_2 flakes were observed under scanning electron microscopy (SEM) and the sizes of the flakes can be decided from the SEM image shown in Figure 3.1d. The statistics of the flake sizes are shown in Figure 3.1e. The average lateral size is estimated to be ~700nm. The optical absorption spectrum of the WS_2 flakes dispersed in isopropanol is shown in the inset of Figure 3.1f. A Tauc plot is derived from the absorption spectrum and an optical bandgap of WS_2 flakes is estimated to be ~1.76 eV.

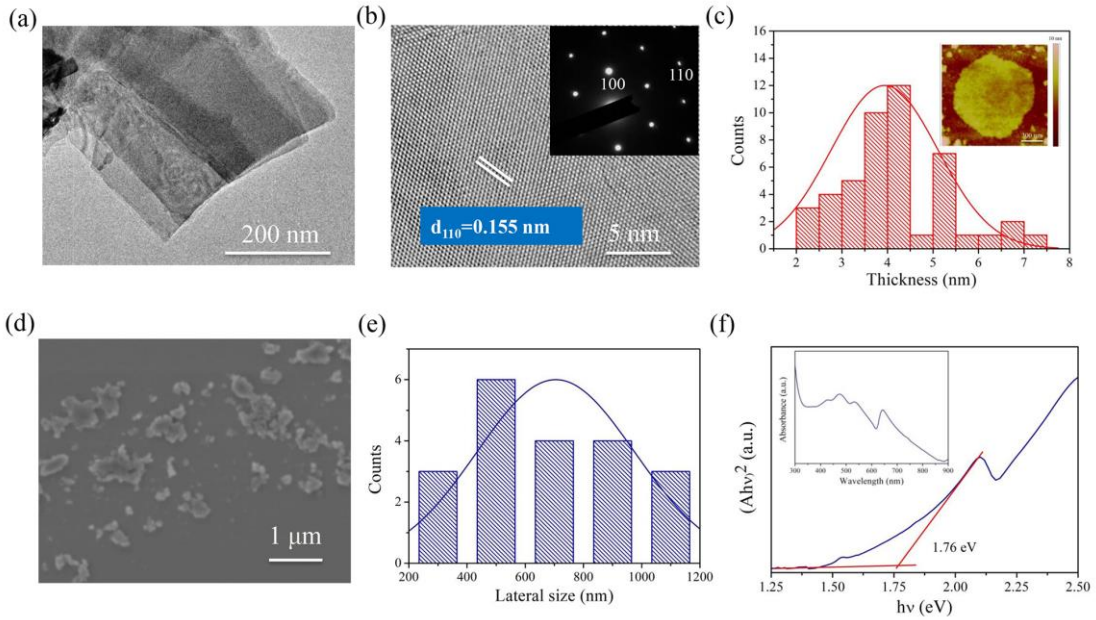

Figure 3.1 TEM image of WS_2 flakes. (b) HRTEM image of WS_2 flake and the inset shows the SAED pattern of WS_2 flake. (c) Film thickness statistics obtained from AFM images of WS_2 flakes. Inset: AFM image of one flake. (d) SEM image of WS_2 flakes. (e) Size distribution statistics of WS_2 flakes obtained from SEM images. (f) Optical absorption spectrum of WS_2 flakes (inset) and calculated optical bandgap of WS_2 flakes from the Tauc plot.

PSCs were fabricated with a planar p-i-n structure of ITO/PTAA/WS_2/perovskite/PCBM/BCP/Ag as shown in **Figure 3.2**a, where WS_2 acts as an interlay to enhance the device performance. The WS_2 layer was prepared by spin coating the WS_2 solution on a PTAA layer with a spin coating speed of 2000 rpm. The

distribution of the WS_2 flakes on the PTAA surface can be observed under SEM as shown in Figure 3.1d. Then a triple cation halide perovskite ($Cs_{0.05}MA_{0.05}FA_{0.9}PbI_{2.7}Br_{0.3}$) was coated on the WS_2/PTAA surface as the active layer[161].

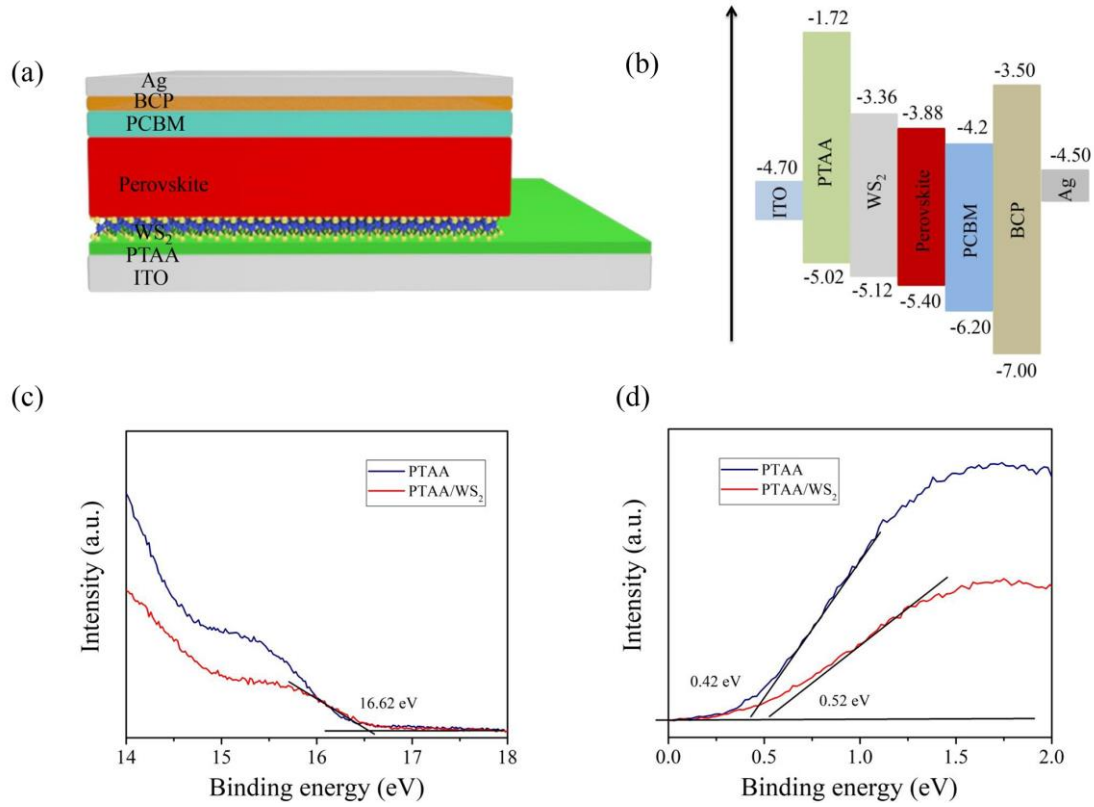

Figure 3.2 (a) Device structure of planar inverted perovskite solar cells. (b) Energy band alignment of the solar cells with WS_2 interlayer. (c) The cut-off energy and (d) Fermi edge of UPS spectra for plain PTAA and WS_2 modified PTAA.

Ultraviolet photoelectron spectroscopy (UPS) was used to investigate the band structure of the PTAA films before and after WS_2 modification. As shown in **Figure 3.2**c,d, the valence band (VB) level of WS_2 flakes could be obtained from the equation of $E_{VB}=21.22-(E_{cut\text{-}off}-E_{F,edge})$, which is calculated to be −5.12 eV. Then, the conduction band (CB) level of WS_2 is estimated to be -3.36 eV, according to the equation of $E_{CB}=E_{VB}+E_g$. The corresponding energy diagram of the device is shown in Figure 3.2b[161, 162]. The crystal structures of WS_2 and perovskite are depicted in **Figure 3.3**a. Notably, the plane distance of (110) in WS_2 crystal is half of that of the (020) plane of the perovskite layer, which may enable WS_2 flake as an epitaxial growth template for perovskite grains (Figure 3.3b). WS_2 has a dangling bond-free

surface that can lead to Van der Waals (vdWs) epitaxial growth of a perovskite film even with lattice or symmetry mismatch between them[163, 164].

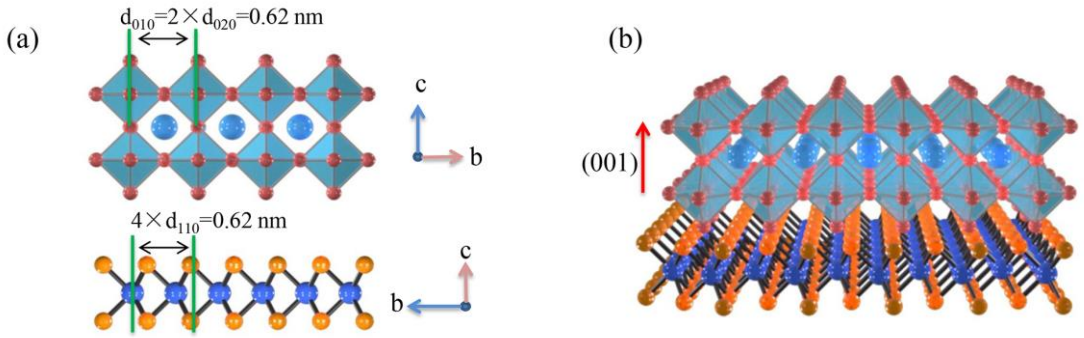

Figure 3.3 (a) Side view of crystal structure and lattice constant of perovskite and WS_2. (b) Schematic illustration of the epitaxial growth of perovskite film on the WS_2 substrate.

Perovskite films prepared on WS_2 or PTAA surfaces by spin coating were first characterized by X-ray diffraction (XRD) measurements. **Figure 3.4**a shows the XRD patterns of perovskite films on PTAA or WS_2/PTAA substrates. All the diffraction peaks could be assigned to cubic perovskite phase and no yellow phase was observed, confirming the phase purity of the perovskite films. Since the film thickness and the characterization conditions are identical, the much increased XRD peak intensity for the film with WS_2 indicates enhanced perovskite crystallization induced by WS_2 flakes. Moreover, the peak intensity ratio of (001)/(111) increases significantly after the introduction of WS_2, indicating the preferable growth along (001) plane of the mixed perovskite after WS_2 modification.

To confirm the vdWs epitaxial growth of the mixed perovskite on WS_2, the microstructure of perovskite/WS_2 heterojunction and perovskite film were then characterized under TEM. The TEM sample was prepared by directly spin-coating the perovskite film on the WS_2 flakes loaded on TEM grid[165]. Figure 3.4b shows the TEM image of perovskite/WS_2 heterojunction and the WS_2 flake was partially covered by a perovskite grain. As shown in Figure 3.4c, the HRTEM image with clear lattice planes indicates high crystalline of perovskite. The plane with lattice distance of 0.31 nm is indexed to (020) plane of the perovskite[166, 167]. The inset of Figure 3.4c shows the SAED pattern of the perovskite, which is consistent with cubic structure of the mixed perovskite. It is notable that the lattice distance of the (020) plane for the

mixed perovskite is 0.31 nm[168], which is twice of the plane distance of (110) of WS_2[169]. This lattice match would favor the epitaxial growth of the mixed perovskite on WS_2 flakes.

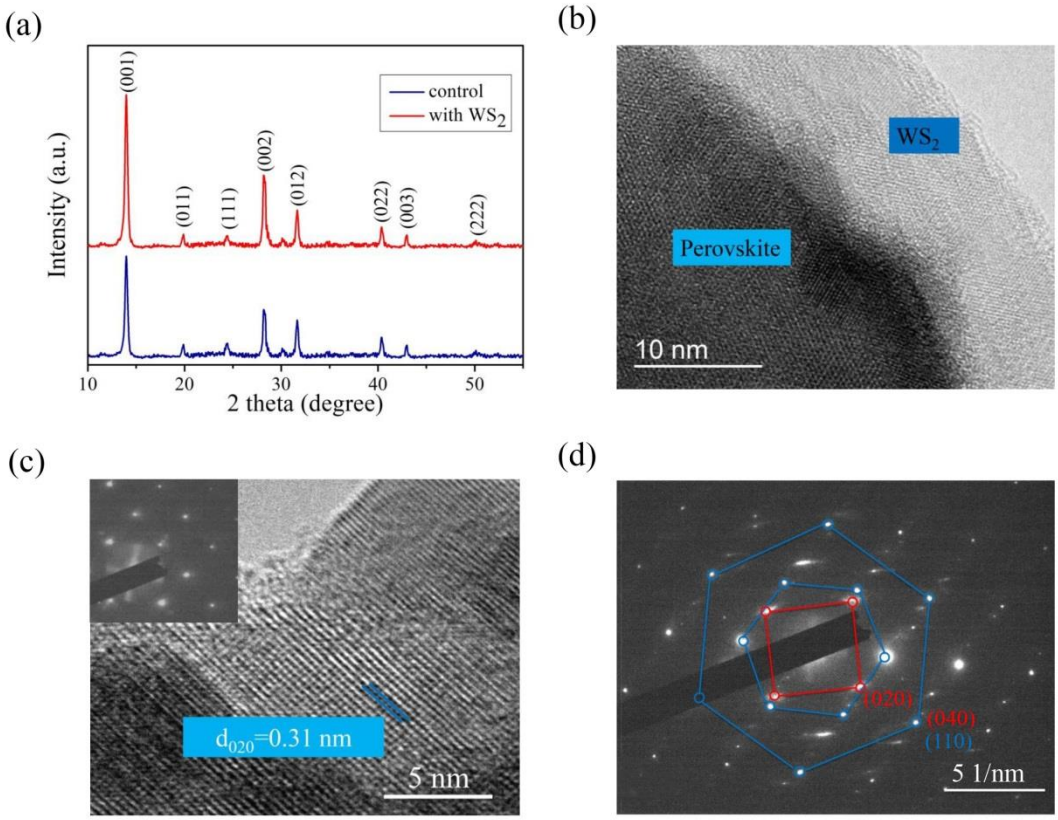

Figure 3.4 (a) XRD patterns of perovskite films fabricated on PTAA and WS_2 modified PTAA film. (b) TEM image of perovskite/WS_2 heterojunction. (c) HRTEM image of perovskite and the inset shows the SAED pattern of perovskite. (d) The SAED pattern of perovskite/WS_2 heterojunction. The blue diffraction spot is for WS_2 and the red one is for perovskite.

As shown in Figure 3.4d, the SAED pattern of perovskite/WS_2 heterojunction shows two sets of diffraction patterns, which can be assigned to the bottom WS_2 (blue) and the top perovskite (red), respectively. The correlation between the two sets of crystal lattices clearly indicates the epitaxial growth of perovskite on the WS_2 flake.

Moreover, the energy dispersive spectroscopy (EDS) mapping clearly demonstrates the loading of Pb, I, Br elements on the WS_2 flakes (**Figure 3.5**). Apart from the lattice match between perovskite (020) and WS_2 (110), the dangling-bond-free surface of WS_2 flake is also favorable for the vdWs epitaxial growth of the perovskite layer[151, 170], leading to the preferable growth of mixed perovskite with (001) plane

parallel to the WS_2 substrate.

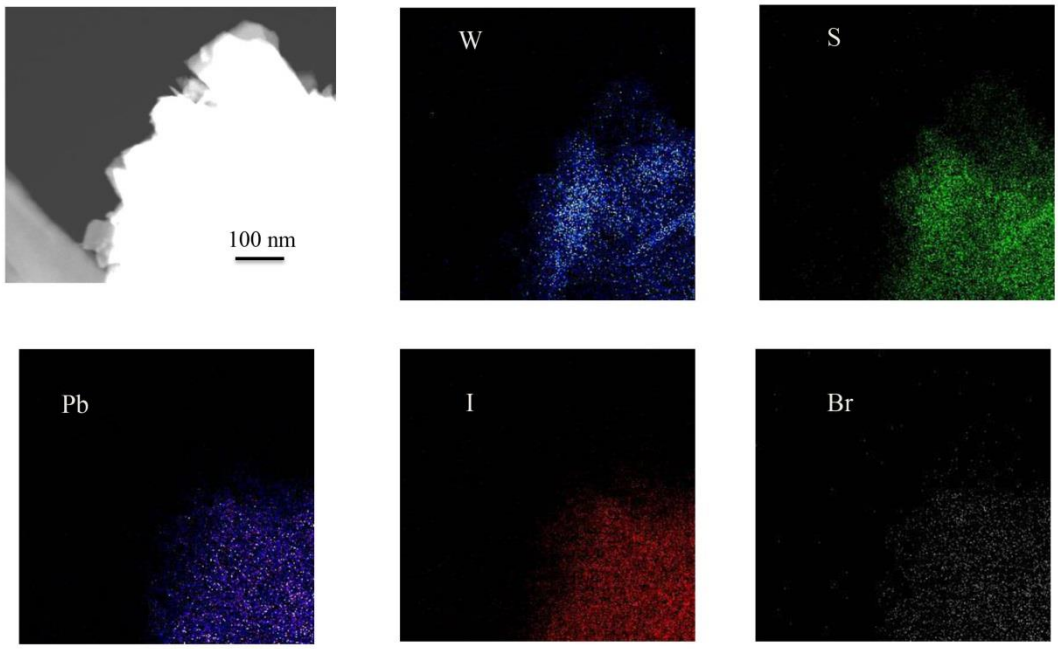

Figure 3.5 TEM image of WS_2/perovskite heterojunction and corresponding EDS mapping of the region.

SEM images of perovskite films deposited on plain PTAA and WS_2/PTAA are shown in **Figure 3.6**a,b. It can be found that the introduction of WS_2 flakes can increase the average grain size of perovskite films, which is favorable for the performance of PSCs.

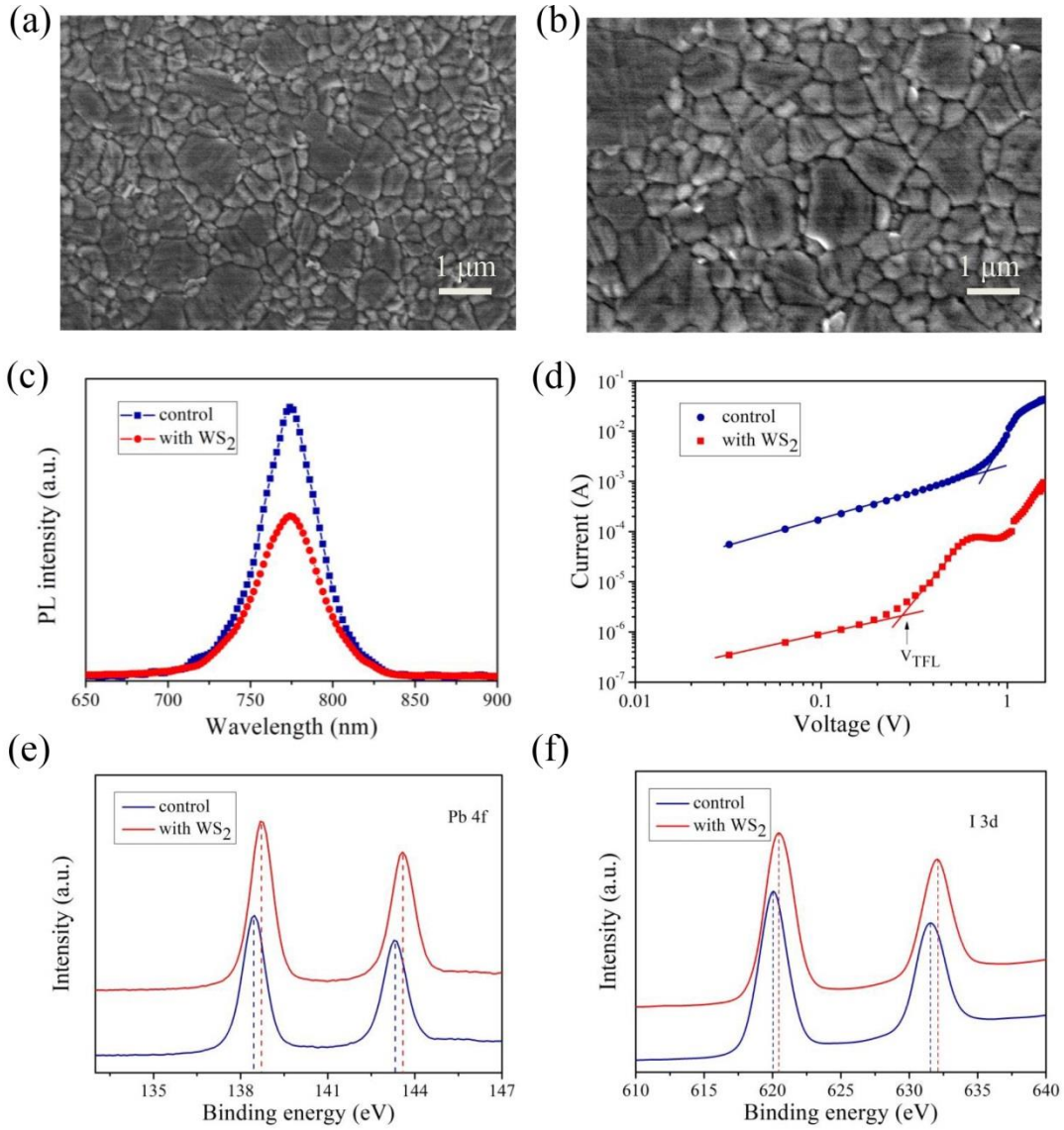

Figure 3.6 SEM images of perovskite films deposited on (a) PTAA and (b) WS_2/PTAA films. (c) Stead state PL spectra of perovskite films prepared on different substrates. (d) Dark I-V curves of hole-only device with and without WS_2 layer, the device structure is ITO/PTAA(or PTAA/WS_2)/perovskite/Au. XPS spectra of (e) Pb 4f and (f) I 3d for perovskite and perovskite/WS_2 mixed films.

To get more information of WS_2 modification on perovskite film quality and charge transfer process, steady state photoluminescence (PL) was measured. As shown in Figure 3.6c, the PL intensity of the perovskite film deposited on WS_2/PTAA is much lower than that of a perovskite film on PTAA, indicating enhanced charge transfer induced by WS_2 flakes. Because of the well-aligned energy level and high charge mobility of WS_2 flakes, the fast charge transfer can suppress interfacial charge

recombination.

To evaluate the charge transport properties of the devices, dark current density was measure and shown in **Figure 3.7**. It can be found that the solar cells with WS_2 interlayer has a lower leakage current than that of the control one, indicating the decreased carrier generation rate and background carrier density in the device. Because the carrier generation rate in a solar cell is related to the trap density in the device[136, 171, 172], this result indicates that the introduction of WS_2 can decrease the trap density in the devices.

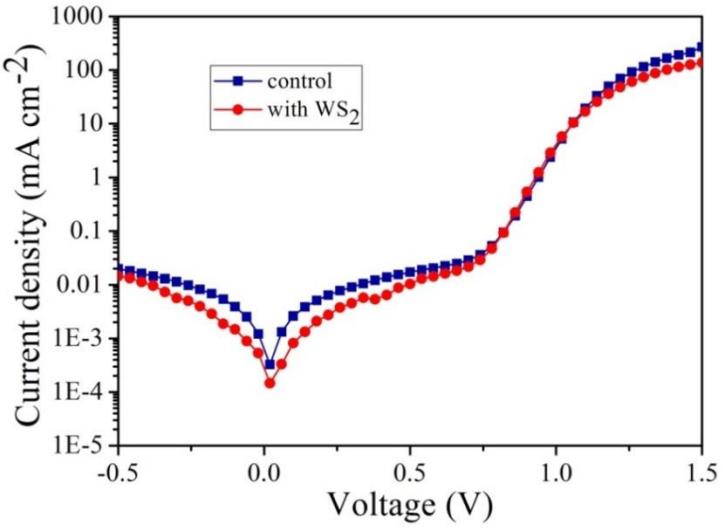

Figure 3.7 Dark current of the PSCs based on different HTLs.

To quantitatively evaluate the defect density of perovskite films, hole-only devices with a structure of ITO/PTAA/WS_2/perovskite/Au were prepared to measure dark I-V curves. As shown in Figure 3.6d**,** the I-V curves can be divided into three regions. At low bias voltages, current and bias voltage has a linear relation, corresponding to the Ohmic region. At intermediate bias region, the current density quickly increases after the kink point, which is called trap-filled limited region. The third region at high bias is space-charge-limited region[173]. The trap density can be calculated by trap-filled limit voltage (V_{TFL}) with the equation of $n_t=(2\varepsilon\varepsilon_0 V_{TFL})/(qL^2)$, where ε is the dielectric constants of perovskite, ε_0 is the vacuum permittivity, q is the elementary charge and L is the thickness of perovskite layer[174]. V_{TFL} could be obtained by fitting the I-V curves. The defect densities of the perovskite films are estimated to be 1.94×10^{15}

cm^{-3} and 0.68×10^{15} cm^{-3} for the devices without and with the WS_2 interlayer, respectively. The much lower defect density induced by WS_2 could be attributed to the enhanced crystallinity of the perovskite film, which is favorable for the device performance.

X-ray photoelectron spectroscopy (XPS) was measured to unravel the interaction between the WS_2 flakes and perovskite layer. Figure 3.6e,f show the XPS of Pb 4f and I 3d of perovskite and WS_2/perovskite mixture, and the binding energies (BEs) of perovskite/WS_2 mixture shows an obvious shift compared with that of the plain perovskite. The clear shift of BEs indicates the modified chemical environmental of $[PbI_6]^{4-}$ octahedral and the strong S ··I interaction[175, 176]. This interaction should exist at the perovskite/WS_2 interface, which could facilitate the growth of perovskite with larger grain size and favor rapid charge extraction to suppress interfacial charge recombination.

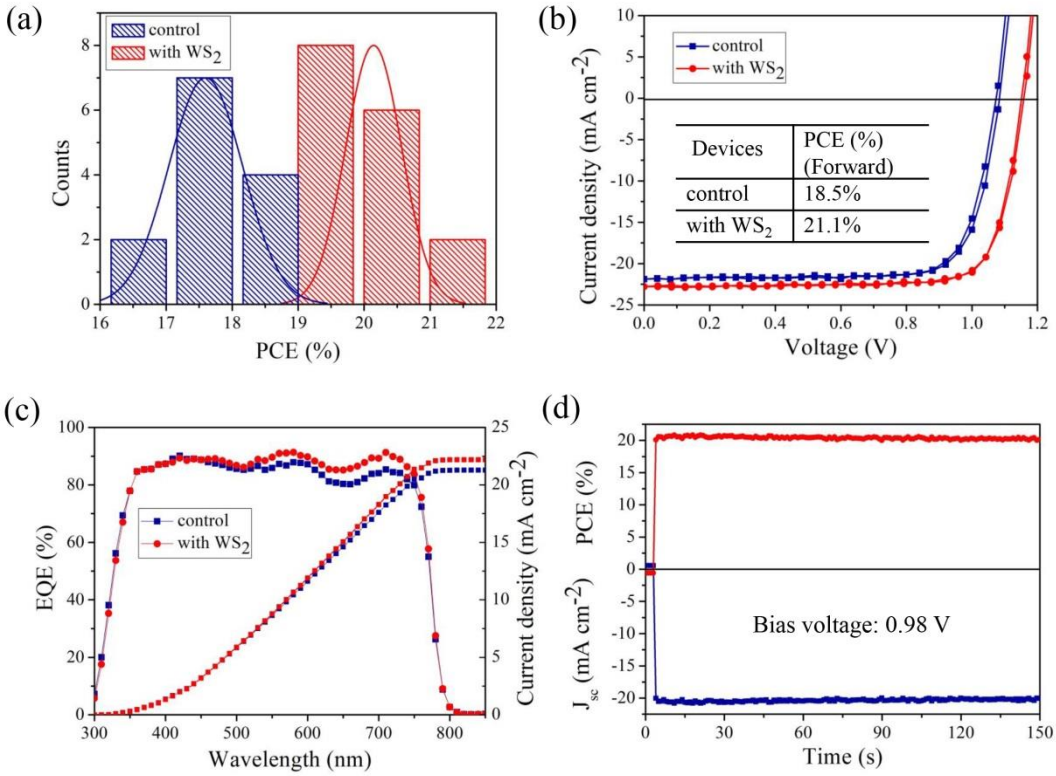

Figure 3.8 (a) PCE statistics of PSCs based PTAA and WS_2 modified PTAA. (b) J-V curves and (c) EQE of the champion devices with different HTLs. (d) Stabilized PCE and photocurrent density of the champion WS_2 based device.

Planar inverted PSCs with or without WS_2 flakes were prepared to investigate the

effect of the WS_2 interlayer on their photovoltaic performance. **Figure 3.8**a shows statistic photovoltaic performance, which demonstrates the good reproducibility of the data. J-V curves of the best-performing devices are shown in Figure 3.8b. The control device has a PCE of 18.5% with an open voltage (V_{OC}) of 1.08 V, a current density (J_{SC}) of 21.88 mA cm^{-2} and a fill factor (FF) of 78.4% under forward scan. With the introduction of a WS_2 interlayer, the champion device exhibits a PCE of 21.1% with a V_{OC} of 1.15V, a J_{SC} of 22.75 mA cm^{-2} and a FF of 80.6%. The integrated J_{SC} values from the external quantum efficiency (EQE) data are close to those from J-V curves as shown in Figure 3.8c.

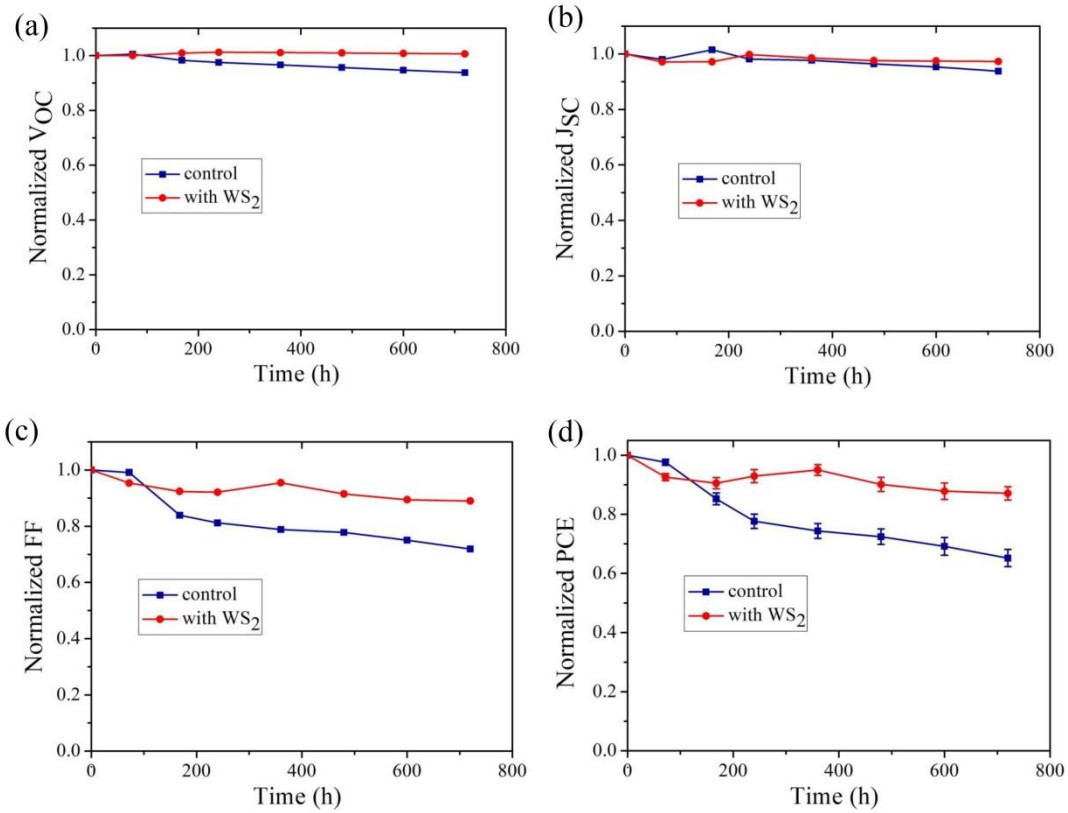

Figure 3.9 Stability test of (a) V_{OC}, (b) J_{SC}, (c) FF and (d) PCE of the PSCs based on different HTLs (without encapsulation, store in ambient air with ~30% humidity).

The enhanced device performance could be attributed to the improved quality of the perovskite film and efficient charge extraction induced by the WS_2 interlayer. Notably, the much improved FF could be ascribed to the decreased interfacial series resistance and reduced charge loss after the WS_2 modification[38, 177]. Moreover, the WS_2 modified device showed a stabilized PCE of 20.5% as shown in Figure 3.8d, which was in agreement with the J-V scans.

Long term stability of the unencapsulated devices stored in the ambient condition was recorded and shown in **Figure 3.9**. The WS_2 modified device remains more than 90% of its initial PCE after 1 month, while the control device retains only about 70% of its initial PCE. The enhanced device stability could be ascribed to the enhanced perovskite film quality and reduced interface defects[178].

3.4 Summary

In summary, WS_2 flakes were introduced as growth templates for the vdWs epitaxial growth of mixed perovskite films, leading to perovskite grains with enlarged sizes and a preferred orientation along (001). Moreover, perfect perovskite/WS_2 interface and the S···I interaction in it can facilitate efficient charge extraction and reduce interfacial carrier recombination. Resultantly, PSCs with a WS_2 interlayer show a PCE up to 21.1% and excellent device stability. This work opens a window of utilizing high-mobility and defect-free 2D materials like WS_2 as interfacial layers in PSCs to improve the device performance. In addition, the successful vdWs epitaxial growth of mixed perovskites on WS_2 may find important applications in other perovskite optoelectronic devices.

Chapter 4 Enhanced performance of tin-based perovskite solar cells induced by ammonium hypophosphite additive

4.1 Introduction

Organic-inorganic hybrid halide perovskite solar cells (PSCs) have been considered as the most promising candidate for the new generation photovoltaic technology because of their high power conversion efficiency (PCE), low cost and convenient fabrication processes[1, 140, 179, 180].The state-of-the-art lead-based halide perovskites exhibit excellent optoelectronic properties, like strong light absorption, long carrier diffusion length and low density of defects[9, 181-183], leading to the record PCE over 25%[2]. However, the toxic lead may cause environmental problems when PSCs are widely used. Thus, it is imperative to develop lead-free perovskites with favorable physical properties. Among various alternative metal elements (Sn, Bi, and Sb) for replacing Pb in perovskites[51, 184, 185], Sn may have the highest potential because of the ideal optical and electrical properties of tin-based perovskites for photovoltaic applications[186]. However, the device performance of tin-based PSCs still falls behind that of lead-based counterparts due to the following reasons. First, the major problem of tin-based perovskite is the poor stability because of the formation of Sn vacancies and the oxidation of Sn^{2+} to Sn^{4+}, leading to high doping levels and recombination rates in perovskite films. Second, it is difficult to get uniform and pinhole-free tin-based perovskite films due to the fast crystallization of the films[103]. So reported tin-based PSCs suffer from low efficiency and poor stability especially in air[86].

Tin-based PSCs have been studied by many groups and various approaches based on different principles have been developed to improve the device performance. To suppress the oxidation of Sn^{2+} and reduce the doping levels, SnF_2 or $SnCl_2$ has been incorporated into perovskite precursor solutions[68, 187]. However, an excess of SnF_2/$SnCl_2$ may cause phase separation in perovskite films (e.g. inhomogeneous

dispersion) and deteriorate the device performance[188]. To further suppress the oxidation process, Kanatzidis and co-workers prepared the perovskite films under a reducing vapor atmosphere[86]. Moreover, solvent engineering[103, 104] and compositional engineering with mixed cations[189, 190] have been developed to prepare high-quality tin-based perovskite films. Very recently, tin-based perovskite film with hierarchy structure was designed to enhance oxidation resistance for improved device stability and performance[191]. However, the photovoltaic performance and stability of the tin-based PSCs still lags far behind those of lead-based PSCs. So, it is necessary to develop novel techniques that can not only retard the Sn^{2+} oxidation but also assist the preparation of compact and uniform perovskite films.

In this chapter, we introduced ammonium hypophosphite (AHP, $NH_4H_2PO_2$) additive in $FASnI_3$ perovskite precursor solutions. AHP is a reducing agent that can prohibit the oxidation of Sn^{2+} in perovskites[61, 85]. Meantime, $H_2PO_2^-$ can form intermediate phase with $SnCl_2$ and lead to improved film morphology and lower trap densities. In addition, we use CuSCN as a hole transporting material in the devices because of its high hole mobility and good energy alignment with $FASnI_3$. The devices show the PCE up to 7.3% with a short circuit current (J_{SC}) of 19.39 mA cm^{-2}, open circuit voltage (V_{OC}) of 0.55 V and fill factor (FF) of 68.8%. More importantly, the devices exhibit good long-term stability in ambient atmosphere. This work clearly indicates that the introduction of proper antioxidant agent in precursor solutions can boost the device performance and long-term stability of tin-based PSCs.

4.2 Devices Fabrication and Characterization

Materials: All chemicals were used as received without any further purification. Copper (I) thiocyanate (CuSCN, 99%) and $SnCl_2$ (>99%) were purchased from Sigma-Aldrich. $CH(NH_2)_2I$ was purchased from Dyesol Ltd. SnI_2 (99.999%) and phenyl-C71-butyric acid methyl ester (PCBM) were purchased from Alfa Aesar and Nano-C, respectively.

Device fabrication: The ITO-coated glass substrates were cleaned via ultrasonication in deionized water, acetone and isopropanol for 10 min, respectively. The process of preparing CuSCN on ITO was similar with

previous report[192]. CuSCN dissolved in aqueous ammonia (10 mg mL^{-1}) was spin-coated on the ITO substrate at 4000 rpm for 20 s in ambient air and then the films were annealed at 150℃ for 20 min on hotplate in air. Then the films were transferred to a nitrogen-purged glovebox for later experiment. The $FASnI_3$ perovskite precursor solution was prepared by dissolving 1 mmol SnI_2 and 1 mmol FAI with 10 mol% $SnCl_2$ in 1 mL mixed solvent (DMF:DMSO=4:1). For the AHP included perovskite precursor solution, the molar ratio of AHP and SnI_2 was 3%, 5% and 7%, respectively. The perovskite precursor solution was spin-coated on the CuSCN layer at 2000 rpm for 5 s then 5000 rpm for 30 s, and 100 μl chlorobenzene was dripped onto the perovskite film at the 11^{th} s. The obtained films were annealed at 70 ℃ for 10 min. PCBM (20 mg mL^{-1} in chlorobenzene) was spin-coated on the perovskite film at 1500 rpm for 30 s to function as electron transporting layer. Finally, 90 nm silver electrodes were thermal evaporation on the PCBM layer under vacuum to complete the device fabrication. An active area of 0.048 cm^2 was defined by shadow mask.

Characterization: The morphology of the films was recorded by field-emission scanning electron microscope (Hitachi S-4300). The optical absorption spectra of perovskite films were measured by Shimadzu UV-2550 spectrophotometer. XRD patterns were measured by Rigaku SmartLab X-ray diffractometer using Cu Kα radiation. The time-resolved photoluminescence (PL) spectra were obtained at 850 nm with the excitation at 650 nm by an FLS980 fluorescence spectrometer (Edinburgh Instruments, England).

The current-voltage (J-V) curves of the solar cells were measured by Keithley 2400 digital source meter under simulated air mass 1.5 G sunlight (Newport 91160, 300 W). The light intensity was calibrated by a standard monocrystalline silicon photodiode. EQE spectra were recorded by an Oriel integrated system. The Nyquist plots were recorded by a Zennium X electrochemical workstation (Zahner, Germany). All the PSCs were measured in ambient air at room temperature without encapsulation. For the stability test,

samples were stored in ambient condition (~20% relative humidity) after measurements.

4.3 Results and Discussion

AHP was introduced into $FASnI_3$ precursors as a reducing additive. To assess the reducing ability of AHP, a plain $FASnI_3$ precursor solution was prepared and exposed to ambient air. At the beginning, the precursor solution showed a clear yellow color (**Figure 4.1**a). After being exposed to air for 15 minutes, the solution turned to be dark red, indicating the oxidation of Sn^{2+} to Sn^{4+}.[92] Interestingly, with the introduction of AHP (12 mol%) into the precursor solution, the color of the solution gradually changed to yellow again for the following reaction[193]:

$$Sn^{4+} + 3H_2PO_2^- \rightarrow Sn^{2+} + 2HPO_3^{2-} + PH_4^+$$

This result clearly indicates the reducing ability of AHP and its effect on Sn ions in the perovskite precursor.

Due to the higher Lewis acidity of Sn than that of Pb, the crystallization of Sn-based perovskite is much faster than its lead analogue, making it difficult to obtain homogeneous and compact perovskite films[194]. To evaluate the influence of AHP on the perovskite film morphology, $FASnI_3$ perovskite films prepared with various amounts of AHP were characterized under scanning electron microscopy (SEM). Many pinholes can be observed from the plain $FASnI_3$ films (Figure 4.1b) because of the fast and uncontrollable crystallization. Moreover, some needle-like aggregates formed on the film resulting from phase separation of $SnCl_2$. With the introduction of 3 mol% AHP, phase separation almost disappeared while some pinholes still existed on the film (Figure 4.1c). Notably, the inclusion of 5 mol% AHP in the precursor solution resulted in a pinhole-free and compact perovskite film (Figure 4.1d), which is beneficial for device performance. However, when the amount of AHP was increased to 7 mol%, the perovskite film became much rougher and many pinholes could be found in the film (Figure 4.1e).

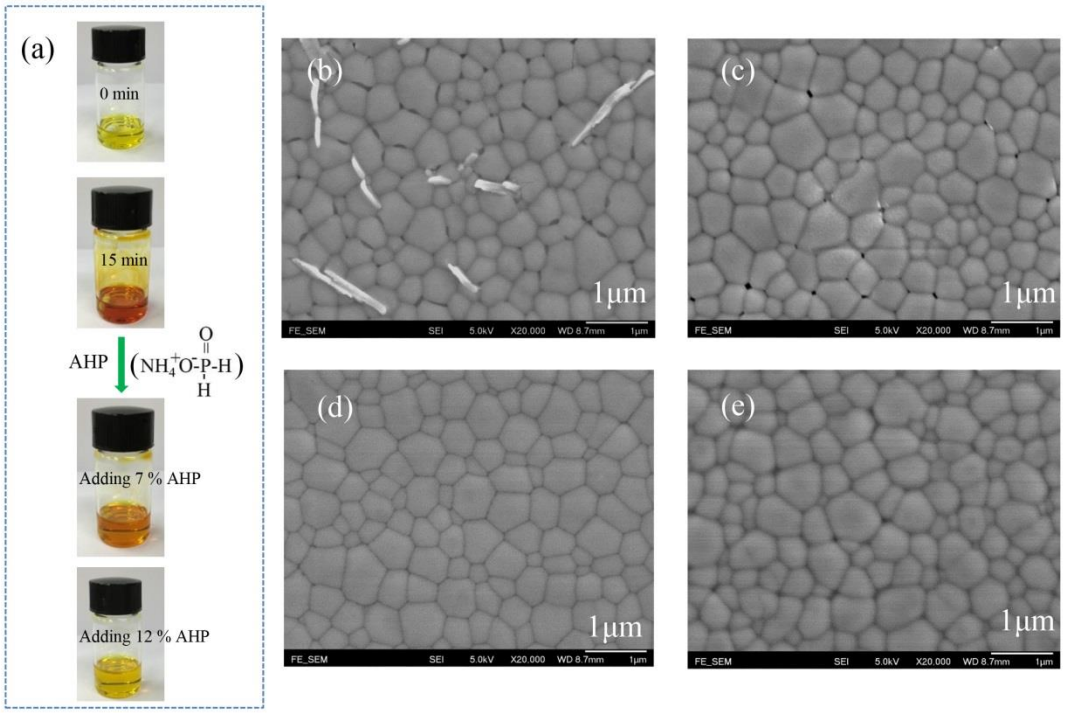

Figure 4.1 Photographs of $FASnI_3$ precursor solution and molecular structure of AHP. SEM images of $FASnI_3$ films prepared with various amounts of AHP, (b) plain $FASnI_3$, (c) 3 mol% AHP, (d) 5 mol% AHP and (e) 7 mol% AHP-added $FASnI_3$.

We consider that the AHP additive in the perovskite precursor can mix with $SnCl_2$ and form a complex to encapsulate perovskite grains. Notably, P=O bond in AHP can coordinate with $SnCl_2$ and induce a uniform dispersion of AHP-$SnCl_2$ intermediate complex in the perovskite film and prohibit the phase separation of $SnCl_2$.[195]

To confirm the interaction between AHP and $SnCl_2$, a pure AHP film and an AHP-$SnCl_2$ (molar ratio, 1:1) composite film were characterized using Fourier transform infrared spectroscopy (FTIR). As shown in **Figure 4.2**a, the vibration of P=O bond was shifted to an obviously lower wavenumber in the AHP-$SnCl_2$ composite, which validates the strong interaction between AHP and $SnCl_2$. Meanwhile, NH_4^+ can also form intermediate phases during perovskite film preparation[196, 197]. Thus, these intermediate phases can suppress the crystallization of $SnCl_2$ and regulate the nucleation and crystallization of perovskite, resulting in a high-quality $FASnI_3$ film.

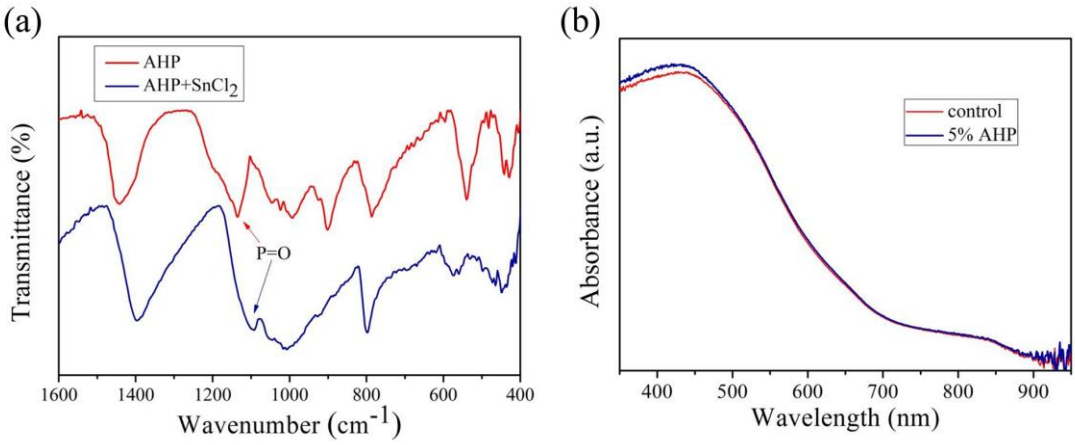

Figure 4.2 (a) FTIR spectra of AHP and AHP-$SnCl_2$ complex. (b) Absorption spectra of control $FASnI_3$ film and 5 mol% AHP included $FASnI_3$ film.

The absorption spectra of $FASnI_3$ films without and with 5 mol% AHP are shown in Figure 4.2b. All the films have similar absorption onset of ~890 nm with an estimated bandgap of 1.39 eV. The X-ray diffraction (XRD) patterns of $FASnI_3$ films prepared with different contents of AHP are shown in **Figure 4.3**. The characteristic peaks of the $FASnI_3$ films without and with AHP all matched well with the orthorhombic lattice structure of $FASnI_3$. Moreover, the much sharper peaks observed from $FASnI_3$ film with 5 mol% AHP demonstrated its enhanced crystallinity.

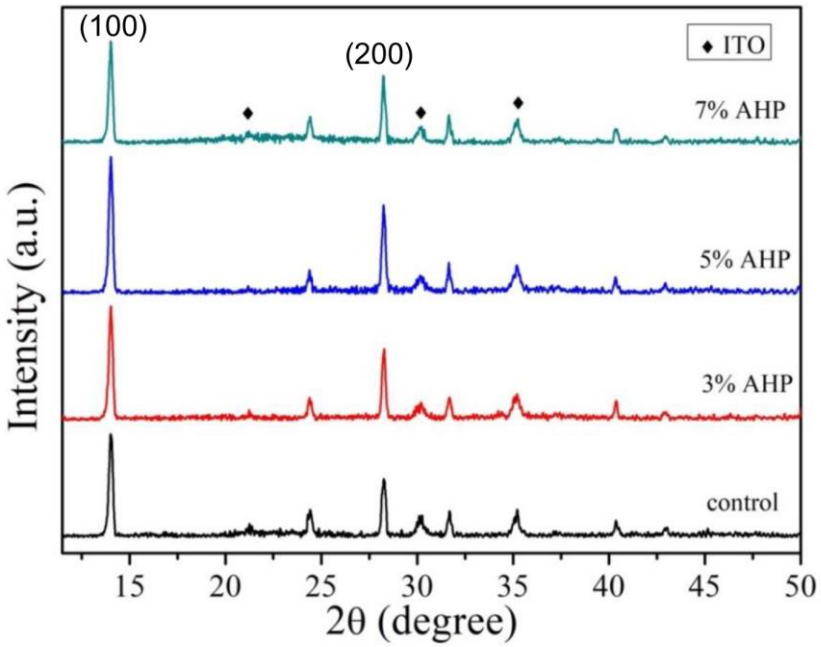

Figure 4.3 XRD pattern of $FASnI_3$ films with various amounts of AHP.

X-ray photoelectron spectroscopy (XPS) measurements were used to detect the location of the AHP-$SnCl_2$ complex. According to **Figure 4.4**a, the content of Cl significantly decreased after argon etching, indicating that Cl was not incorporated into the perovskite lattice. Similar result was found for the P element from the XPS spectra (Figure 4.4b). These elemental composition values confirm that AHP-$SnCl_2$ complex can encapsulate perovskite grains on their surfaces.

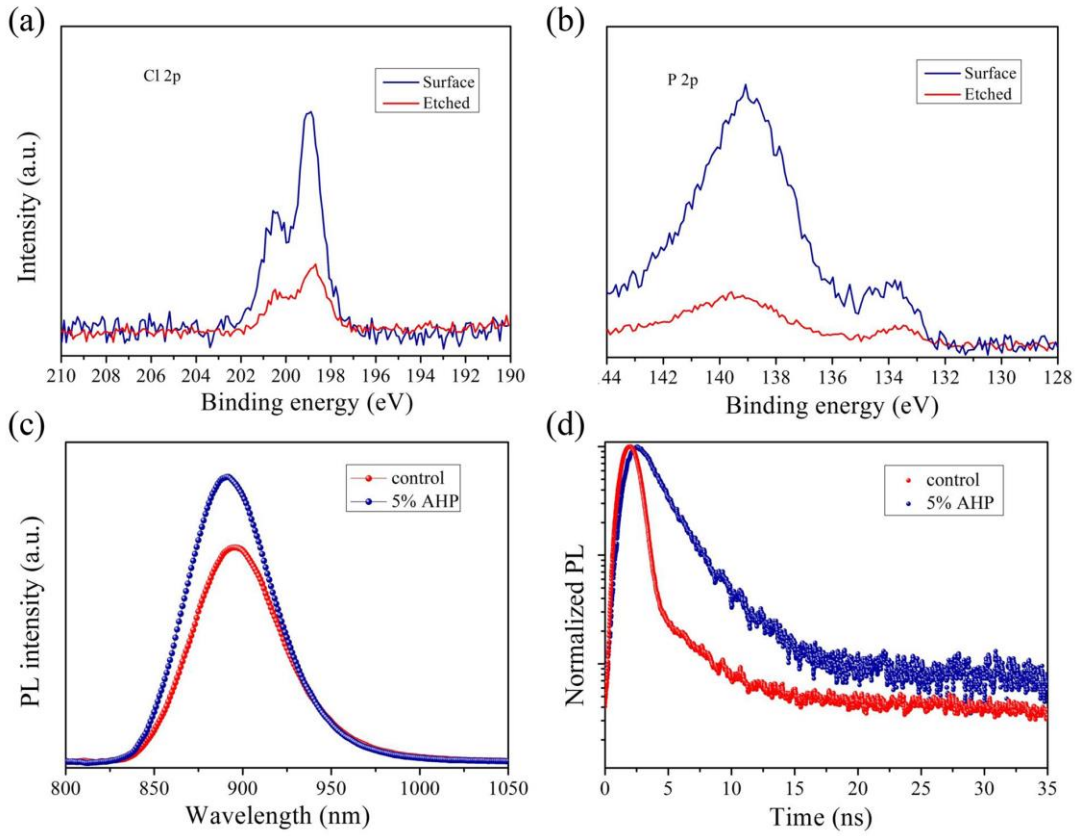

Figure 4.4 XPS spectra of (a) Cl peaks and (b) P peaks of 5 mol% AHP included $FASnI_3$ perovskite film before and after Argon etching. Steady state (c) and time-resolved (d) photoluminescence spectra of plain $FASnI_3$ film and 5 mol% AHP modified $FASnI_3$ film.

To get deeper understanding of charge dynamics, the $FASnI_3$ films were characterized using steady state and time-resolved photoluminescence (PL) spectroscopy. As shown in Figure 4.4c, the plain $FASnI_3$ film showed a PL peak at around 895 nm, corresponding to a bandgap of 1.39 eV. The AHP-modified $FASnI_3$ film had a much stronger PL intensity, indicating suppressed nonradiative recombination, which can be attributed to its improved film quality and reduced defect density[198]. Moreover, the blue shift of the PL peak observed in the AHP-modified

$FASnI_3$ film also implied the improved crystallinity of the perovskite film. The time-resolved PL spectra are shown in Figure 4.4d, which are fitted by a bi-exponential decay model[170]. The average lifetimes for the plain $FASnI_3$ film and AHP-modified $FASnI_3$ film are 0.81 ns and 2.18 ns, respectively, which further confirms the smaller trap density and reduced charge recombination induced by AHP[199, 200]. The increased carrier lifetime is favorable for the open circuit voltage of resultant PSCs[201].

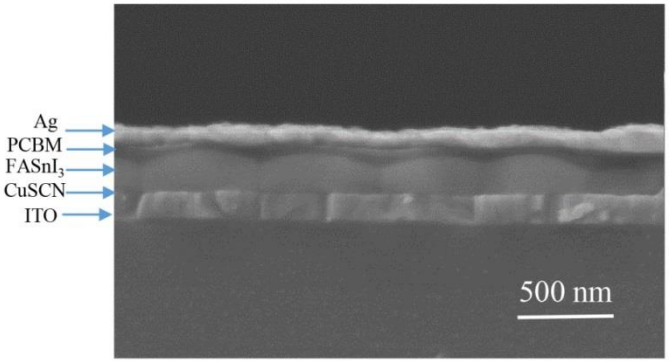

Figure 4.5 Cross-sectional SEM image of the $FASnI_3$ solar cells.

Inverted PSCs with the planar device structure of ITO/CuSCN/$FASnI_3$/PCBM/Ag were prepared to evaluate the effect of AHP additive on the photovoltaic performance (**Figure 4.5**), and the corresponding energy diagram is shown in **Figure 4.6**a[165, 202].

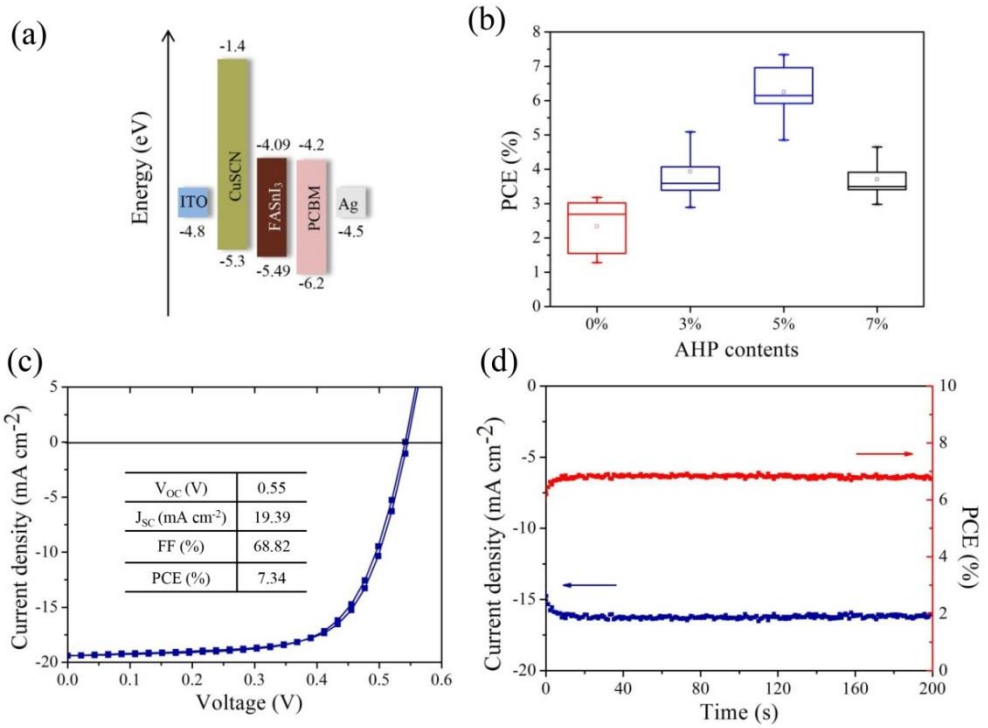

Figure 4.6 (a) Schematic energy diagram of the $FASnI_3$ solar cells. (b) The PCE distribution of $FASnI_3$ solar cells prepared with various contents of AHP. (c) Current density-voltage (J-V) curve of the champion device. (d) Stabilized PCE and photocurrent density of the champion device measured at a bias of 0.43 V.

The PCE statistics of $FASnI_3$ PSCs prepared with different amounts of AHP are shown in Figure 4.6b. The control devices without AHP showed average PCE of 2.34±0.71%, V_{OC} of 0.25±0.05 V, short circuit current density (J_{SC}) of 17.72±1.65 $mAcm^{-2}$ and fill factor (FF) of 51.11±9.01%. With the introduction of AHP, the device performance was improved substantially. The devices with 5 mol% AHP showed an average PCE of 6.25±0.67%, V_{OC} of 0.50±0.03 V, J_{SC} of 19.55±0.79$mAcm^{-2}$ and FF of 63.71±4.47%. As discussed before, the enhanced photovoltaic performance can be ascribed to the improved perovskite film quality and reduction of defects. However, more addition of AHP led to decreased device performance, which may come from deteriorated perovskite films with pinholes and high roughness.

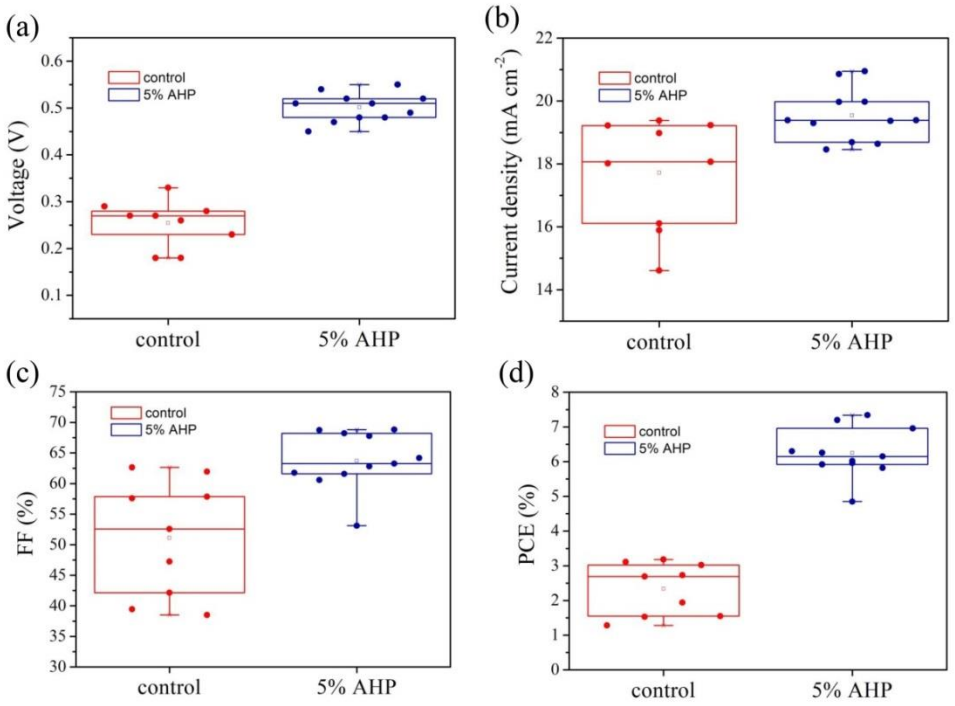

Figure 4.7 Distribution of photovoltaic parameters of plain $FASnI_3$ solar cells and 5 mol% AHP included $FASnI_3$solar cells, including (a) open voltage, (b) current density, (c) FF and (d) PCE.

The current density-voltage (J-V) curve of the champion PSC (5 mol% AHP) is shown in Figure 4.6c, achieving a PCE of 7.34% and V_{OC} of 0.55 V with negligible hysteresis. To verify the reliability of the device performance, the stabilized photocurrent and power output were measured at a bias of 0.43 V under AM 1.5 G illumination. As shown in Figure 4.6d, a stabilized output power of ~7.0% was achieved, which is close to the value obtained from the J-V curve. Notably, the V_{OC} up to 0.55 V is among the highest value for $FASnI_3$ based PSCs, which can be attributed to decreased defect density in perovskite film and the good energy alignment between perovskite and the hole transporting material CuSCN[202, 203]. Moreover, the photovoltaic parameters of control and 5 mol% AHP-modified devices are shown in **Figure 4.7.** The results clearly indicate that the introduction of AHP can improve both the reproducibility and efficiency of the devices.

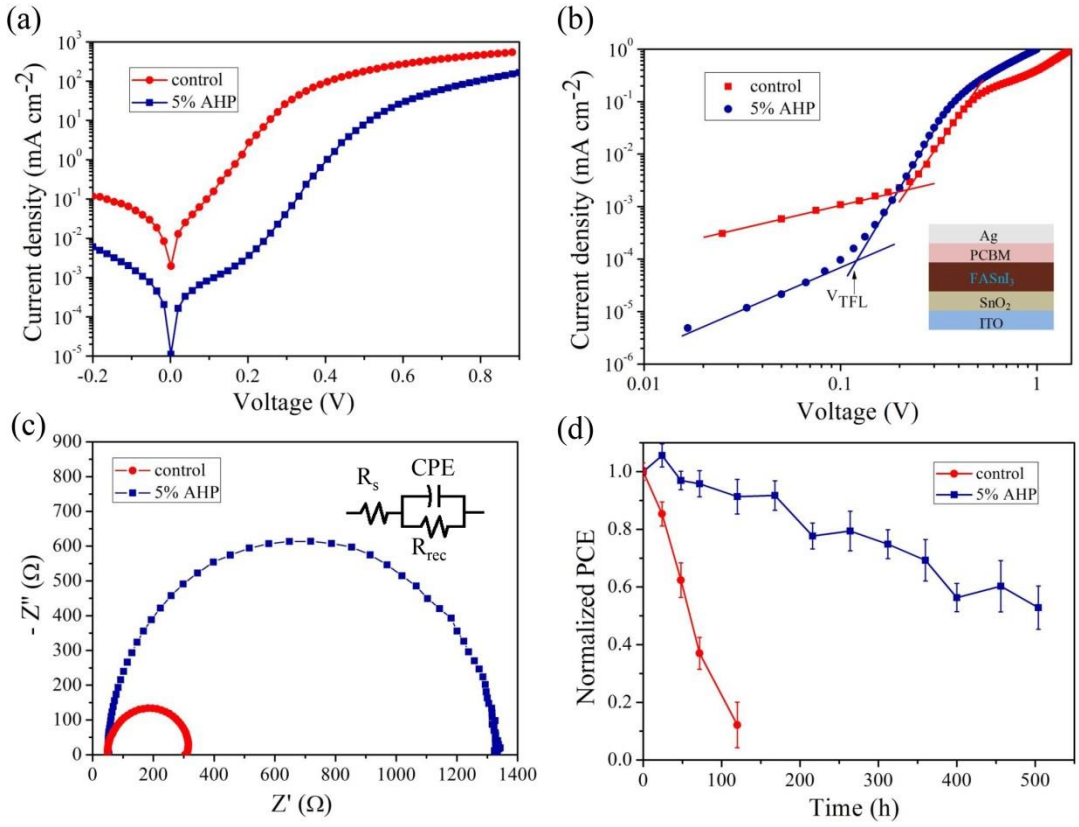

Figure 4.8 (a) J-V curves of $FASnI_3$ solar cells with and without AHP measured in dark. (b) J-V curves of electron-only devices. The insert shows the device structure. (c) Nyquist plots of $FASnI_3$ solar cells with and without AHP. (d) Normalized PCE of $FASnI_3$ solar cells as a function of storage time in ambient air with ~20% humidity.

To evaluate the charge transport properties of the devices, we measured the dark current density[204], as shown in **Figure 4.8**a. The plain $FASnI_3$ solar cells suffered from high leakage current because of the highly p-type doping. On the contrary, the 5 mol% AHP modified $FASnI_3$ solar cells showed good diode behavior with almost 1-2 orders lower leakage current than that of the control one, indicating its much reduced background carrier density[205].

We further measured the trap state density in the perovskite films by the space charge limited current (SCLC) method[206]. Electron-only devices with a structure of ITO/SnO_2/perovskite/PCBM/Ag were prepared to get dark J-V curves, as shown in Figure 4.8b. At low bias voltages, the J-V curves show linear relation, corresponding to the Ohmic region. With the bias voltage exceeding the kink point, the current density quickly increases, implying that the trap states are fully filled. Using the trap-filled limit voltage (V_{TFL}), we can obtain the trap state density N_t by this equation:

$N_t=2\varepsilon\varepsilon_0 V_{TFL}/qL^2$, where ε and ε_0 are the relative and vacuum dielectric constants, respectively, q is the elementary charge and L is the thickness of the perovskite film[207, 208]. The V_{TFL} of the control and AHP-included devices are around 0.22 V and 0.12 V, corresponding to trap state densities of 3.45×10^{15} cm^{-3} and 1.88×10^{15} cm^{-3}, respectively. The much lower trap state density of the AHP-modified perovskite film is favorable for the device performance.

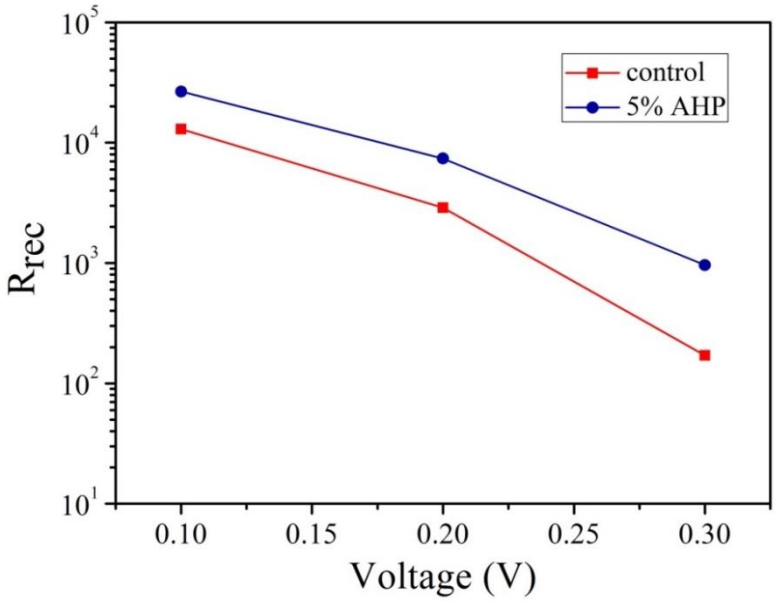

Figure 4.9 The fitted values of R_{rec} measured at different bias voltages.

To get further insight into the charge transport characteristics of the solar cells, electrochemical impedance spectroscopy of the PSCs was recorded[209, 210]. Figure 4.8c shows the Nyquist plots of the $FASnI_3$ solar cells without and with 5 mol% AHP addition, which were recorded at a bias of 0.3 V in dark. Generally, the semicircle at low frequency can be attributed to the recombination resistance (R_{rec}) and constant phase element (CPE), and the charge recombination rate is inversely proportional to recombination resistance[141, 211-213]. The R_{rec} values for the control and AHP-modified solar cells measured at different bias voltages are shown in **Figure 4.9**.The AHP–modified device had a much bigger R_{rec}, indicating a much lower recombination rate than that in the control.

In previous reports, the unencapsulated tin-based PSCs degraded quickly in ambient air. We examined the storage stability of the devices in air (without encapsulation), as

shown in Figure 4.8d. In air, about 50% of its original PCE was maintained after the storage for 500 h while the control devices degraded rapidly within 100 h. The enhanced long-term stability induced by AHP can be ascribed to the reducing effect of AHP around the perovskite grains as well as the compact and pinhole free film morphology that can effectively suppress the permeation of oxygen.

4.4 Summary

In summary, AHP was introduced into the perovskite precursor to suppress the oxidation of Sn^{2+} and retard the fast crystallization of $FASnI_3$. This method can substantially improve the film quality and decrease the trap density in the perovskite films. Meantime, inorganic CuSCN was used as hole transporting material for $FASnI_3$ PSCs to form good energy level alignment of the devices[19]. Consequently, improved photovoltaic performance was obtained in the resultant PSCs. Moreover, the AHP-included $FASnI_3$ PSCs demonstrate outstanding long term stability in ambient condition. Our work suggests that the combination of effective antioxidant additive and suitable hole extraction layer can improve the photovoltaic performance as well as the long-term stability of tin-based PSCs.

Chapter 5 High performance mixed Sn-Pb perovskite solar cells enabled by multiple functional additive

5.1 Introduction

Halide perovskites have the advantages of high absorption coefficient, long carrier diffusion length and low cost solution processability, making them attractive photovoltaic materials[1, 72, 144]. Single junction perovskite solar cells (PSC) have achieved certified power conversion efficiency (PCE) of 25%, which is close to the performance of silicon solar cells[2]. At present, high performance PSCs are based on multication mixed-halide perovskite absorbers, which have bandgaps around 1.5 – 1.6 eV[214]. However, the efficiency of single junction perovskite device is limited by Shockley-Queisser (S-Q) limit[47, 215], and the ideal bandgaps for single junction solar cells should be around 1.1 – 1.4 eV[216, 217]. Alloying Pb and Sn in perovskites can tune the bandgap down to 1.17 eV, making them ideal candidates for high performance single junction solar cells[127, 218]. Moreover, high performance low bandgap mixed Sn-Pb solar cells are essential for all perovskite tandem devices, which hold promise to exceed the S-Q limit[219, 220]. Nevertheless, it is still challenging to fabricate high efficiency mixed Sn-Pb PSCs due to the easy oxidation of Sn^{2+} to Sn^{4+}, leading to high level p-type doping and quick degradation of the devices[221].

A variety of efforts have been devoted to improving the performance and stability of low-bandgap mixed Sn-Pb PSCs. For example, excess Sn (II) compound such as SnF_2 has been introduced to Sn-based perovskites to suppress the oxidation of Sn^{2+} and reduce Sn vacancies. However, these SnF_2 additives are usually nonuniformly distributed, which may damage the film morphology of Sn-based perovskite films[188, 222]. Establishing 2D/3D hybrid structure Sn-based perovskite can slow down the permeation of oxygen to reduce Sn^{2+} oxidation[223, 224]. However, an excess of bulky organic cation in perovskite films usually leads to low fill factor, which may come

from restricted carrier transport in layered perovskites[225].

In this chapter, we introduced 4-hydrazinobenzoic acid (HBA) with multiple functional groups to enhance the efficiency and stability of mixed Sn-Pb perovskite solar cells. The hydrazine group of HBA could effectively suppress the oxidation of Sn^{2+}. Meantime, the carbonyl group in HBA could coordinate with Sn^{2+} components to slow down the crystallization rate of perovskite and enlarge the grain size. Moreover, it has been shown that undercoordinated lead ions (Pb^{2+}) have relatively low formation energy and are one of the common trap densities[226]. Here, these carbonyl groups of HBA at the grain boundaries can effectively passivate the uncoordinated Pb^{2+} defects to reduce nonradiative recombination. Benefiting from these effects, the champion mixed Sn-Pb PSCs achieved a high PCE of 20.14% with enhanced stability.

5.2 Devices Fabrication and Characterization

Materials: Formamidinium iodide (FAI) and methylammonium iodide (MAI) were purchased from Dyesol. Lead iodide (PbI_2), tin iodide (SnI_2) and tin fluorine (SnF_2) were obtained from Alpha Aesar. N,N-dimethylmethanamide (DMF), dimethyl-sulfoxide (DMSO) and diethyl ether were purchased form Sigma-Aldrich. Phenyl-C71-butyric acid methyl ester (PCBM) was purchased from Nano-C.

Device fabrication: ITO glass substrates were ultrasonically cleaned by deionized (DI) water, acetone and isopropanol for 15 min, respectively. The process of preparing NiO_x on ITO was similar to previous report. NiO_x dissolved in DI water (7.5 mg mL^{-1}) was spin-coated on the ITO substrate at 4000 rpm for 30 s in ambient air and then the films were annealed at 150℃ for 30 min in air. Then the films were transferred to N_2 glovebox for later experiments. The mixed Sn-Pb perovskite precursor was prepared by dissolving FAI (0.5 mmol), SnI_2 (0.5mmol), SnF_2 (0.05mmol), MAI (0.5 mmol) and PbI_2 (0.5 mmol) in mixed solvent (DMF: DMSO=4:1). For the HBA modification, the molar ratio of HBA and SnI_2 was 1.5%, 3% and 5%, respectively. The perovskite precursor solution was spin-coated on the NiO_x substrate at 1000 rpm for 10 s and 5000 rpm for 20 s, and diethyl ether was dropped on the film at 10^{th} s. Then, the perovskite films were annealed at 70℃ for 1 min and 100 ℃ for 10 min. Afterward,

PCBM (20 mg mL^{-1}) and BCP (0.5 mg mL^{-1}) were spin-coated on the films. Finally, 100 nm silver electrodes were thermally evaporated onto the films.

Characterization: J-V curves were measured by a Keithley 2400 source meter with a solar simulator under AM 1.5 G one sun illumination (Newport 66902). The EQE of the PSCs was obtained from an EQE system under DC mode. UV-vis spectra were collected on a UV-vis spectrometer (Perkin elmer). SEM images were measured by a field-emission SEM (Tescan MAIA3). The TEM images were collected by JEOL JEM 2100F operated at 200 kV. XRD patterns were measured using Cu Kα radiation (Rigaku, Smartlab). XPS and UPS were measured on Thermo Fisher Scientific system. The Nyquist plots were recorded by a Zennium X electrochemical workstation (Zahner, Germany).

5.3 Results and Discussion

The device structure of the perovskite solar cells and the chemical structure of HBA are illustrated in **Figure 5.1a**. Here, the planar inverted PSC was constructed with structure of indium tin oxide (ITO)/NiO_x/perovskite/PCBM/BCP/Ag.

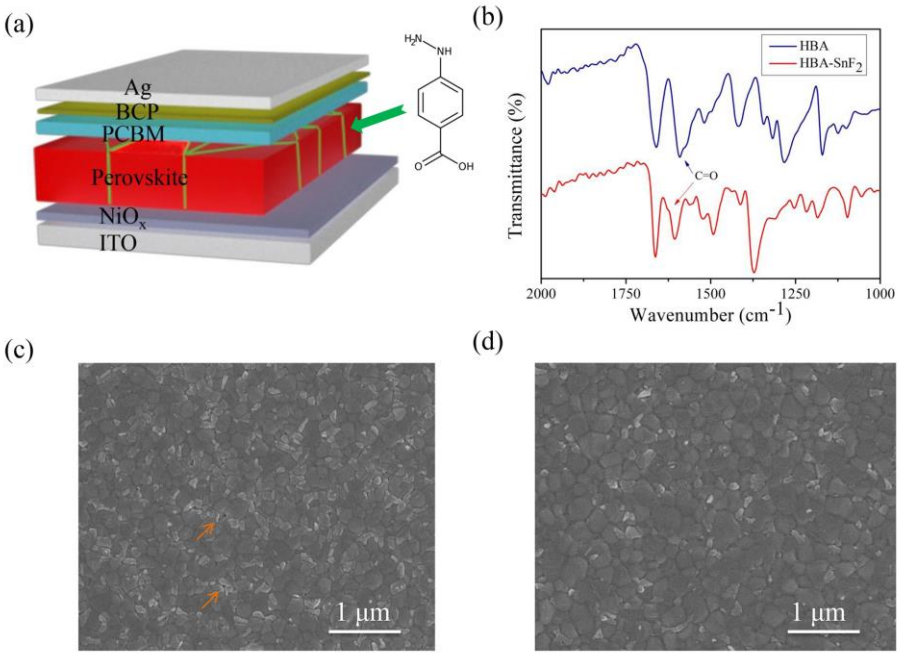

Figure 5.1 (a) Device structure and molecular structure of HBA. (b) FTIR spectra of HBA and HBA-SnF_2 complex. SEM images of mixed Sn-Pb perovskite films (c) without and (d) with HBA additive.

Fourier Transform Infrared Spectrometer (FTIR) spectroscopy measurement was performed to identify the interaction between HBA and Sn^{2+} ions as illustrated in Figure 5.1b. It can be found that the C=O vibration band of HBA shifted to higher wavenumber in the HBA-SnF_2 complex, which can be attributed to the coordinate effects between the lone electron pair of C=O and Sn^{2+} ions[227]. $(FASnI_3)_{0.5}(MAPbI_3)_{0.5}$ was chosen as the reference mixed Sn-Pb perovskite and SEM was used to evaluate the impact of HBA on the film morphology, as shown in Figure 5.1c,d. It is observed that the pristine perovskite film exhibited some small pinholes (marked as arrow in Figure 5.1c), which maybe resulted from the fast crystallization of Sn-containing perovskite films[172]. Interestingly, with the introduction of HBA, the perovskite film showed compact and pinhole free morphology with larger grain size. This can be ascribed to the coordination effect between C=O group of HBA and Sn^{2+} ions, which favored the formation of larger perovskite grains[228, 229].

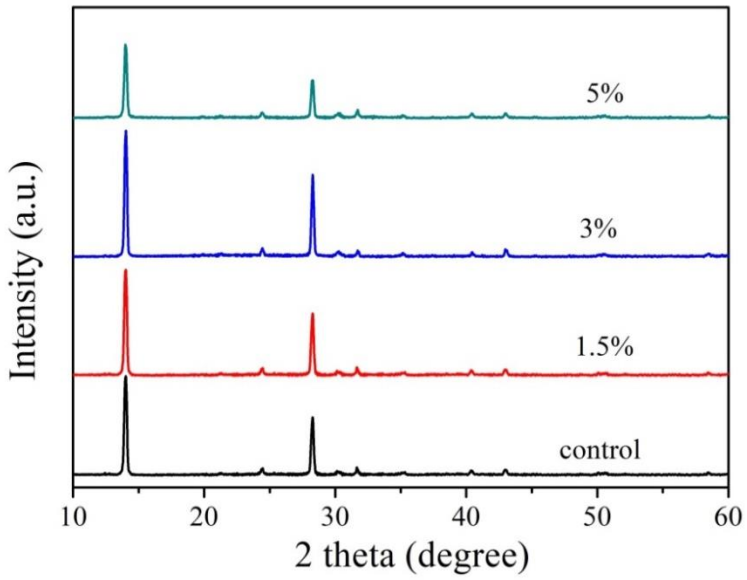

Figure 5.2 XRD pattern of perovskite films with various concentrations of HBA additive.

X-ray diffraction (XRD) patterns of the perovskite films with different amounts of HBA are shown in **Figure 5.2**. All the XRD patterns show similar characteristic peaks assigning to pseudo-cubic perovskite structure[230], indicating that HBA is not incorporated into the perovskite crystal structure. Meantime, the peak intensity of the perovskite with 3% HBA was much stronger than that of the pristine one, indicating the enhanced crystallinity of perovskite film.

To evaluate the reduction effect of HBA additive on Sn^{4+} in perovskite films, X-ray photoelectron spectroscopy (XPS) was conducted and the corresponding XPS spectra are shown in **Figure 5.3a,b**. The Sn (3d) band can be separated into two peaks associated with Sn^{2+} and Sn^{4+}, respectively[231]. The XPS spectra indicated that perovskite film with HBA additive had much less Sn^{4+} than that of the control one, which confirmed the reducing ability of HBA to retard the oxidation of Sn^{2+}.

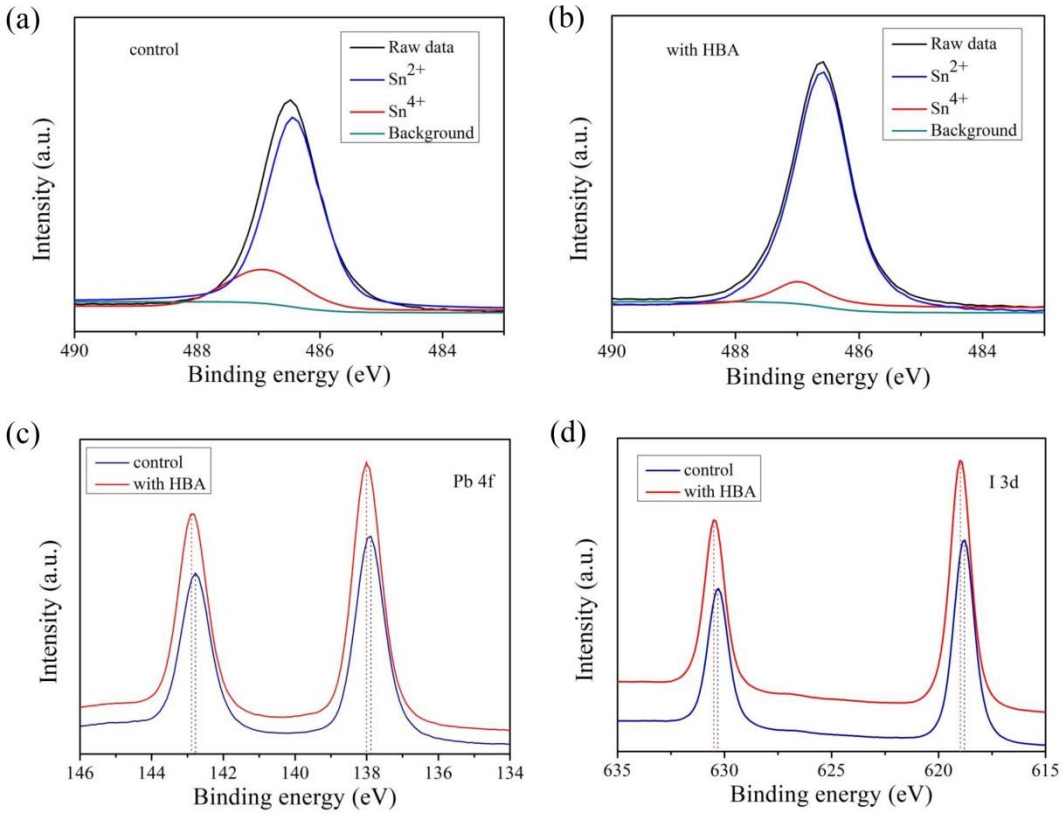

Figure 5.3 High-resolution XPS spectra (Sn 3d) of mixed Sn-Pb perovskite film (a) without and (b) with HBA additive. XPS spectra of (c) Pb and (d) I peaks of mixed Sn-Pb perovskite films with and without HBA additive.

Meantime, XPS is further used to investigate the chemical interaction between HBA and perovskite film. As shown in Figure 5.3c,d, the binding energies of Pb, I shifted to higher position, indicating the interaction between HBA and perovskite. It is reported that the C=O group is a Lewis base which can donate electron pair to the undercoordinated Pb^{2+} ions, suggesting the passivation effect of HBA[232]. Moreover, the hydrogen bonding interaction between O-H and I^- can reduce trap states and suppress iodide ions migration, leading to improved stability of perovskite film[233]. In

addition, the XPS spectra of characteristic element of O 1s confirmed the presence of HBA in perovskite film, as shown in **Figure 5.4**. Overall, the interaction between HBA and perovskite is beneficial for suppress the oxidation of Sn^{2+} and reduce trap states, resulting in enhanced film quality.

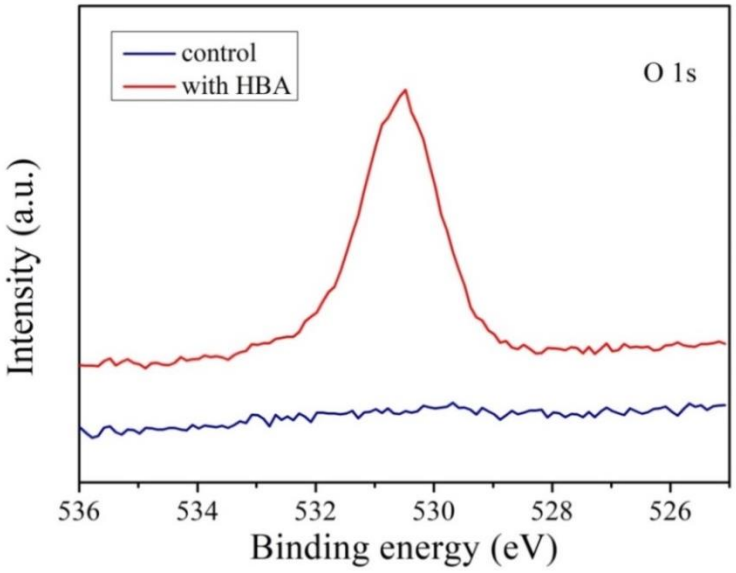

Figure 5.4 XPS spectra of O 1s for the control and HBA modified perovskite film.

The ultraviolet-visible absorption spectra of $(FASnI_3)_{0.5}(MAPbI_3)_{0.5}$ perovskite films with and without HBA are shown in **Figure 5.5a**, and there is no obvious change in the absorption curves. The bandgap of the perovskite films is estimated to be about 1.26 eV.

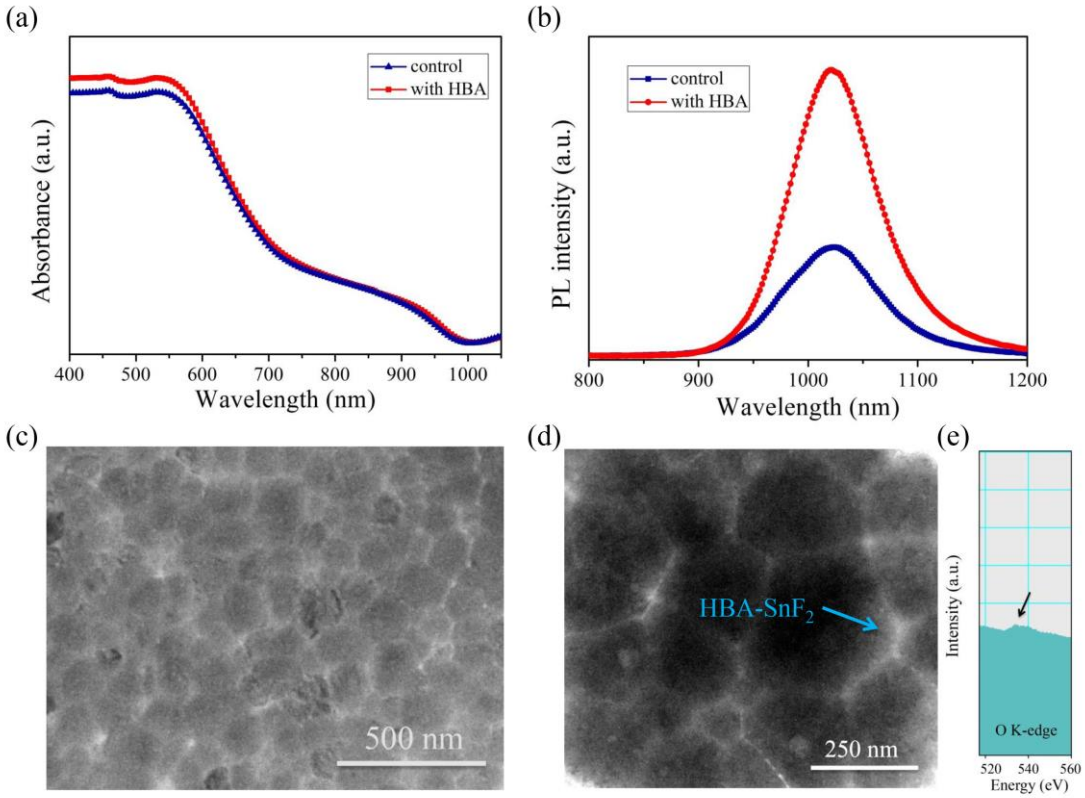

Figure 5.5 (a) UV-vis absorption spectra of perovskite films with and without HBA. (b) Steady state PL spectra of perovskite films with and without HBA. TEM images of perovskite films with HBA additive at (c) low magnification and (d) higher magnification. (e) O K-edge of EELS spectrum measured from the grain boundary region.

To investigate the charge carrier dynamics, steady-state PL spectroscopy of the perovskite films are performed and shown in Figure 5.5b. It can be found the HBA modified perovskite film shows much enhanced PL intensity, which indicates the suppressed nonradiative recombination due to less defects and enhanced crystallinity of HBA modified perovskite film.

To study the microstructure of the HBA modified perovskite film, transmission electron microscopy (TEM) characterization was performed. The TEM samples were prepared by directly solution-depositing the thin films on the TEM grids. As can be seen from Figure 5.5c, the $(FASnI_3)_{0.5}(MAPbI_3)_{0.5}$ perovskite grain and low-crystallinity HBA-SnF_2 complex can be differentiated from the image. A higher magnification TEM image is shown in Figure 5.5d, which displays the amorphous HBA-SnF_2 complex and crystalline perovskite grains more clearly.

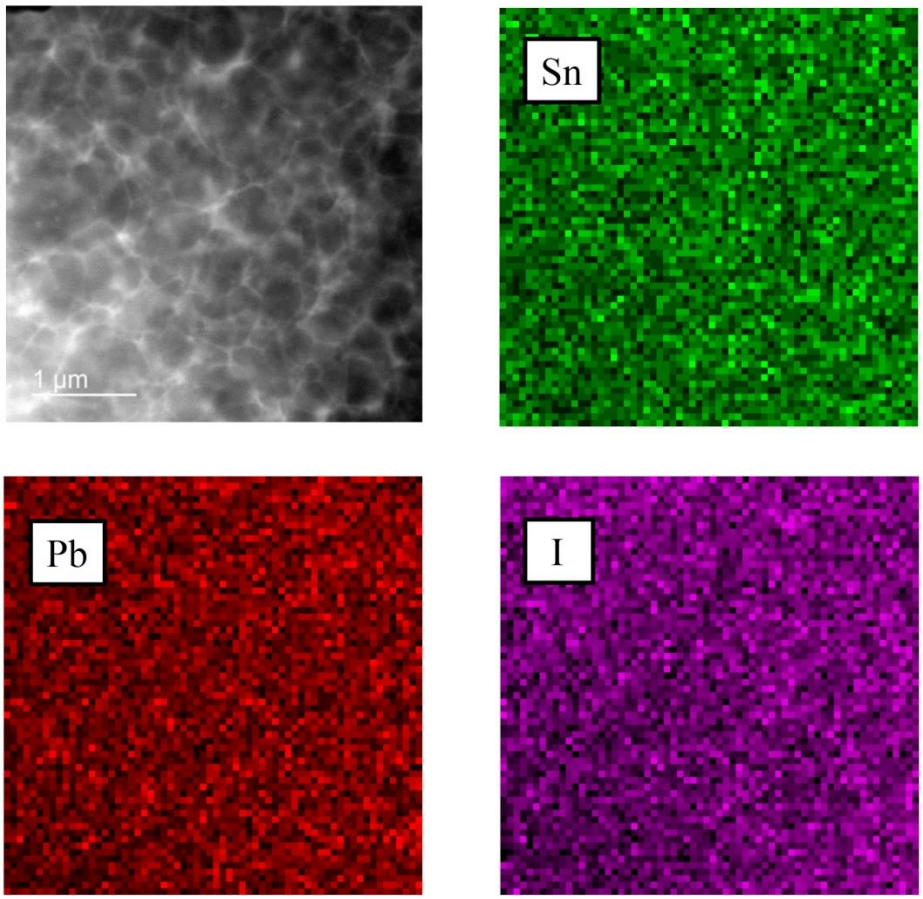

Figure 5.6 TEM image of HBA modified perovskite film and EDS elemental mapping of the film.

Moreover, electron-energy loss spectrum (EELS) was obtained from the grain boundary (GB) region and shown in Figure 5.5e, and the O K-edge signal can be clearly detected. This further confirms the presence of HBA-SnF_2 complex at the GB regions of the perovskite. The HBA-SnF_2 complex at grain boundaries can passivate defects and enhance the chemical stability of the perovskite films. Meantime, as shown in **Figure 5.6**, the energy dispersive spectroscopy (EDS) mapping of the perovskite film demonstrates the homogenous distribution of Pb, Sn and I across the film, confirming its phase purity.

To evaluate the charge transport and recombination process of the devices, dark J-V curve was measured. As shown in **Figure 5.7a**, the solar cell with HBA have much lower leakage current, which can be ascribed to decreased carrier generation rate and reduced background carrier density. In solar cells, the trap density is related with the

carrier generation rate, and this result suggests that the introduction of HBA can decrease the trap density in the devices[172, 234]. To quantitatively assess the defect density of the perovskite films, space charge limited current (SCLC) measurements were adopted (Figure 5.7b). The defect density (N_t) could be calculated from the equation: $N_t=(2\varepsilon\varepsilon_0V_{TFL})/(qL^2)$, where V_{TFL} indicates the trap-filled limit (TFL) voltage, L is the thickness of the perovskite film. Q is the elementary charge, ε and ε_0 are the dielectric constants of perovskite and vacuum, respectively. The defect density in perovskite films without and with HBA was estimated to be 3.87×10^{15} cm^{-3} and 2.52×10^{15} cm^{-3}, respectively. This result indicates that the incorporation of HBA can effectively reduce the defect density, leading to enhanced device performance.

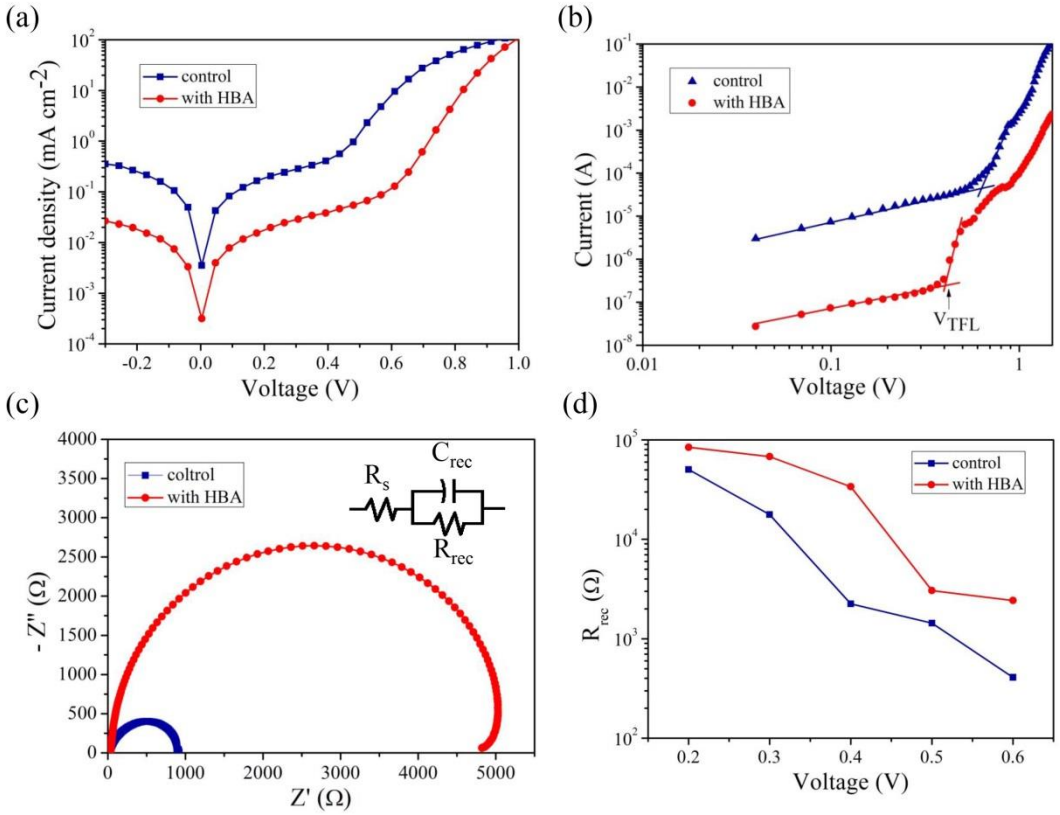

Figure 5.7 (a) Dark J-V curves of solar cells with and without HBA. (b) Dark I-V curves of the electron-only device, the device structure is ITO/SnO_2/perovskite/PCBM/Ag. (c) Nyquist plots of pristine and HBA modified perovskite solar cells measured in the dark (The inset shows the equivalent circuit for fitting the plots). (d) The fitted R_{rec} of solar cells at different applied voltages.

Electrochemical impedance spectroscopy (EIS) was further carried out to study the carrier dynamics in solar cells. The measurement was conducted in dark at different

applied biases. As shown in Figure 5.7c, the Nyquist plots show a main semicircle at low frequency, which can be interpreted as the recombination resistance (R_{rec})[172]. According to the equivalent circuit in the inset of Figure 5.7c, the fitted R_{rec} of devices under different bias are extracted and shown in Figure 5.7d. The device with HBA exhibits much larger R_{rec} than that of the control one, indicating that HBA can effectively suppress the charge recombination, which is beneficial for enhanced open voltage of the solar cells.

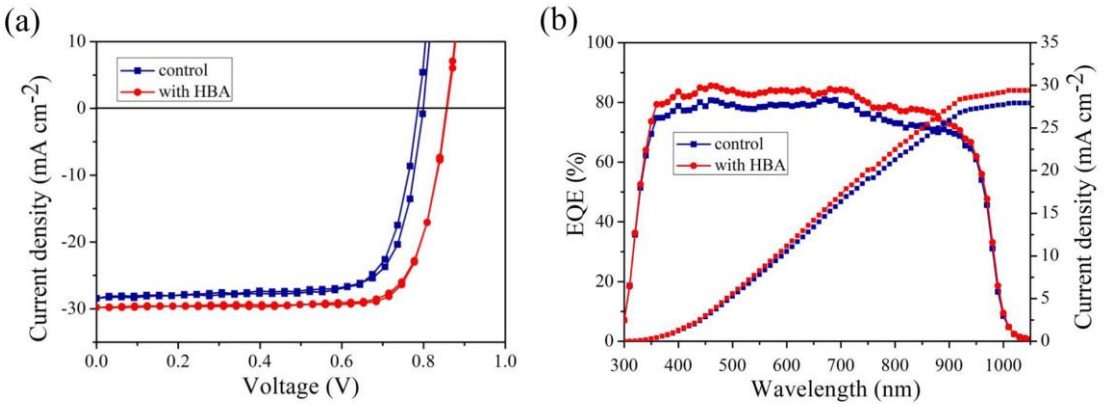

Figure 5.8 (a) J-V curves of the devices with and without HBA. (b) EQE and integrated J_{SC} of PSCs with and without HBA.

The current density-voltage (J-V) curves of the solar cells using $(FASnI_3)_{0.5}(MAPbI_3)_{0.5}$ perovskite films without and with HBA additive are shown in **Figure 5.8a**. The control device got a PCE of 17.16% with open voltage (V_{OC}) of 0.80 V, short-circuit current density (J_{SC}) of 28.45 mA cm^{-2} and fill factor (FF) of 75.39% (forward scan direction). With the introduction of HBA, the champion device achieved J_{SC} of 29.80 mA cm^{-2}, V_{OC} of 0.85 V and FF of 79.51%, yielding the maximum PCE of 20.14%.

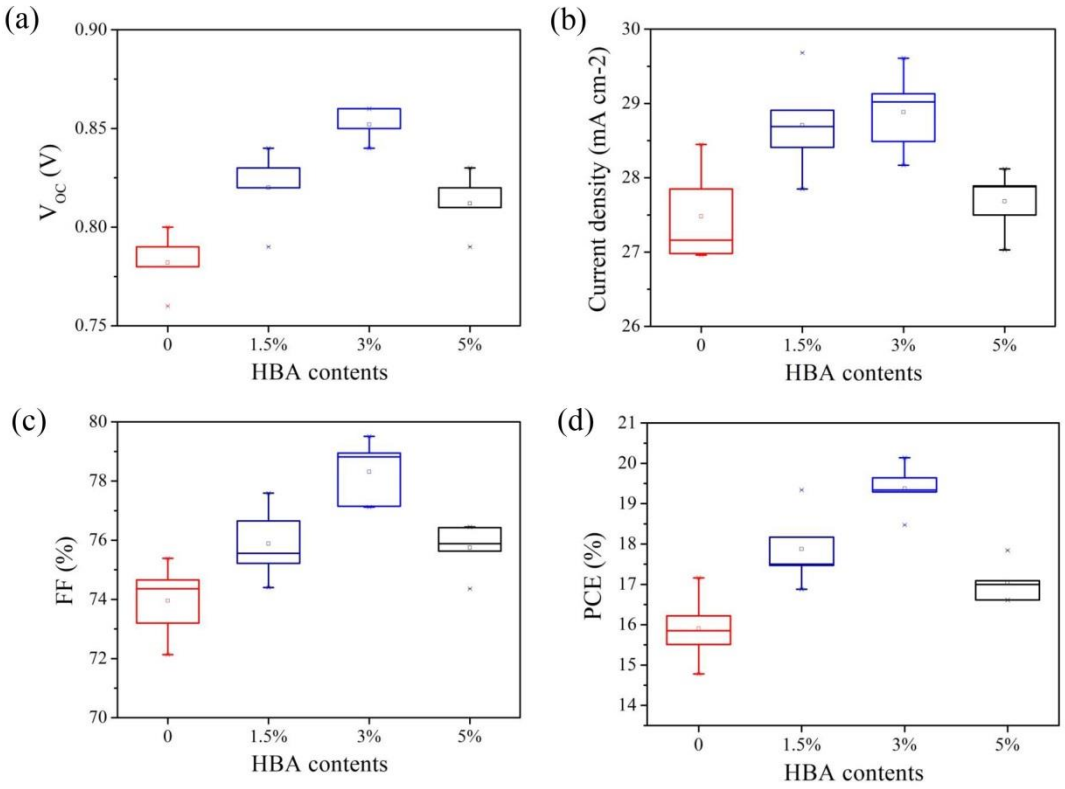

Figure 5.9 Photovoltaic parameters of PSCs with various amounts of HBA. (a) V_{OC}, (b) J_{SC}, (c) FF and (d) PCE.

The external quantum efficiency (EQE) of the PSCs and integrated J_{SC} are shown in Figure 5.8b, which agree with the values from the J-V curves. The statistical data of the photovoltaic parameters with different amounts of HBA are shown in **Figure 5.9**. The enhanced V_{OC} and FF can be attributed to the reduction of Sn^{4+} and suppressed recombination[235]. Meantime, the defects passivation effect of HBA also contributes to improved device performance.

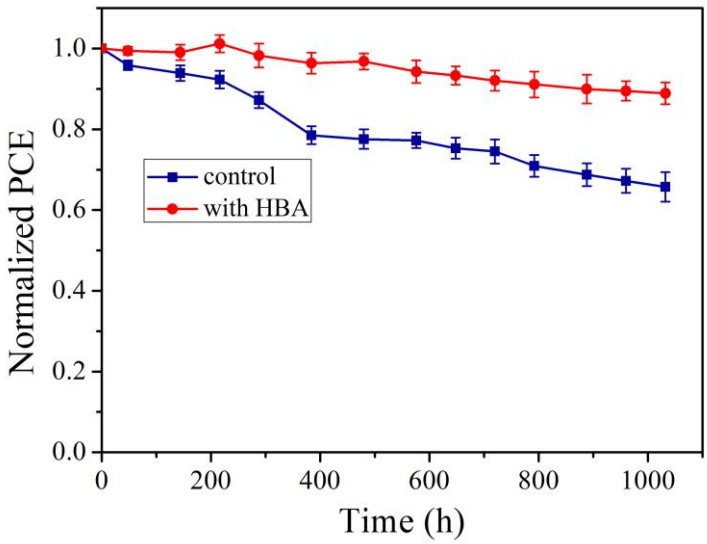

Figure 5.10 Shelf stability of the control and HBA modified solar cells stored in N_2 glovebox.

In addition, the shelf stability of the PSCs is also studied, as shown in **Figure 5.10**. The unencapsulated devices were stored in N_2 glovebox and measured under ambient condition at specific time interval. The HBA modified devices can retain about 90% of their initial efficiency after 1000 hours, while the control remained only about 65% of their initial values under the same condition. The enhanced shelf stability can be ascribed to the improved film morphology after HBA modification, which could block the permeation of oxygen and moisture. Meantime, the presence of HBA-SnF_2 complex at grain boundaries could passivate defects and inhibit Sn^{2+} oxidation, which is beneficial for enhanced device stability.

5.4 Summary

In summary, we introduced multiple functional additive HBA in mixed $(FASnI_3)_{0.5}(MAPbI_3)_{0.5}$ perovskite films and investigated its effect on crystallization of perovskite film and device performance. HBA can interact with Sn^{2+} ions to slow down the crystal growth process of perovskite, leading to enhanced crystallinity of perovskite with enlarged grain size. Meantime, the reduction effect of HBA can suppress the oxidation of Sn^{2+}, resulting in low Sn vacancies and stable perovskite phase. In addition, HBA remains at perovskite grain boundary may passivate uncoordinated ions to reduce trap states and suppress ions migration. As a result, the

PCE increased from 17.16% to 20.14% along with enhanced device stability. This work provides a simple and effective method to improve the efficiency and stability of mixed Sn-Pb perovskite solar cells.

Chapter 6 Conclusions and Future Outlook

6.1 Conclusions

Few layer WS_2 flakes were introduced as growth templates for the vdWs epitaxial growth of mixed perovskite films, leading to perovskite grains with enlarged sizes and a preferred orientation along (001). Moreover, perfect perovskite/WS_2 interface and the S···I interaction in it can facilitate efficient charge extraction and reduce interfacial carrier recombination. Resultantly, PSCs with a WS_2 interlayer show PCE up to 21.1% and excellent device stability. This work shows that high-mobility and defect-free 2D materials like WS_2 can be used as interfacial layers in PSCs to improve the device performance. In addition, the vdWs epitaxial growth of mixed perovskites on WS_2 may find important applications in other perovskite optoelectronic devices.

Then, AHP was introduced into the $FASnI_3$ perovskite precursor to suppress the oxidation of Sn^{2+} and retard the fast crystallization. This method can substantially enhance the perovskite film quality and decrease the trap density in the perovskite films. Meantime, inorganic hole transporting material CuSCN was introduced for $FASnI_3$ PSCs to form good energy level alignment of the devices. Consequently, improved photovoltaic performance was obtained along with outstanding long term stability. This work exhibits that the combination of effective antioxidant additive and suitable hole extraction layer can improve the photovoltaic performance as well as the long-term stability of tin-based PSCs.

In the next chapter, multiple functional additive HBA was introduced in mixed $(FASnI_3)_{0.5}(MAPbI_3)_{0.5}$ perovskite and its effect on crystallization of perovskite films was investigated. HBA can interact with Sn^{2+} ions to retard the crystal growth rate of perovskite, leading to enhanced crystallinity of perovskite with enlarged grain size. Meantime, the reduction effect of HBA can suppress the oxidation of Sn^{2+}, leading to low Sn vacancies and stable perovskite phase. In addition, HBA remains at perovskite grain boundary may passivate uncoordinated ions to reduce trap states and suppress ions migration. As a result, the PCE of mixed Sn-Pb PSCs increased from 17.16% to 20.14% along with enhanced device stability. This work provides a simple and

effective method to improve the efficiency and stability of mixed Sn-Pb perovskite solar cells.

6.2 Future Outlook

Epitaxial growth of perovskite films has been reported for lead-based perovskite, and this method may be used to prepare tin-based perovskite films to enhance their electronic properties.

Tin-based perovskite faces notorious stability issue, which hinders the further development of tin-based PSCs. Other reducing agents can be introduced to suppress the oxidation of Sn^{2+} as well as improve the film quality of tin-based perovskite, which may enable significant enhancement of the device performance.

Blending Sn with Pb, the mixed perovskites have low bandgaps from 1.1 eV to around 1.3 eV, making them excellent materials for ideal bandgap single-junction solar cells and subcells for all-perovskite tandem solar cells. However, the long term stability issue still needs to be solved before their commercial readiness. Compositional engineering has been showed as a successful way to prepare perovskite solar cells with significantly enhanced photoelectric performance. Chemical modification of the A site cations in mixed Sn-Pb PSCs can be a promising method to improve device performance and the long term stability.

The interfaces between perovskite and the charge transport layers should be paid more attention, which have great influence on the device performance and long term stability. Encouragingly, both efficiency and long term stability of PSCs have demonstrated great progress in the last few years. In short, we strongly believe that a new era of perovskite optoelectronics has just begun.

References

1. Kojima, A., et al., Organometal Halide Perovskites as Visible-Light Sensitizers for Photovoltaic Cells. Journal of the American Chemical Society, 2009. 131(17): p. 6050-6051.
2. NREL Efficiency Chart (Feb. 2020). Available from: https://www.nrel.gov/pv/assets/pdfs/best-research-cell-efficiencies.20200203.pdf.
3. Seok, S.I., M. Grätzel, and N.G. Park, Methodologies toward Highly Efficient Perovskite Solar Cells. Small, 2018.
4. Green, M.A., A. Ho-Baillie, and H.J. Snaith, The emergence of perovskite solar cells. Nature Photonics, 2014. 8(7): p. nphoton. 2014.134.
5. Goldschmidt, V.M., Die gesetze der krystallochemie. Naturwissenschaften, 1926. 14(21): p. 477-485.
6. Zhao, Y. and K. Zhu, Organic-inorganic hybrid lead halide perovskites for optoelectronic and electronic applications. Chemical Society Reviews, 2016. 45(3): p. 655-689.
7. Eperon, G.E., et al., Formamidinium lead trihalide: a broadly tunable perovskite for efficient planar heterojunction solar cells. Energy & Environmental Science, 2014. 7(3): p. 982-988.
8. Fan, Z., K. Sun, and J. Wang, Perovskites for photovoltaics: a combined review of organic-inorganic halide perovskites and ferroelectric oxide perovskites. Journal of Materials Chemistry A, 2015. 3(37): p. 18809-18828.
9. Johnston, M.B. and L.M. Herz, Hybrid Perovskites for Photovoltaics: Charge-Carrier Recombination, Diffusion, and Radiative Efficiencies. Accounts of Chemical Research, 2016. 49(1): p. 146-154.
10. Park, N.G., Perovskite solar cells: an emerging photovoltaic technology. Materials Today, 2015. 18(2): p. 65-72.
11. Shi, D., et al., Low trap-state density and long carrier diffusion in organolead trihalide perovskite single crystals. Science, 2015. 347(6221): p. 519-522.
12. Yin, W.J., T. Shi, and Y. Yan, Unique Properties of Halide Perovskites as Possible Origins of the Superior Solar Cell Performance. Advanced Materials,

2014. 26(27): p. 4653-4658.

13. Guanqi, T., et al., Performance Enhancement of Perovskite Solar Cells Induced by Lead Acetate as an Additive. Solar RRL, 2018. 2(6): p. 1800066.
14. Tsai, H., et al., High-efficiency two-dimensional Ruddlesden–Popper perovskite solar cells. Nature, 2016. 536: p. 312.
15. Shi, E., et al., Two-dimensional halide perovskite nanomaterials and heterostructures. Chemical Society Reviews, 2018.
16. Tang, Z., J. Guan, and A.M. Guloy, Synthesis and crystal structure of new organic-based layered perovskites with 2,2′-biimidazolium cations. Journal of Materials Chemistry, 2001. 11(2): p. 479-482.
17. Mao, L., et al., Hybrid Dion–Jacobson 2D Lead Iodide Perovskites. Journal of the American Chemical Society, 2018. 140(10): p. 3775-3783.
18. Chen, J. and N.G. Park, Causes and Solutions of Recombination in Perovskite Solar Cells. Advanced Materials, 2019. 31(47): p. 1803019.
19. Chen, J. and N.G. Park, Inorganic Hole Transporting Materials for Stable and High Efficiency Perovskite Solar Cells. The Journal of Physical Chemistry C, 2018. 122(25): p. 14039-14063.
20. Meng, L., et al., Recent Advances in the Inverted Planar Structure of Perovskite Solar Cells. Accounts of Chemical Research, 2016. 49(1): p. 155-165.
21. Uddin, A., et al., Encapsulation of organic and perovskite solar cells: a review. Coatings, 2019. 9(2): p. 65.
22. Koushik, D., et al., High-efficiency humidity-stable planar perovskite solar cells based on atomic layer architecture. Energy & Environmental Science, 2017. 10(1): p. 91-100.
23. Tanenbaum, D.M., et al., Edge sealing for low cost stability enhancement of roll-to-roll processed flexible polymer solar cell modules. Solar Energy Materials and Solar Cells, 2012. 97: p. 157-163.
24. Kim, N., et al., A correlation study between barrier film performance and shelf lifetime of encapsulated organic solar cells. Solar Energy Materials and Solar Cells, 2012. 101: p. 140-146.
25. Han, Y., et al., Degradation observations of encapsulated planar $CH_3NH_3PbI_3$

perovskite solar cells at high temperatures and humidity. Journal of Materials Chemistry A, 2015. 3(15): p. 8139-8147.

26. Lv, R., et al., Transition Metal Dichalcogenides and Beyond: Synthesis, Properties, and Applications of Single- and Few-Layer Nanosheets. Accounts of Chemical Research, 2015. 48(1): p. 56-64.
27. Capasso, A., et al. Spray deposition of exfoliated MoS_2 flakes as hole transport layer in perovskite-based photovoltaics. in 2015 IEEE 15th International Conference on Nanotechnology (IEEE-NANO). 2015.
28. Kim, Y.G., et al., Atomically thin two-dimensional materials as hole extraction layers in organolead halide perovskite photovoltaic cells. Journal of Power Sources, 2016. 319: p. 1-8.
29. Dasgupta, U., S. Chatterjee, and A.J. Pal, Thin-film formation of 2D MoS_2 and its application as a hole-transport layer in planar perovskite solar cells. Solar Energy Materials and Solar Cells, 2017. 172: p. 353-360.
30. Huang, P., et al., Water-Soluble 2D Transition Metal Dichalcogenides as the Hole-Transport Layer for Highly Efficient and Stable p–i–n Perovskite Solar Cells. ACS Applied Materials & Interfaces, 2017. 9(30): p. 25323-25331.
31. Kakavelakis, G., et al., Extending the Continuous Operating Lifetime of Perovskite Solar Cells with a Molybdenum Disulfide Hole Extraction Interlayer. Advanced Energy Materials, 2018. 8(12): p. 1702287.
32. Dai, R., et al., Metal–Organic-Compound-Modified MoS_2 with Enhanced Solubility for High-Performance Perovskite Solar Cells. ChemSusChem, 2017. 10(14): p. 2869-2874.
33. Capasso, A., et al., Few-Layer MoS_2 Flakes as Active Buffer Layer for Stable Perovskite Solar Cells. Advanced Energy Materials, 2016. 6(16): p. 1600920.
34. Divitini, G., et al., In situ observation of heat-induced degradation of perovskite solar cells. Nature Energy, 2016. 1(2): p. 15012.
35. Najafi, L., et al., MoS_2 Quantum Dot/Graphene Hybrids for Advanced Interface Engineering of a $CH_3NH_3PbI_3$ Perovskite Solar Cell with an Efficiency of over 20%. ACS Nano, 2018. 12(11): p. 10736-10754.
36. Choi, Y., et al., Enhanced Charge Transport via Metallic 1T Phase Transition Metal Dichalcogenides-Mediated Hole Transport Layer Engineering for

Perovskite Solar Cells. ChemNanoMat, 2019. 5(8): p. 1050-1058.

37. Zhao, E., et al., In situ fabrication of 2D SnS_2 nanosheets as a new electron transport layer for perovskite solar cells. Nano Research, 2018. 11(11): p. 5913-5923.
38. Zhao, X., et al., 20% Efficient Perovskite Solar Cells with 2D Electron Transporting Layer. Advanced Functional Materials, 2019. 29(4): p. 1805168.
39. Yin, G., et al., Low-temperature and facile solution-processed two-dimensional TiS_2 as an effective electron transport layer for UV-stable planar perovskite solar cells. Journal of Materials Chemistry A, 2018. 6(19): p. 9132-9138.
40. Huang, P., et al., Room-Temperature and Aqueous Solution-Processed Two-Dimensional TiS_2 as an Electron Transport Layer for Highly Efficient and Stable Planar n–i–p Perovskite Solar Cells. ACS Applied Materials & Interfaces, 2018. 10(17): p. 14796-14802.
41. Huang, P., et al., 21.7% efficiency achieved in planar n–i–p perovskite solar cells via interface engineering with water-soluble 2D TiS_2. Journal of Materials Chemistry A, 2019. 7(11): p. 6213-6219.
42. Wang, Y., et al., Largely enhanced V_{OC} and stability in perovskite solar cells with modified energy match by coupled 2D interlayers. Journal of Materials Chemistry A, 2018. 6(11): p. 4860-4867.
43. Imran, M., et al., Highly efficient and stable inverted perovskite solar cells with two-dimensional ZnSe deposited using a thermal evaporator for electron collection. Journal of Materials Chemistry A, 2018. 6(45): p. 22713-22720.
44. Coskun, H., et al., Thermally evaporated two-dimensional SnS as an efficient and stable electron collection interlayer for inverted planar perovskite solar cells. Journal of Materials Chemistry A, 2019. 7(9): p. 4759-4765.
45. Wang, K., et al., Lead Replacement in $CH_3NH_3PbI_3$ Perovskites. Advanced Electronic Materials, 2015. 1(10): p. 1500089.
46. Stoumpos, C.C., C.D. Malliakas, and M.G. Kanatzidis, Semiconducting Tin and Lead Iodide Perovskites with Organic Cations: Phase Transitions, High Mobilities, and Near-Infrared Photoluminescent Properties. Inorganic Chemistry, 2013. 52(15): p. 9019-9038.

47. Shockley, W. and H.J. Queisser, Detailed Balance Limit of Efficiency of p-n Junction Solar Cells. Journal of Applied Physics, 1961. 32(3): p. 510-519.
48. Kagan, C.R., D.B. Mitzi, and C.D. Dimitrakopoulos, Organic-Inorganic Hybrid Materials as Semiconducting Channels in Thin-Film Field-Effect Transistors. Science, 1999. 286(5441): p. 945.
49. Mitzi, D.B., C.D. Dimitrakopoulos, and L.L. Kosbar, Structurally Tailored Organic−Inorganic Perovskites: Optical Properties and Solution-Processed Channel Materials for Thin-Film Transistors. Chemistry of Materials, 2001. 13(10): p. 3728-3740.
50. Chen, Z., et al., Schottky solar cells based on $CsSnI_3$ thin-films. Applied Physics Letters, 2012. 101(9): p. 093901.
51. Hao, F., et al., Lead-free solid-state organic–inorganic halide perovskite solar cells. Nature Photonics, 2014. 8(6): p. 489-494.
52. Noel, N.K., et al., Lead-free organic–inorganic tin halide perovskites for photovoltaic applications. Energy & Environmental Science, 2014. 7(9): p. 3061-3068.
53. Shao, S., et al., Highly Reproducible Sn-Based Hybrid Perovskite Solar Cells with 9% Efficiency. Advanced Energy Materials, 2017: p. 1702019.
54. Chung, I., et al., $CsSnI_3$: Semiconductor or Metal? High Electrical Conductivity and Strong Near-Infrared Photoluminescence from a Single Material. High Hole Mobility and Phase-Transitions. Journal of the American Chemical Society, 2012. 134(20): p. 8579-8587.
55. Ma, L., et al., Carrier Diffusion Lengths of over 500 nm in Lead-Free Perovskite $CH_3NH_3SnI_3$ Films. J Am Chem Soc, 2016. 138(44): p. 14750-14755.
56. Noel, N.K., et al., Lead-free organic–inorganic tin halide perovskites for photovoltaic applications. Energy Environ. Sci., 2014. 7(9): p. 3061-3068.
57. Binek, A., et al., Stabilization of the Trigonal High-Temperature Phase of Formamidinium Lead Iodide. The Journal of Physical Chemistry Letters, 2015. 6(7): p. 1249-1253.
58. Zeng, L.H., et al., Multilayered $PdSe_2$/Perovskite Schottky Junction for Fast, Self-Powered, Polarization-Sensitive, Broadband Photodetectors, and Image

Sensor Application. Advanced Science, 2019. 6(19): p. 1901134.

59. Shi, T., et al., Effects of organic cations on the defect physics of tin halide perovskites. Journal of Materials Chemistry A, 2017. 5(29): p. 15124-15129.
60. Koh, T.M., et al., Formamidinium tin-based perovskite with low E_g for photovoltaic applications. Journal of Materials Chemistry A, 2015. 3(29): p. 14996-15000.
61. Li, W., et al., Addictive-assisted construction of all-inorganic $CsSnIBr_2$ mesoscopic perovskite solar cells with superior thermal stability up to 473 K. Journal of Materials Chemistry A, 2016. 4(43): p. 17104-17110.
62. Ning, W., et al., Heterojunction-Depleted Lead-Free Perovskite Solar Cells with Coarse-Grained B-γ-$CsSnI_3$ Thin Films. Advanced Energy Materials, 2016. 6(24): p. 1601130.
63. Koji, Y., et al., Structural Phase Transitions of the Polymorphs of $CsSnI_3$ by Means of Rietveld Analysis of the X-Ray Diffraction. Chemistry Letters, 1991. 20(5): p. 801-804.
64. Kontos, A.G., et al., Structural Stability, Vibrational Properties, and Photoluminescence in $CsSnI_3$ Perovskite upon the Addition of SnF_2. Inorganic Chemistry, 2017. 56(1): p. 84-91.
65. Qiu, X., et al., From unstable $CsSnI_3$ to air-stable Cs_2SnI_6: A lead-free perovskite solar cell light absorber with bandgap of 1.48eV and high absorption coefficient. Solar Energy Materials and Solar Cells, 2017. 159: p. 227-234.
66. Shum, K., et al., Synthesis and characterization of $CsSnI_3$ thin films. Applied Physics Letters, 2010. 96(22): p. 221903.
67. Yu, C., et al., First-principles study of structural phase transitions in $CsSnI_3$. Journal of Applied Physics, 2013. 114(16): p. 163505.
68. Hemant, K.M., et al., Lead-Free Halide Perovskite Solar Cells with High Photocurrents Realized Through Vacancy Modulation. Advanced Materials, 2014. 26(41): p. 7122-7127.
69. Giorgi, G., et al., Small Photocarrier Effective Masses Featuring Ambipolar Transport in Methylammonium Lead Iodide Perovskite: A Density Functional Analysis. The Journal of Physical Chemistry Letters, 2013. 4(24): p.

4213-4216.

70. Xu, P., et al., Influence of Defects and Synthesis Conditions on the Photovoltaic Performance of Perovskite Semiconductor $CsSnI_3$. Chemistry of Materials, 2014. 26(20): p. 6068-6072.
71. Xie, G., et al., Insight into the reaction mechanism of water, oxygen and nitrogen molecules on a tin iodine perovskite surface. Journal of Materials Chemistry A, 2019. 7(10): p. 5779-5793.
72. Tai, Q., et al., Recent advances toward efficient and stable tin-based perovskite solar cells. EcoMat, 2019. 1(1): p. e12004.
73. Min, X., et al., Tin-Based Perovskite with Improved Coverage and Crystallinity through Tin-Fluoride-Assisted Heterogeneous Nucleation. Advanced Optical Materials, 2018. 6(1): p. 1700615.
74. Marshall, K.P., R.I. Walton, and R.A. Hatton, Tin perovskite/fullerene planar layer photovoltaics: improving the efficiency and stability of lead-free devices. Journal of Materials Chemistry A, 2015. 3(21): p. 11631-11640.
75. Heo, J.H., et al., Roles of SnX_2 (X = F, Cl, Br) Additives in Tin-Based Halide Perovskites toward Highly Efficient and Stable Lead-Free Perovskite Solar Cells. The Journal of Physical Chemistry Letters, 2018. 9(20): p. 6024-6031.
76. Lee, B., et al., All-solid-state dye-sensitized solar cells with high efficiency. Nature, 2012. 485(7399): p. 486.
77. Hartmann, C., et al., Impact of SnF_2 Addition on the Chemical and Electronic Surface Structure of $CsSnBr_3$. ACS Applied Materials & Interfaces, 2020. 12(10): p. 12353-12361.
78. Liao, W., et al., Lead-Free Inverted Planar Formamidinium Tin Triiodide Perovskite Solar Cells Achieving Power Conversion Efficiencies up to 6.22. Adv Mater, 2016. 28(42): p. 9333-9340.
79. Ke, W., et al., Dopant-Free Tetrakis-Triphenylamine Hole Transporting Material for Efficient Tin-Based Perovskite Solar Cells. Journal of the American Chemical Society, 2018. 140(1): p. 388-393.
80. Pengchen, Z., et al., $CsSnI_3$ Solar Cells via an Evaporation-Assisted Solution Method. Solar RRL, 2018. 2(4): p. 1700224.
81. Oda, C. and J. Ingle, Speciation of mercury with cold vapor atomic absorption

spectrometry by selective reduction. Analytical Chemistry, 1981. 53(14): p. 2305-2309.

82. Marshall, K.P., et al., Enhanced stability and efficiency in hole-transport-layer-free $CsSnI_3$ perovskite photovoltaics. Nature Energy, 2016. 1: p. 16178.
83. Shao, Y., Y. Yuan, and J. Huang, Correlation of energy disorder and open-circuit voltage in hybrid perovskite solar cells. Nature Energy, 2016. 1: p. 15001.
84. He, Y., et al., Indene−C_{60} Bisadduct: A New Acceptor for High-Performance Polymer Solar Cells. Journal of the American Chemical Society, 2010. 132(4): p. 1377-1382.
85. Zhang, W., et al., Enhanced optoelectronic quality of perovskite thin films with hypophosphorous acid for planar heterojunction solar cells. Nature communications, 2015. 6: p. 10030.
86. Song, T.B., et al., Importance of Reducing Vapor Atmosphere in the Fabrication of Tin-Based Perovskite Solar Cells. Journal of the American Chemical Society, 2017. 139(2): p. 836-842.
87. Song, T.-B., et al., Performance Enhancement of Lead-Free Tin-Based Perovskite Solar Cells with Reducing Atmosphere-Assisted Dispersible Additive. ACS Energy Letters, 2017. 2(4): p. 897-903.
88. Kayesh, M.E., et al., Enhanced Photovoltaic Performance of $FASnI_3$-Based Perovskite Solar Cells with Hydrazinium Chloride Coadditive. ACS Energy Letters, 2018: p. 1584-1589.
89. Brion, B., et al., The Development of Hydrazine-Processed $Cu(In,Ga)(Se,S)_2$ Solar Cells. Advanced Energy Materials, 2012. 2(5): p. 504-522.
90. Miki, H., Method for producing copper powder. 1998, Google Patents.
91. Williams, S.T., et al., Role of Chloride in the Morphological Evolution of Organo-Lead Halide Perovskite Thin Films. ACS Nano, 2014. 8(10): p. 10640-10654.
92. Gu, F., et al., Improving Performance of Lead-Free Formamidinium Tin Triiodide Perovskite Solar Cells by Tin Source Purification. Solar RRL, 2018. 2(10): p. 1800136.

93. Song, T.B., et al., Piperazine Suppresses Self-Doping in $CsSnI_3$ Perovskite Solar Cells. ACS Applied Energy Materials, 2018. 1(8): p. 4221-4226.

94. Yu, B.B., et al., Synergy Effect of Both 2,2,2-Trifluoroethylamine Hydrochloride and SnF_2 for Highly Stable $FASnI_{3-x}Cl_x$ Perovskite Solar Cells. Solar RRL, 2019. 3(3): p. 1800290.

95. Hoshi, H., N. Shigeeda, and T. Dai, Improved oxidation stability of tin iodide cubic perovskite treated by 5-ammonium valeric acid iodide. Materials Letters, 2016. 183: p. 391-393.

96. Ghufran, H.S., et al., Air Processed Inkjet Infiltrated Carbon Based Printed Perovskite Solar Cells with High Stability and Reproducibility. Advanced Materials Technologies, 2017. 2(1): p. 1600183.

97. Mei, A., et al., A hole-conductor–free, fully printable mesoscopic perovskite solar cell with high stability. Science, 2014. 345(6194): p. 295-298.

98. Kayesh, M.E., et al., Coadditive Engineering with 5-Ammonium Valeric Acid Iodide for Efficient and Stable Sn Perovskite Solar Cells. ACS Energy Letters, 2019. 4(1): p. 278-284.

99. Li, F., et al., Trihydrazine Dihydriodide-Assisted Fabrication of Efficient Formamidinium Tin Iodide Perovskite Solar Cells. Solar RRL, 2019. 3(9): p. 1900285.

100. He, X., et al., Highly efficient tin perovskite solar cells achieved in a wide oxygen concentration range. Journal of Materials Chemistry A, 2020.

101. Wang, M., et al., Efficient $CsSnI_3$-based inorganic perovskite solar cells based on mesoscopic metal oxide framework via incorporating donor element. Journal of Materials Chemistry A, 2020.

102. Yokoyama, T., et al., Overcoming Short-Circuit in Lead-Free $CH_3NH_3SnI_3$ Perovskite Solar Cells via Kinetically Controlled Gas–Solid Reaction Film Fabrication Process. The Journal of Physical Chemistry Letters, 2016. 7(5): p. 776-782.

103. Hao, F., et al., Solvent-Mediated Crystallization of $CH_3NH_3SnI_3$ Films for Heterojunction Depleted Perovskite Solar Cells. Journal of the American Chemical Society, 2015. 137(35): p. 11445-11452.

104. Liu, X., et al., Solvent Engineering Improves Efficiency of Lead-Free

Tin-Based Hybrid Perovskite Solar Cells beyond 9%. ACS Energy Letters, 2018. 3(11): p. 2701-2707.

105. Jeon, N.J., et al., Solvent engineering for high-performance inorganic–organic hybrid perovskite solar cells. Nature materials, 2014. 13(9): p. 897.
106. Ahn, N., et al., Highly reproducible perovskite solar cells with average efficiency of 18.3% and best efficiency of 19.7% fabricated via Lewis base adduct of lead (II) iodide. Journal of the American Chemical Society, 2015. 137(27): p. 8696-8699.
107. Ahn, N., et al., Highly Reproducible Perovskite Solar Cells with Average Efficiency of 18.3% and Best Efficiency of 19.7% Fabricated via Lewis Base Adduct of Lead(II) Iodide. Journal of the American Chemical Society, 2015. 137(27): p. 8696-8699.
108. Lee, J.-W., et al., Tuning Molecular Interactions for Highly Reproducible and Efficient Formamidinium Perovskite Solar Cells via Adduct Approach. Journal of the American Chemical Society, 2018. 140(20): p. 6317-6324.
109. Liu, J., et al., Lead-Free Solar Cells based on Tin Halide Perovskite Films with High Coverage and Improved Aggregation. Angewandte Chemie International Edition, 2018. 57(40): p. 13221-13225.
110. Lee, S.J., et al., Fabrication of Efficient Formamidinium Tin Iodide Perovskite Solar Cells through SnF_2-Pyrazine Complex. J Am Chem Soc, 2016. 138(12): p. 3974-7.
111. Chen, C.C., et al., Interplay between nucleation and crystal growth during the formation of $CH_3NH_3PbI_3$ thin films and their application in solar cells. Solar Energy Materials and Solar Cells, 2017. 159: p. 583-589.
112. Fujihara, T., et al., Fabrication of high coverage $MASnI_3$ perovskite films for stable, planar heterojunction solar cells. Journal of Materials Chemistry C, 2017. 5(5): p. 1121-1127.
113. He, L., et al., Efficient Anti-solvent-free Spin-Coated and Printed Sn-Perovskite Solar Cells with Crystal-Based Precursor Solutions. Matter, 2020. 2(1): p. 167-180.
114. Godel, K.C., et al., Efficient room temperature aqueous Sb_2S_3 synthesis for inorganic-organic sensitized solar cells with 5.1% efficiencies. Chemical

Communications, 2015. 51(41): p. 8640-8643.

115. Liu, C., et al., Enhanced Hole Transportation for Inverted Tin-Based Perovskite Solar Cells with High Performance and Stability. Advanced Functional Materials, 2019. 29(18): p. 1808059.
116. Meng, X., et al., Highly Stable and Efficient $FASnI_3$-Based Perovskite Solar Cells by Introducing Hydrogen Bonding. Advanced Materials. 0(0): p. 1903721.
117. Tianhao, W., et al., Efficient and stable tin-based perovskite solar cells by introducing π-conjugated Lewis base. SCIENCE CHINA Chemistry, (1674-7291).
118. Cao, D.H., et al., Thin Films and Solar Cells Based on Semiconducting Two-Dimensional Ruddlesden–Popper $(CH_3(CH_2)_3NH_3)_2(CH_3NH_3)_{n-1}Sn_nI_{3n+1}$ Perovskites. ACS Energy Letters, 2017. 2(5): p. 982-990.
119. Zonglong, Z., et al., Realizing Efficient Lead-Free Formamidinium Tin Triiodide Perovskite Solar Cells via a Sequential Deposition Route. Advanced Materials, 2018. 30(6): p. 1703800.
120. Liangliang, D., et al., Polymer assist crystallization and passivation for enhancements of open-circuit voltage and stability in tin-halide perovskite solar cells. Journal of Physics D: Applied Physics, 2018. 51(47): p. 475102.
121. Wu, C., et al., Highly-Stable Organo-Lead Halide Perovskites Synthesized Through Green Self-Assembly Process. Solar RRL, 2018. 2(6): p. 1800052.
122. Liu, G., et al., Regulated Crystallization of Efficient and Stable Tin-Based Perovskite Solar Cells via a Self-Sealing Polymer. ACS Applied Materials & Interfaces, 2020.
123. Xu, X., et al., Ascorbic acid as an effective antioxidant additive to enhance the efficiency and stability of Pb/Sn-based binary perovskite solar cells. Nano Energy, 2017. 34: p. 392-398.
124. Chowdhury, T.H., et al., Post-Deposition Vapor Annealing Enables Fabrication of 1 cm2 Lead-Free Perovskite Solar Cells. Solar RRL. p. 1900245.
125. Kamarudin, M.A., et al., Suppression of Charge Carrier Recombination in Lead-Free Tin Halide Perovskite via Lewis Base Post-treatment. The Journal of Physical Chemistry Letters, 2019. 10(17): p. 5277-5283.

126. Ogomi, Y., et al., $CH_3NH_3Sn_xPb_{(1-x)}I_3$ Perovskite Solar Cells Covering up to 1060 nm. The Journal of Physical Chemistry Letters, 2014. 5(6): p. 1004-1011.
127. Hao, F., et al., Anomalous Band Gap Behavior in Mixed Sn and Pb Perovskites Enables Broadening of Absorption Spectrum in Solar Cells. Journal of the American Chemical Society, 2014. 136(22): p. 8094-8099.
128. Zhao, D., et al., Low-bandgap mixed tin–lead iodide perovskite absorbers with long carrier lifetimes for all-perovskite tandem solar cells. Nature Energy, 2017. 2: p. 17018.
129. Zuo, F., et al., Binary-Metal Perovskites Toward High-Performance Planar-Heterojunction Hybrid Solar Cells. Advanced Materials, 2014. 26(37): p. 6454-6460.
130. Zhu, H.L., et al., Controllable Crystallization of $CH_3NH_3Sn_{0.25}Pb_{0.75}I_3$ Perovskites for Hysteresis-Free Solar Cells with Efficiency Reaching 15.2%. Advanced Functional Materials, 2017. 27(11): p. 1605469.
131. Zong, Y., et al., Lewis-Adduct Mediated Grain-Boundary Functionalization for Efficient Ideal-Bandgap Perovskite Solar Cells with Superior Stability. Advanced Energy Materials, 2018. 8(27): p. 1800997.
132. Zhu, Z., et al., Improved Efficiency and Stability of Pb/Sn Binary Perovskite Solar Cells Fabricated by Galvanic Displacement Reaction. Advanced Energy Materials, 2019. 9(7): p. 1802774.
133. Tong, J., et al., Carrier lifetimes of 1 μs in Sn-Pb perovskites enable efficient all-perovskite tandem solar cells. Science, 2019. 364(6439): p. 475-479.
134. Lin, R., et al., Monolithic all-perovskite tandem solar cells with 24.8% efficiency exploiting comproportionation to suppress Sn(ii) oxidation in precursor ink. Nature Energy, 2019. 4(10): p. 864-873.
135. Yang, Z., et al., Enhancing electron diffusion length in narrow-bandgap perovskites for efficient monolithic perovskite tandem solar cells. Nature Communications, 2019. 10(1): p. 4498.
136. Li, C., et al., Reducing Saturation-Current Density to Realize High-Efficiency Low-Bandgap Mixed Tin–Lead Halide Perovskite Solar Cells. Advanced Energy Materials, 2019. 9(3): p. 1803135.

137. Jiang, T., et al., Realizing High Efficiency over 20% of Low-Bandgap Pb–Sn-Alloyed Perovskite Solar Cells by In Situ Reduction of Sn^{4+}. Solar RRL, 2020. 4(3): p. 1900467.
138. Kapil, G., et al., Strain Relaxation and Light Management in Tin–Lead Perovskite Solar Cells to Achieve High Efficiencies. ACS Energy Letters, 2019. 4(8): p. 1991-1998.
139. Zhao, D., et al., Efficient two-terminal all-perovskite tandem solar cells enabled by high-quality low-bandgap absorber layers. Nature Energy, 2018. 3(12): p. 1093-1100.
140. Green, M.A., A. Ho-Baillie, and H.J. Snaith, The emergence of perovskite solar cells. Nature Photonics, 2014. 8: p. 506.
141. Tai, Q., K.C. Tang, and F. Yan, Recent progress of inorganic perovskite solar cells. Energy & Environmental Science, 2019. 12(8): p. 2375-2405.
142. Zhao, Z., et al., Metal Halide Perovskite Materials for Solar Cells with Long-Term Stability. Advanced Energy Materials, 2019. 9(3): p. 1802671.
143. You, P., et al., Ultrafast laser-annealing of perovskite films for efficient perovskite solar cells. Energy & Environmental Science, 2020.
144. Xiao, J.W., et al., The Emergence of the Mixed Perovskites and Their Applications as Solar Cells. Advanced Energy Materials, 2017. 7(20): p. 1700491.
145. Xie, C., et al., Perovskite-Based Phototransistors and Hybrid Photodetectors. Advanced Functional Materials. p. 1903907.
146. Zheng, G., et al., Manipulation of facet orientation in hybrid perovskite polycrystalline films by cation cascade. Nature Communications, 2018. 9(1): p. 2793.
147. Leblebici, S.Y., et al., Facet-dependent photovoltaic efficiency variations in single grains of hybrid halide perovskite. Nature Energy, 2016. 1(8): p. 16093.
148. Cho, N., et al., Pure crystal orientation and anisotropic charge transport in large-area hybrid perovskite films. Nature Communications, 2016. 7(1): p. 13407.
149. Xu, Z., et al., A Thermodynamically Favored Crystal Orientation in Mixed Formamidinium/Methylammonium Perovskite for Efficient Solar Cells.

Advanced Materials, 2019. 31(24): p. 1900390.

150. Wang, Y., et al., Two-Dimensional van der Waals Epitaxy Kinetics in a Three-Dimensional Perovskite Halide. Crystal Growth & Design, 2015. 15(10): p. 4741-4749.
151. Lin, Z., et al., Scalable solution-phase epitaxial growth of symmetry-mismatched heterostructures on two-dimensional crystal soft template. Science Advances, 2016. 2(10): p. e1600993.
152. Wang, Y., et al., Epitaxial Growth of Large-Scale Orthorhombic $CsPbBr_3$ Perovskite Thin Films with Anisotropic Photoresponse Property. Advanced Functional Materials, 2019. 29(43): p. 1904913.
153. Wang, Y., et al., High-Temperature Ionic Epitaxy of Halide Perovskite Thin Film and the Hidden Carrier Dynamics. Advanced Materials, 2017. 29(35): p. 1702643.
154. Das, S., et al., The Role of Graphene and Other 2D Materials in Solar Photovoltaics. Advanced Materials, 2019. 31(1): p. 1802722.
155. Zhao, X., et al., Efficient Planar Perovskite Solar Cells with Improved Fill Factor via Interface Engineering with Graphene. Nano Letters, 2018. 18(4): p. 2442-2449.
156. Cui, Y., et al., High-Performance Monolayer WS_2 Field-Effect Transistors on High-κ Dielectrics. Advanced Materials, 2015. 27(35): p. 5230-5234.
157. Geim, A.K. and I.V. Grigorieva, Van der Waals heterostructures. Nature, 2013. 499(7459): p. 419-425.
158. Duan, X., et al., Lateral epitaxial growth of two-dimensional layered semiconductor heterojunctions. Nature Nanotechnology, 2014. 9(12): p. 1024-1030.
159. Coleman, J.N., et al., Two-Dimensional Nanosheets Produced by Liquid Exfoliation of Layered Materials. Science, 2011. 331(6017): p. 568-571.
160. Liu, S., et al., Black Phosphorus Quantum Dots Used for Boosting Light Harvesting in Organic Photovoltaics. Angewandte Chemie International Edition, 2017. 56(44): p. 13717-13721.
161. Chen, L., et al., Toward Long-Term Stability: Single-Crystal Alloys of Cesium-Containing Mixed Cation and Mixed Halide Perovskite. Journal of the

American Chemical Society, 2019. 141(4): p. 1665-1671.

162. Xue, Y., et al., Scalable Production of a Few-Layer MoS_2/WS_2 Vertical Heterojunction Array and Its Application for Photodetectors. ACS Nano, 2016. 10(1): p. 573-580.
163. Shi, Y., et al., van der Waals Epitaxy of MoS_2 Layers Using Graphene As Growth Templates. Nano Letters, 2012. 12(6): p. 2784-2791.
164. Zhang, H., Ultrathin Two-Dimensional Nanomaterials. ACS Nano, 2015. 9(10): p. 9451-9469.
165. Tai, Q., et al., Antioxidant Grain Passivation for Air-Stable Tin-Based Perovskite Solar Cells. Angewandte Chemie International Edition, 2019. 58(3): p. 806-810.
166. Hong, L., et al., Guanine-Stabilized Formamidinium Lead Iodide Perovskites. Angewandte Chemie International Edition. n/a(n/a).
167. Chen, G., et al., Air-Stable Highly Crystalline Formamidinium Perovskite 1D Structures for Ultrasensitive Photodetectors. Advanced Functional Materials. p. 1908894.
168. Zhu, C., et al., Strain engineering in perovskite solar cells and its impacts on carrier dynamics. Nature Communications, 2019. 10(1): p. 815.
169. Shi, B., et al., Facile and Controllable Synthesis of Large-Area Monolayer WS_2 Flakes Based on WO_3 Precursor Drop-Casted Substrates by Chemical Vapor Deposition. Nanomaterials, 2019. 9(4): p. 578.
170. Tang, G., et al., Solution-Phase Epitaxial Growth of Perovskite Films on 2D Material Flakes for High-Performance Solar Cells. Advanced Materials, 2019. 31(24): p. 1807689.
171. Sze, S.M., Semiconductor devices: physics and technology. 2008: John wiley & sons.
172. Cao, J., et al., Enhanced performance of tin-based perovskite solar cells induced by an ammonium hypophosphite additive. Journal of Materials Chemistry A, 2019. 7(46): p. 26580-26585.
173. Chen, J., et al., Multifunctional Chemical Linker Imidazoleacetic Acid Hydrochloride for 21% Efficient and Stable Planar Perovskite Solar Cells. Advanced Materials, 2019. 31(39): p. 1902902.

174. Shi, P., et al., Template-Assisted Formation of High-Quality α-Phase $HC(NH_2)_2PbI_3$ Perovskite Solar Cells. Advanced Science, 2019. 6(21): p. 1901591.
175. Liu, M., et al., Aluminum-Doped Cesium Lead Bromide Perovskite Nanocrystals with Stable Blue Photoluminescence Used for Display Backlight. Advanced Science, 2017. 4(11): p. 1700335.
176. Bai, Y., et al., Liquid-Phase Growth and Optoelectronic Properties of Two-dimensional Hybrid Perovskites $CH_3NH_3PbX_3$ (X=Cl, Br, I). Nanoscale, 2019.
177. Li, H., et al., Enhancing Efficiency of Perovskite Solar Cells via Surface Passivation with Graphene Oxide Interlayer. ACS Applied Materials & Interfaces, 2017. 9(44): p. 38967-38976.
178. Fakharuddin, A., et al., Interfaces in Perovskite Solar Cells. Advanced Energy Materials, 2017. 7(22): p. 1700623.
179. Kim, H.-S., et al., Lead Iodide Perovskite Sensitized All-Solid-State Submicron Thin Film Mesoscopic Solar Cell with Efficiency Exceeding 9%. Scientific Reports, 2012. 2: p. 591.
180. Yang, W.S., et al., Iodide management in formamidinium-lead-halide–based perovskite layers for efficient solar cells. Science, 2017. 356(6345): p. 1376-1379.
181. You, P., et al., Efficient Semitransparent Perovskite Solar Cells with Graphene Electrodes. Advanced Materials, 2015. 27(24): p. 3632-3638.
182. Tai, Q., et al., Efficient and stable perovskite solar cells prepared in ambient air irrespective of the humidity. Nature Communications, 2016. 7: p. 11105.
183. Liu, Z., et al., Ultrathin and flexible perovskite solar cells with graphene transparent electrodes. Nano Energy, 2016. 28: p. 151-157.
184. Park, B.W., et al., Bismuth Based Hybrid Perovskites $A_3Bi_2I_9$ (A: Methylammonium or Cesium) for Solar Cell Application. Advanced Materials, 2015. 27(43): p. 6806-6813.
185. Nie, R., et al., Mixed Sulfur and Iodide-Based Lead-Free Perovskite Solar Cells. Journal of the American Chemical Society, 2018. 140(3): p. 872-875.
186. Ke, W., C.C. Stoumpos, and M.G. Kanatzidis, “Unleaded” Perovskites: Status

Quo and Future Prospects of Tin-Based Perovskite Solar Cells. Advanced Materials. p. 1803230.

187. Liao, W., et al., Lead-Free Inverted Planar Formamidinium Tin Triiodide Perovskite Solar Cells Achieving Power Conversion Efficiencies up to 6.22%. Advanced Materials, 2016. 28(42): p. 9333-9340.
188. Lee, S.J., et al., Fabrication of Efficient Formamidinium Tin Iodide Perovskite Solar Cells through SnF_2–Pyrazine Complex. Journal of the American Chemical Society, 2016. 138(12): p. 3974-3977.
189. Zhao, Z., et al., Mixed-Organic-Cation Tin Iodide for Lead-Free Perovskite Solar Cells with an Efficiency of 8.12%. Advanced Science, 2017: p. 1700204.
190. Ke, W., et al., Enhanced photovoltaic performance and stability with a new type of hollow 3D perovskite {en}$FASnI_3$. Science Advances, 2017. 3(8): p. e1701293.
191. Wang, F., et al., 2D-Quasi-2D-3D Hierarchy Structure for Tin Perovskite Solar Cells with Enhanced Efficiency and Stability. Joule, 2018.
192. Wijeyasinghe, N., et al., Copper(I) Thiocyanate (CuSCN) Hole-Transport Layers Processed from Aqueous Precursor Solutions and Their Application in Thin-Film Transistors and Highly Efficient Organic and Organometal Halide Perovskite Solar Cells. Advanced Functional Materials, 2017. 27(35): p. 1701818.
193. Xu, W., et al., Precisely Controlling the Grain Sizes with an Ammonium Hypophosphite Additive for High-Performance Perovskite Solar Cells. Advanced Functional Materials, 2018. 28(33): p. 1802320.
194. Zhu, Z., et al., Realizing Efficient Lead-Free Formamidinium Tin Triiodide Perovskite Solar Cells via a Sequential Deposition Route. Advanced Materials, 2018. 30(6): p. 1703800.
195. Yang, X., et al., Efficient green light-emitting diodes based on quasi-two-dimensional composition and phase engineered perovskite with surface passivation. Nature Communications, 2018. 9(1): p. 570.
196. Si, H., et al., Deciphering the NH_4PbI_3 Intermediate Phase for Simultaneous Improvement on Nucleation and Crystal Growth of Perovskite. Advanced Functional Materials, 2017. 27(30): p. 1701804.

197. Zuo, C., et al., One-step roll-to-roll air processed high efficiency perovskite solar cells. Nano Energy, 2018. 46: p. 185-192.

198. Tang, G., et al., Performance Enhancement of Perovskite Solar Cells Induced by Lead Acetate as an Additive. Solar RRL, 2018. 2(6): p. 1800066.

199. Ke, W., et al., Efficient Lead-Free Solar Cells Based on Hollow {en}$MASnI_3$ Perovskites. Journal of the American Chemical Society, 2017. 139(41): p. 14800-14806.

200. Jokar, E., et al., Robust Tin-Based Perovskite Solar Cells with Hybrid Organic Cations to Attain Efficiency Approaching 10%. Advanced Materials. p. 1804835.

201. Shao, S., et al., The Effect of the Microstructure on Trap-Assisted Recombination and Light Soaking Phenomenon in Hybrid Perovskite Solar Cells. Advanced Functional Materials, 2016. 26(44): p. 8094-8102.

202. Jung, J.W., C.C. Chueh, and A.K.Y. Jen, High-Performance Semitransparent Perovskite Solar Cells with 10% Power Conversion Efficiency and 25% Average Visible Transmittance Based on Transparent CuSCN as the Hole-Transporting Material. Advanced Energy Materials, 2015. 5(17): p. 1500486.

203. Liu, X., et al., Improving the Performance of Inverted Formamidinium Tin Iodide Perovskite Solar Cells by Reducing the Energy-Level Mismatch. ACS Energy Letters, 2018. 3(5): p. 1116-1121.

204. Wang, Q., et al., Large fill-factor bilayer iodine perovskite solar cells fabricated by a low-temperature solution-process. Energy & Environmental Science, 2014. 7(7): p. 2359-2365.

205. He, C., et al., Origin of the enhanced open-circuit voltage in polymer solar cells via interfacial modification using conjugated polyelectrolytes. Journal of Materials Chemistry, 2010. 20(13): p. 2617-2622.

206. Ke, W., et al., Efficient Lead-Free Solar Cells Based on Hollow {en}$MASnI_3$ Perovskites. Journal of the American Chemical Society, 2017. 139(41): p. 14800-14806.

207. Yang, D., et al., Surface optimization to eliminate hysteresis for record efficiency planar perovskite solar cells. Energy & Environmental Science,

2016. 9(10): p. 3071-3078.

208. Ran, C., et al., Bilateral Interface Engineering toward Efficient 2D–3D Bulk Heterojunction Tin Halide Lead-Free Perovskite Solar Cells. ACS Energy Letters, 2018. 3(3): p. 713-721.
209. Tai, Q., X. Zhao, and F. Yan, Hybrid solar cells based on poly (3-hexylthiophene) and electrospun TiO_2 nanofibers with effective interface modification. Journal of Materials Chemistry, 2010. 20(35): p. 7366-7371.
210. Liu, G., et al., Dependence of power conversion properties of perovskite solar cells on operating temperature. Applied Physics Letters, 2018. 113(11): p. 113501.
211. Ke, W., et al., Diammonium Cations in the $FASnI_3$ Perovskite Structure Lead to Lower Dark Currents and More Efficient Solar Cells. ACS Energy Letters, 2018. 3(7): p. 1470-1476.
212. Chandiran, A.K., et al., Sub-Nanometer Conformal TiO_2 Blocking Layer for High Efficiency Solid-State Perovskite Absorber Solar Cells. Advanced Materials, 2014. 26(25): p. 4309-4312.
213. Juarez Perez, E.J., et al., Role of the Selective Contacts in the Performance of Lead Halide Perovskite Solar Cells. The Journal of Physical Chemistry Letters, 2014. 5(4): p. 680-685.
214. Saliba, M., et al., Incorporation of rubidium cations into perovskite solar cells improves photovoltaic performance. Science, 2016. 354(6309): p. 206.
215. Sha, W.E.I., et al., The efficiency limit of $CH_3NH_3PbI_3$ perovskite solar cells. Applied Physics Letters, 2015. 106(22): p. 221104.
216. Eperon, G.E., M.T. Hörantner, and H.J. Snaith, Metal halide perovskite tandem and multiple-junction photovoltaics. Nature Reviews Chemistry, 2017. 1(12): p. 0095.
217. Leijtens, T., et al., Opportunities and challenges for tandem solar cells using metal halide perovskite semiconductors. Nature Energy, 2018. 3(10): p. 828-838.
218. Liao, W., et al., Fabrication of Efficient Low-Bandgap Perovskite Solar Cells by Combining Formamidinium Tin Iodide with Methylammonium Lead Iodide. Journal of the American Chemical Society, 2016. 138(38): p.

12360-12363.

219. Eperon, G.E., et al., Perovskite-perovskite tandem photovoltaics with optimized band gaps. Science, 2016. 354(6314): p. 861.
220. Tong, J., et al., Carrier lifetimes of 1 μs in Sn-Pb perovskites enable efficient all-perovskite tandem solar cells. Science, 2019. 364(6439): p. 475.
221. Ke, W., C.C. Stoumpos, and M.G. Kanatzidis, "Unleaded" Perovskites: Status Quo and Future Prospects of Tin-Based Perovskite Solar Cells. Advanced Materials, 2019. 31(47): p. 1803230.
222. Zhu, Z., et al., Realizing Efficient Lead-Free Formamidinium Tin Triiodide Perovskite Solar Cells via a Sequential Deposition Route. Advanced Materials, 2018. 30(6): p. 1703800.
223. Shao, S., et al., Highly Reproducible Sn-Based Hybrid Perovskite Solar Cells with 9% Efficiency. Advanced Energy Materials, 2018. 8(4): p. 1702019.
224. Liao, Y., et al., Highly Oriented Low-Dimensional Tin Halide Perovskites with Enhanced Stability and Photovoltaic Performance. Journal of the American Chemical Society, 2017. 139(19): p. 6693-6699.
225. Ramirez, D., et al., Layered Mixed Tin–Lead Hybrid Perovskite Solar Cells with High Stability. ACS Energy Letters, 2018. 3(9): p. 2246-2251.
226. Zheng, X., et al., Defect passivation in hybrid perovskite solar cells using quaternary ammonium halide anions and cations. Nature Energy, 2017. 2(7): p. 17102.
227. Wu, T., et al., Efficient Defect Passivation for Perovskite Solar Cells by Controlling the Electron Density Distribution of Donor-π-Acceptor Molecules. Advanced Energy Materials, 2019. 9(17): p. 1803766.
228. Bi, D., et al., Polymer-templated nucleation and crystal growth of perovskite films for solar cells with efficiency greater than 21%. Nature Energy, 2016. 1(10): p. 16142.
229. He, X., et al., Highly efficient tin perovskite solar cells achieved in a wide oxygen concentration range. Journal of Materials Chemistry A, 2020. 8(5): p. 2760-2768.
230. Han, Q., et al., Low-temperature processed inorganic hole transport layer for efficient and stable mixed Pb-Sn low-bandgap perovskite solar cells. Science

Bulletin, 2019. 64(19): p. 1399-1401.

231. Jokar, E., et al., Robust Tin-Based Perovskite Solar Cells with Hybrid Organic Cations to Attain Efficiency Approaching 10%. Advanced Materials, 2019. 31(2): p. 1804835.

232. Peng, J., et al., A Universal Double-Side Passivation for High Open-Circuit Voltage in Perovskite Solar Cells: Role of Carbonyl Groups in Poly(methyl methacrylate). Advanced Energy Materials, 2018. 8(30): p. 1801208.

233. Meng, X., et al., Highly Stable and Efficient $FASnI_3$-Based Perovskite Solar Cells by Introducing Hydrogen Bonding. Advanced Materials, 2019. 31(42): p. 1903721.

234. Sze, S.M. and K.K. Ng, Physics of semiconductor devices. 2006: John wiley & sons.

235. Kumar, M.H., et al., Lead-Free Halide Perovskite Solar Cells with High Photocurrents Realized Through Vacancy Modulation. Advanced Materials, 2014. 26(41): p. 7122-7127.